Rate of Hydrate formation
=4.2×10^{-6} (moles hydrate/second)

Step 5

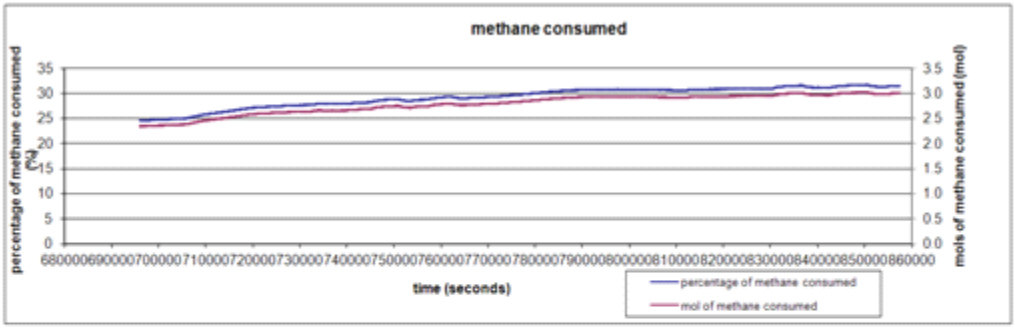

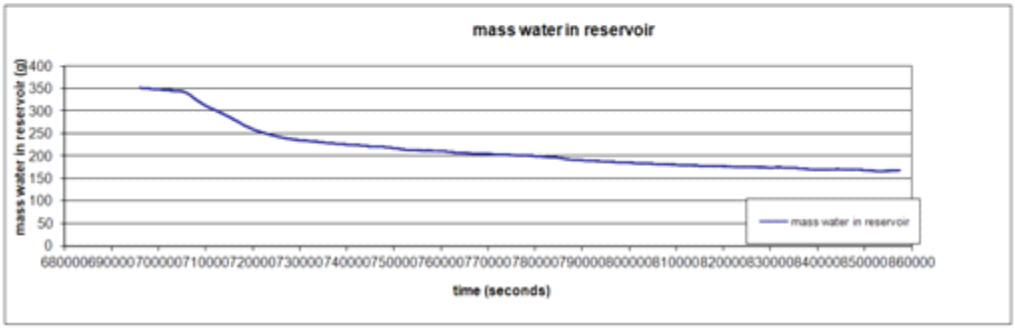

Rate of Hydrate formation
=2.4×10^{-6} (moles hydrate/second)

Step 6

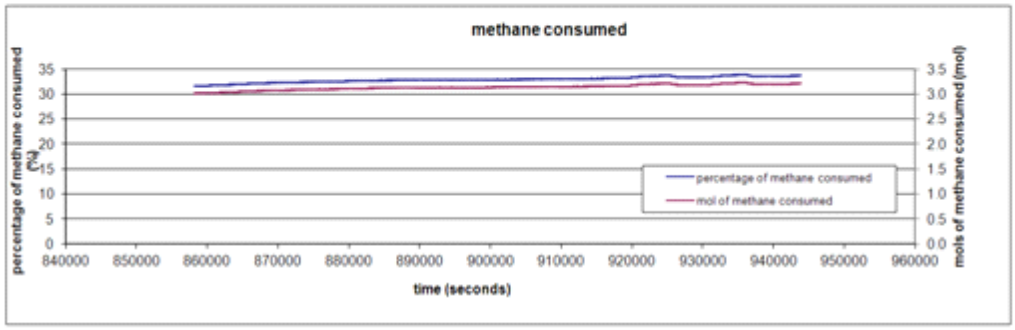

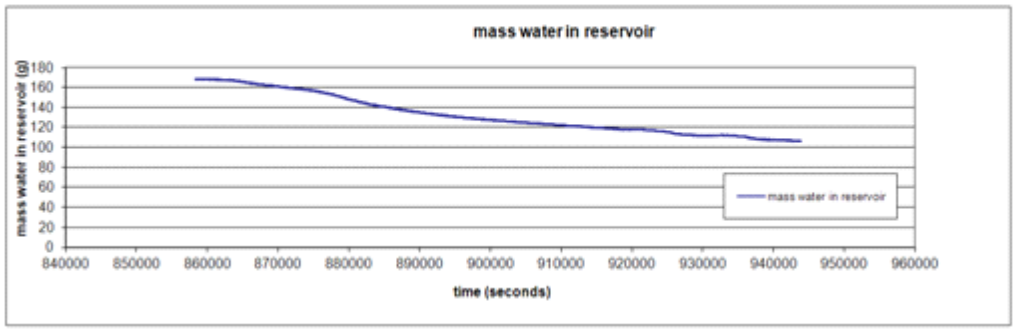

Rate of Hydrate formation
=2.4×10^{-6} (moles hydrate/second)

Step 7

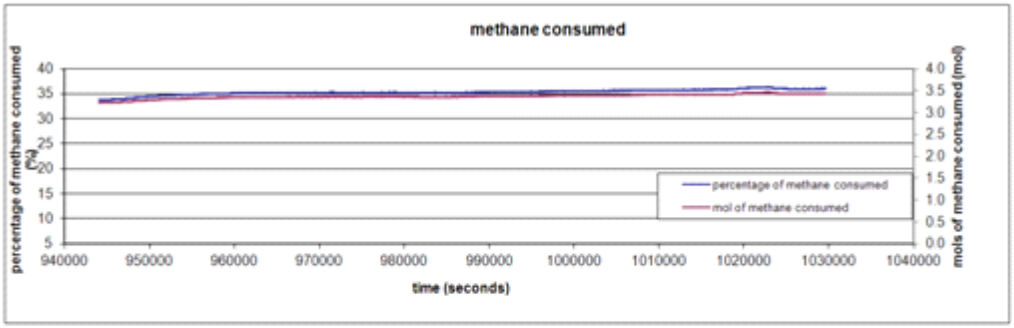

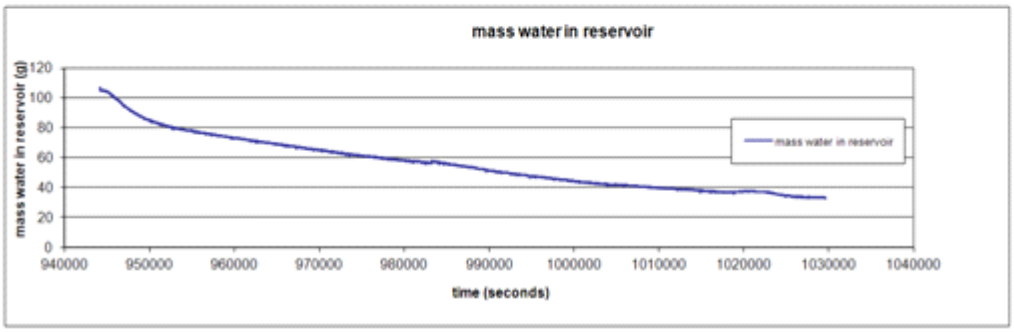

Rate of Hydrate formation
=1.3×10^{-6} (moles hydrate/second)

Step 8

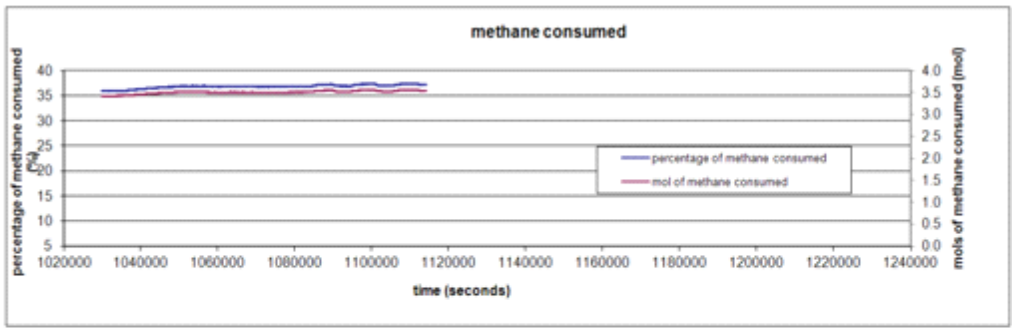

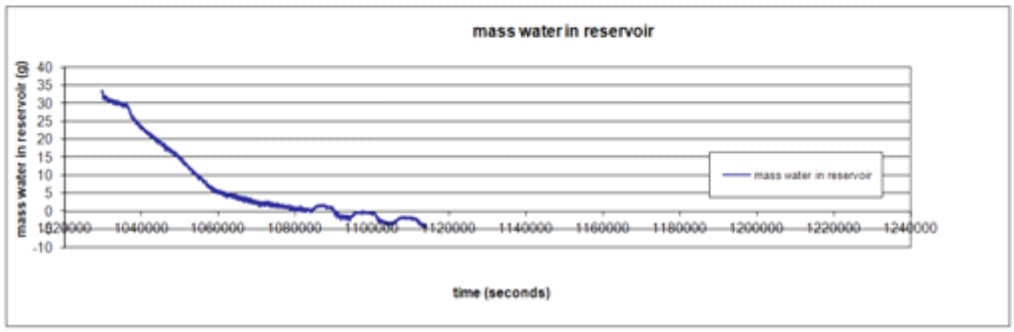

Discussion of Findings from Experimental Descent of Gas Hydrate Stability Zone

The experimental boundary conditions do not replicate the situation in gas reservoirs converted to hydrate in the Arctic. The key differences are that in the experiment water can move

to the hydrate stability zone only from below, while in nature water can move from below and from above. In experiment gas can move to the hydrate stability zone from below and from above, while in nature it can move only from below. Finally, the fluid phase pressures decrease with time in the experiment (though the conditions remain within the hydrate stability field throughout), while the water phase pressure does not change with time in nature. These differences are minor and do not alter the essential similarities to the natural situation. In the experiment and in nature, the base of the gas hydrate stability zone descends gradually through an existing gas accumulation, and fluid phases are free to move in response to any gradients that arise as hydrate forms. The latter point is important: no fluid flow (neither pressure-driven nor capillarity-driven) is imposed in the experiment. Instead the system evolves a combination of buoyancy-, pressure- and capillarity-driven fluxes of the gas and water phases, and these fluxes balance the various resistances to transport.

The model predicts that the contribution of capillarity-driven flux is significant in these experiments. In fact R_v~0.69 when capillary-dominated flow is taken into account while R_v~1 when only the viscous dominated portion of the flow was considered. This is consistent with our findings in previous sections of this report, namely, pressure-driven flow cannot supply water from below the BGHSZ fast enough to sustain hydrate formation. Moreover the model predicts that the amount of gas flows to the GHSZ from above quickly diminishes as both the effective permeability, due to hydrate formation within the GHSZ, and gaseous phase relative permeability, due to decrease in gas saturation within the GHSZ, decrease. Therefore, the main contribution for gas flow would be flow from the middle gas inlet. While the gas flux from above and from below could not be independently measured in this experiment, the consistency of the model with other observations suggests that all the fluids needed during conversion to hydrate can be supplied from below. But this is possible only if capillarity-driven flux is accounted for.

The consistency of the capillarity-driven flux model with the experimental observations suggests that the finding in the previous section, viz. that the observed hydrate saturation profile in Mt. Elbert arises naturally from the capillarity-driven fluxes, is not a coincidence. That is, these findings suggest that the gas reservoir conversion process is slow, that it introduces modest, even negligible pressure gradients but impose significant gradients in saturation which, along with gas buoyancy, feed the appropriate volumes of fluids to the GHSZ.

A complete validation of the model would compare the predicted hydrate saturation profile to the observed profile in Fig. 60. Unfortunately this is not possible because we do not know the initial gas saturation profile. The required horizontal positioning of the column during scanning would have disrupted the gas-water saturation distribution achieved in the vertical orientation of the experiment. Thus the experiment proceeded with knowledge only of the mass of gas in the column and the observation that gas was produced from the bottom of the column during injection. This is sufficient only to bound the possible initial saturation profile, e.g. if it were uniform, the initial gas phase saturation would have been 0.20. As discussed above, it is possible to make a plausible estimate of the original gas saturation profile, and this does lead to a prediction consistent with the final profile. It would be valuable to repeat the experiment and eliminate this uncertainty.

The coarse/fine layering in the sand pack was intended to represent the variation that allows for disconnection of the gas column as the gas-water contact rises during conversion to hydrate. This is a key mechanism leading to large saturations in the upper portions of layers, separated by regions of small hydrate saturation. The experiment did not test this mechanism directly, because the pressure in the gas phase probably was controlled by gas column height. Though the

gas/water contact presumably rose during the experiment as water entered the bottom of the sandpack, the gas phase in the sandpack was always connected to the gas reservoir pressure by the inlets at the top and at the midpoint of the sand pack. Thus disconnection of the gas column across fine sand layers probably did not occur, and the gas phase was able to flow anywhere within the top half of the sandpack throughout the experiment.

Conclusions from Experiment on Descending Base of Gas Hydrate Stability Zone

After establishing a gas saturation within a long (1 m) sand column, short (10 cm) sections of the column were sequentially (from top to bottom) cooled to conditions at which hydrate was stable. While the boundary conditions (a source of gas and water phases at same pressure, with gas line connected to the top and midpoint of the sand column and water line connected to the bottom) were not the same as those during the descent of the base of gas hydrate stability zone through gas reservoirs in the Arctic, the driving force for fluid phase movement was identical: the consumption of gas and water and the reduction in phase volume accompanying hydrate formation. A mathematical model of fluid phase transport that accounts for fluxes due to buoyancy pressure gradient and capillary pressure gradient correctly predicted the movement of gas phase and water phase into the sand column from the reservoir, given the observed rate of hydrate formation and the observed pressure history. The agreement with observation is significant, since it requires achieving the correct balance between the different driving forces.

Capillarity-driven fluxes are essential for explaining the observed hydrate distribution. The experiment thus supports the hypothesis that saturation gradients are a key mechanism in the process of converting gas reservoirs to hydrate in the Arctic.

References for Capillarity Dominated Behavior in Hydrate-Bearing Sediments

Anderson, B., Hancock, S., Wilson, S., Enger, C., Collett, T., Boswell, R., and Hunter, R., 2011, Formation pressure testing at the Mount Elbert Gas Hydrate Stratigraphic Test Well, Alaska North Slope: Operational summary, history matching, and interpretations: Marine and Petroleum Geology, v. 28, no. 2, p. 478-492.

Behseresht, J., Bryant, S.L., Sepehrnoori, K., 2009. Infinite-Acting Physically Representative Networks for Capillarity-Controlled Displacements. Soc. Petrol. Eng. J. 14, 568-578.

Bhatnagar, G., Chapman, W.G., Dickens, G.R., Dugan, B., Hirasaki, G.J., 2007. Generalization of gas hydrate distribution and saturation in marine sediments by scaling of thermodynamic and transport processes. Am. J. Sci. 307, 861-900.

Blunt, M., 2001, Flow in porous media -- pore-network models and multiphase flow: Current Opinion in Colloid & Interface Science, v. 6, no. 3, p. 197-207.

Boswell, R., Rose, K., Collett, T.S., Lee, M., Winters, W.J., Lewis, K.A., Agena, W.F., 2011. Geologic controls on gas hydrate occurrence in the Mount Elbert prospect, Alaska North Slope. Mar. Pet. Geol. 28, 589-607.

Bryant, S.L., King, P.R., Mellor, D.W., 1993. Network model evaluation of permeability and spatial correlation in a real random sphere packing. Transp. Porous Media. 11, 53-70.

Buffett, B., 2000. Formation of gas hydrate from dissolved gas in natural porous media. Mar. Geol. 164, 69-77.

Clennell, B.M., Hovland, M., Booth, J.S., Henry, P., Winters, W.J., 1999. Formation of natural gas hydrates in marine sediments 1. Conceptual model of gas hydrate growth conditioned by host sediment properties. J. Geophys. Res. 104, 22985-23003.

Collett, T., and Lee, M., 2005, Electrical-resistivity well-log analysis of gas hydrate saturations in the JAPEX/JNOC/GSC *et al*. Mallik 5L-38 gas hydrate production research well: Scientific results frmo the Mallik 2002 Gas hydrate Production Research Well Program, Mackenzie Delta, Northwest Territories, Canada.

Collett, T.S., 1993. Natural Gas Hydrates of the Prudhoe Bay and Kuparuk River Area, North Slope, Alaska. Am. Assoc. Pet. Geol. Bull. 77, 793-812.

Collett, T.S., Johnson, A., Knapp, C., Boswell, R., 2009. Natural Gas Hydrates – A Review, in: Natural Gas Hydrates – Energy Resource Potential and Associated Geologic Hazards, Mem. Am. Assoc. Pet. Geol. 89, 146–219.

Collett, T.S., Lee, M.W., Agena, W.F., Miller, J.J., Lewis, K.A., Zyrianova, M.V., Boswell, R., Inks, T.L., 2011. Permafrost-associated natural gas hydrate occurrences on the Alaska North Slope. Mar. Pet. Geol. 28, 279-294.

Dai, S., Lee, C., Santamarina, J.C., 2011. Formation history and physical properties of sediments from the Mount Elbert Gas Hydrate Stratigraphic Test Well, Alaska North Slope. Mar. Pet. Geol. 28, 427-438.

Dallimore, S.R., Collett, T.S., 2005. Scientific results from the Mallik 2002 gas hydrate production research well program, Mackenzie delta, Northwest Territories, Bull. Geol. Surv. Can., 585.

Dawe, R.A., Wheat, M.R., Bidner, M.S., 1992. Experimental investigation of capillary pressure effects on immiscible displacement in lensed and layered porous media. Transp. Porous Media. 7, 83-101.

Dong Lee, J., Susilo, R., and Englezos, P., 2005, Methane-ethane and methane-propane hydrate formation and decomposition on water droplets: Chemical Engineering Science, v. 60, no. 15, p. 4203-4212.

Fujii, T., Saeki, T., Kobayashi, T., Inamori, T., Hayashi, M., Takano, O., Takayama, T., Kawasaki, T., Nagakubo, S., Nakamizu, M., Yokoi, K., 2008. Resource Assessment of Methane Hydrate in the Eastern Nankai Trough, Japan. Presented in Offshore Technology Conference, 5-8 May 2008, Houston, Texas, USA.

Ginsburg, G.D., 1998. Gas hydrate accumulation in deep-water marine sediments. J. Geol. Soc. (London, U.K.) Special Publications. 137, 51-62.

Gladkikh, M., and Bryant, S., 2005, Prediction of imbibition in unconsolidated granular materials: Journal of Colloid and Interface Science, v. 288, no. 2, p. 526-539.

Hadley, C., Peters, D., Vaughan, A., Bean, D., 2008. Gumusut-Kakap Project: Geohazard Characterisation and Impact on Field Development Plans, Presented in International Petroleum Technology Conference, 3-5 December, Kuala Lumpur, Malaysia.

Handa, Y., 1990, Effect of hydrostatic pressure and salinity on the stability of gas hydrates: The Journal of Physical Chemistry, v. 94, no. 6, p. 2652-2657.

Handa, Y.P., 1986. Calorimetric determinations of the compositions, enthalpies of dissociation, and heat capacities in the range 85 to 270 K for clathrate hydrates of xenon and krypton. J. Chem. Thermodyn. 18, 891-902.

Hensen, C., Wallmann, K., 2005. Methane formation at Costa Rica continental margin—constraints for gas hydrate inventories and cross-décollement fluid flow. Earth Planet. Sci. Lett. 236, 41-60.

Hilpert, M., McBride, J.F., Miller, C.T., 2000. Investigation of the residual–funicular nonwetting-phase-saturation relation. Adv. Water Resour. 24, 157-177.

Hirai, S., Okazaki, K., Araki, N., Yazawa, H., Ito, H., and Hijikata, K., 1996, Transport phenomena of liquid CO2 in pressurized water flow with clathrate-hydrate at the interface: Energy Conversion and Management, v. 37, no. 6-8, p. 1073-1078.

Holbrook, S., Hoskins, H., Wood, W., Stephen, R., and Lizarralde, D., 1996, Methane Hydrate and Free Gas on the Blake Ridge from Vertical Seismic Profiling: Science, v. 273, no. 5283, p. 1840 -1843.

Holland, M., Schultheiss, P., Roberts, J., Druce, M., 2008. Observed gas Hydrate morphologies in marine sediments. Presented in the 6th International Conference on Gas Hydrates, Vancouver, British Columbia, Canada.

Hunter, R., Collett, T., Boswell, R., Anderson, B., Digert, S., Pospisil, G., Baker, R., and Weeks, M., 2011, Mount Elbert Gas Hydrate Stratigraphic Test Well, Alaska North Slope: Overview of scientific and technical program: Marine and Petroleum Geology, v. 28, no. 2, p. 295-310.

Hyndman, R., and Spence, G., 1992, A Seismic Study of Methane Hydrate Marine Bottom Simulating Reflectors: Journal of Geophysical Research, v. 97, no. B5, p. PP. 6683-6698.

Hyndman, R.D., Davis, E.E., 1992. A Mechanism for the Formation of Methane Hydrate and Seafloor Bottom-Simulating Reflectors by Vertical Fluid Expulsion. J. Geophys. Res. 97, 7025-7041.

Inks, T., Lee, M., Agena, W.F., Taylor, D., Collett, T.S., Hunter, R., Zyrianova, M., 2009. Seismic prospecting for gas hydrate and associated free gas prospects in the Milne Point area of northern Alaska, in: Collett, T.S., Johnson, A., Knapp, C., Boswell R., eds., Natural Gas Hydrates – Energy Resource Potential and Associated Geologic Hazards. Mem. Am. Assoc. Pet. Geol., 89.

Iversen, N., Jorgensen, B., 1993. Diffusion coefficients of sulfate and methane in marine sediments: Influence of porosity. Geochim. Cosmochim. Acta. 57, 571-578.

Jho, C., Nealon, D., Shogbola, S., King, A.D., 1978. Effect of pressure on the surface tension of water: Adsorption of hydrocarbon gases and carbon dioxide on water at temperatures between 0 and 50℃ . J. Colloid Interface Sci. 65, 141-154.

Katsube, T., Dallimore, S., Jonasson, I., Connell-Madore, S., Medioli, B., Uchida, T., Wright, J., and Scromeda, N., 2005, Petrophysical characteristics of gas-hydrate-bearing and gas-hydrate-gree formations in the JAPEX/JNOC/GSC *et al*. Mallik 5L-38 gas hydrate production research well: Geological Survey of Canada, Scientific results frmo the Mallik 2002 Gas hydrate Production Research Well Program, Mackenzie Delta, Northwest Territories, Canada.

Katsuki, D., Ohmura, R., Ebinuma, T., and Narita, H., 2006, Formation, growth and ageing of clathrate hydrate crystals in a porous medium: Philosophical Magazine, v. 86, no. 12, p. 1753-1761.

Katsuki, D., Ohmura, R., Ebinuma, T., and Narita, H., 2007, Methane hydrate crystal growth in a porous medium filled with methane-saturated liquid water: Philosophical Magazine, v. 87, no. 7, p. 1057-1069.

Kleinberg, R., Flaum, C., and Collett, T., 2005, Magnetic resonance log of JAPEX/JNOC/GSC *et al*. Mallik 5L-38 gas hydrate production research well: gas hydrate saturation, growth habit, and relative permeability: Geological Survey of Canada, Scientific results from the Mallik 2002 Gas hydrate Production Research Well Program, Mackenzie Delta, Northwest Territories, Canada.

Koh, C., Westacott, R. ., Zhang, W., Hirachand, K., Creek, J., Soper, A., 2002. Mechanisms of gas hydrate formation and inhibition. Fluid Phase Equilib. 194-197, 143-151.

Kvenvolden, K., 1988. Methane hydrate — A major reservoir of carbon in the shallow geosphere? Chem. Geol. 71, 41-51.

Lee, M., and Collett, T., 2005, Assessment of gas hydrate concentrations estimated from sonic logs in the JAPEX/JNOC/GSC *et al*. Mallik 5L-38 gas hydrate research production well: Geological Survey of Canada, Scientific results frmo the Mallik 2002 Gas hydrate Production Research Well Program, Mackenzie Delta, Northwest Territories, Canada.

Lee, M.W., Collett, T.S., 2011. In-situ gas hydrate saturation estimated from various well logs at the Mount Elbert Gas Hydrate Stratigraphic Test Well, Alaska North Slope. Mar. Pet. Geol. 28, 439-449.

Liu, X., and Flemings, P., 2007, Dynamic multiphase flow model of hydrate formation in marine sediments: Journal of Geophysical Research, v. 112, no. B3.

Liu, X., Flemings, P.B., 2006. Passing gas through the hydrate stability zone at southern Hydrate Ridge, offshore Oregon. Earth Planet. Sci. Lett. 241, 211-226.

Lorenson, T., Collett, T., and Hunter, R., 2011, Gas geochemistry of the Mount Elbert Gas Hydrate Stratigraphic Test Well, Alaska North Slope: Implications for gas hydrate exploration in the Arctic: Marine and Petroleum Geology, v. 28, no. 2, p. 343-360.

Majorowicz, J., Osadetz, K., and Safanda, J., 2008, Onset and stability of gas hydrates under permafrost in an environment of surface climatic change - past and future, *in* Vancouver, Canada.

Majorowicz, J.A., Osadetz, K., Safanda, J., 2008. Modeling temperature profiles considering the latent heat of physical-chemical reactions in permafrost and gas hydrates: The Mackenzie

Delta terrestrial case, Presented in the Ninth International Conference on Permafrost, Fairbanks, Alaska USA, pp. 1113-1118.

Mason, G., Mellor, D.W., 1995. Simulation of Drainage and Imbibition in a Random Packing of Equal Spheres. J. Colloid Interface Sci. 176, 214-225.

Matsumoto, R., Tomaru, H., Chen, Y., Lu, H., and Clark, I., 2005, Geochemistry of the interstitial waters of the JAPEX/JNOC/GSC *et al*. Mallik 5L-38 gas hydrate production research well: Geological Survey of Canada, Scientific results frmo the Mallik 2002 Gas hydrate Production Research Well Program, Mackenzie Delta, Northwest Territories, Canada.

Mori, Y., and Mochizuki, T., 1997, Mass transport across clathrate hydrate films -- a capillary permeation model: Chemical Engineering Science, v. 52, no. 20, p. 3613-3616.

Odong, J., 2008. Evaluation of Empirical Formulae for Determination of Hydraulic Conductivity based on Grain-Size Analysis. J. Am. Sci. 4, 1-6.

Ohmura, R., Matsuda, S., Uchida, T., Ebinuma, T., and Narita, H., 2005, Clathrate hydrate crystal growth in liquid water saturated with a guest substance: Observations in a methane + water System: Crystal Growth & Design, v. 5, no. 3, p. 953-957.

Peng, Y., 2011, Study of methane hydrate formation and distribution in arctic regions: from pore scale to field scale [PhD dissertation]: The University of Texas at Austin.

Peng, Y., Prodanovic, M., Bryant, S.L., 2009. Improving Fidelity of Network Models for Drainage and Imbibition. Presented in SPE Annual Technical Conference and Exhibition, 4-7 October, New Orleans, Louisiana.

Prodanović, M., and Bryant, S., 2006, A level set method for determining critical curvatures for drainage and imbibition: Journal of Colloid and Interface Science, v. 304, no. 2, p. 442-458.

Prodanović, M., Bryant, S., and Karpyn, Z., 2008, Investigating matrix-fracture transfer via a level set method for drainage and imbibition, *in* Proceedings of SPE Annual Technical Conference and Exhibition.

Ripmeester, J., Lu, H., Moudrakovski, I., Dutrisac, R., Wilson, L., Wright, F., and Dallimore, S., 2005, Structure and composition of gas hydrate in sediment recoverd from JAPEX/JNOC/GSC *et al*. Mallik 5L-38 gas hydrate production research well, determined by X-ray diffraction and Raman and solid-state nuclear magnetic resonance spectroscopy: Geological Survey of Canada, Scientific results frmo the Mallik 2002 Gas hydrate Production Research Well Program, Mackenzie Delta, Northwest Territories, Canada.

Ripmeester, J.A., Ratcliffe, C.I., 1988. Low-temperature cross-polarization/magic angle spinning 13C NMR of solid methane hydrates: Structure, cage occupancy, and hydration number. J. Phys. Chem. 92, 337-339.

Rose, K., Boswell, R., Collett, T.S., 2011. Mount Elbert Gas Hydrate Stratigraphic Test Well, Alaska North Slope: Coring operations, core sedimentology, and lithostratigraphy. Mar. Pet. Geol. 28, 311-331.Setzmann, U.; Wagner, W., A New Equation of State and Tables of Thermodynamic Properties for Methane Covering the Range from the Melting Line to 625 K at Pressures up to 1000 MPa, **J. Phys. Chem. Ref. Data**, 1991, 20(6), 1061-1151.

Ruppel, C., Boswell, R., and Jones, E., 2008, Scientific results from Gulf of Mexico Gas Hydrates Joint Industry Project Leg 1 drilling: Introduction and overview: Marine and Petroleum Geology, v. 25, no. 9, p. 819-829.

Shindo, Y., Fujioka, Y., Takeuchi, K., and Komiyama, H., 1995, Kinetics on the Dissolution of C02 into Water from the Surface of CO2 Hydrate at High Pressure: International Journal of Chemical Kinetics, v. 27, p. 569-575.

Sloan, E., 2003, Fundamental principles and applications of natural gas hydrates: Nature, v. 426, no. 6964, p. 353-363.
Sloan, E., and Koh, C., 2008, Clathrate hydrates of natural gases: CRC Press.
Sloan, E.D., 1998. Clathrate hydrates of natural gases. 2nd ed. Marcel Dekker, New York.
Sun, R., and Duan, Z., 2007, An accurate model to predict the thermodynamic stability of methane hydrate and methane solubility in marine environments: Chemical Geology, v. 244, no. 1-2, p. 248-262.
Teng, H., Kinoshita, C., and Masutani, S., 1995, Hydrate formation on the surface of a CO2 droplet in high-pressure, low-temperature water: Chemical Engineering Science, v. 50, no. 4, p. 559-564.
Tohidi, B., Anderson, R., Clennell, M., Burgass, R., and Biderkab, A., 2001, Visual observation of gas-hydrate formation and dissociation in synthetic porous media by means of glass micromodels: Geology, v. 29, no. 9, p. 867-870.
Torres, M.E., Collett, T.S., Rose, K.K., Sample, J.C., Agena, W.F., Rosenbaum, E.J., 2011. Pore fluid geochemistry from the Mount Elbert Gas Hydrate Stratigraphic Test Well, Alaska North Slope. Mar. Pet. Geol. 28, 332-342.
Torres, M.E., Wallmann, K., Tréhu, A.M., Bohrmann, G., Borowski, W.S., Tomaru, H., 2004. Gas hydrate growth, methane transport, and chloride enrichment at the southern summit of Hydrate Ridge, Cascadia margin off Oregon. Earth Planet. Sci. Lett. 226, 225-241.
Tréhu, A., Flemings, P., Bangs, N., Chevallier, J., Gràcia, E., Johnson, J., Liu, C., Liu, X., Riedel, M., and Torres, M., 2004, Feeding methane vents and gas hydrate deposits at south Hydrate Ridge: Geophysical Research Letters, v. 31, p. 4 PP.
Uchida, T., Tsuji, T., Takahashi, T., Okui, T., and Minagawa, H., 2005, Petrophysical properties and sedimentology of gas-hydrate-bearing sediments in the JAPEX/JNOC/GSC *et al*. Mallik 5L-38 gas hydrate production research well: Geological Survey of Canada, Scientific results frmo the Mallik 2002 Gas hydrate Production Research Well Program, Mackenzie Delta, Northwest Territories, Canada.
Valvatne, P., and Blunt, M., 2004, Predictive pore-scale modeling of two-phase flow in mixed wet media: Water Resources Research, v. 40, no. W07406.
Valvatne, P., Piri, M., Lopez, X., and Blunt, M., 2005, Predictive pore-scale modeling of single and multiphase flow: Transport in Porous Media, v. 58, no. 1, p. 23-41.
van Dijke, M., and Sorbie, K., 2003, Pore-scale modelling of three-phase flow in mixed-wet porous media: multiple displacement chains: Journal of Petroleum Science and Engineering, v. 39, no. 3-4, p. 201-216.
Waite, W.F., Santamarina, J.C., Cortes, D.D., Dugan, B., Espinoza, D.N., Germaine, J., Jang, J., Jung, J.W., Kneafsey, T.J., Shin, H., Soga, K., Winters, W.J., Yun, T.S., 2009. Physical properties of hydrate-bearing sediments. Rev. Geophys. 47, RG4003.
Winters, W., Dallimore, S., Collett, T., Medioli, B., Matsumoto, R., Katsube, T., and Brennan-Alpert, P., 2005, Relatinoships of sediment physcial properties from the JAPEX/JNOC/GSC *et al*. Mallik 5L-38 gas hydrate production research well: Geological Survey of Canada, Scientific results frmo the Mallik 2002 Gas hydrate Production Research Well Program, Mackenzie Delta, Northwest Territories, Canada.
Winters, W., Walker, M., Hunter, R., Collett, T., Boswell, R., Rose, K., Waite, W., Torres, M., Patil, S., and Dandekar, A., 2011, Physical properties of sediment from the Mount Elbert Gas Hydrate Stratigraphic Test Well, Alaska North Slope: Marine and Petroleum Geology, v. 28, no. 2, p. 361-380.

Xu, W., and Ruppel, C., 1999, Predicting the occurrence, distribution, and evolution of methane gas hydrate in porous marine sediments: Journal of Geophysical Research, v. 104, p. 5081-5095.

Fracturing Dominated Behavior

Preferential mode of gas invasion in sediments: Grain-scale mechanistic model of coupled multiphase fluid flow and sediment mechanics

Introduction

Gas migration through water-filled soft sediment is an essential component of the dynamics of the seafloor. It governs, for instance, the spatiotemporal characteristics of natural gas seeps and vent sites [Judd et al., 2002; Heeschen et al., 2003; Best et al., 2006], the biochemical processes in the shallow sub-seafloor as well as the ocean floor [Suess et al., 1999], the mechanical and acoustic properties of submarine sediments [Anderson and Hampton, 1980; Anderson et al., 1998; Waite et al., 2008], the creation of pockmarks in the ocean floor [Hovland et al., 2002; Sahling et al., 2008], and the accumulation of gas hydrate (notably methane) in ocean sediments. Understanding gas transport in soft sediments is also key to assessing the viability of carbon dioxide sequestration in the sub-seafloor, either by hydrate formation [Koide et al., 1995, 1997b] or gravitational trapping [Koide et al., 1997a; House et al., 2006; Levine et al., 2007; Goldberg et al., 2008].

Methane hydrates—crystalline ice-like compounds composed of methane molecules caged in a lattice of water molecules [Sloan, 1998]—form naturally at high pressures and low temperatures, like those typical of most of the ocean floor. It is believed that an enormous pool of carbon exists in the form of methane gas and methane hydrate in the ocean floor along the continental margins [Kvenvolden, 1988; Sloan, 2003], although the global estimates of the energy resource are highly uncertain. It also seems likely that this pool of carbon plays an important role in massive submarine landslides [Paull et al., 2003] and in the global carbon cycle [Dickens, 2003]—its sudden or gradual release has been hypothesized to be the cause of past and future climate change [Dickens et al., 1995; Buffett and Archer, 2004; Archer et al., 2009].

Methane hydrate systems in ocean sediments have been the subject of intense research in recent years. A significant component of that effort is directed towards gaining a better conceptual picture of the hydrogeological environment of gas hydrate systems. Particular attention has been devoted to the two end-members [Trehu et al., 2006b]:

1. The hydrogeologically more active, dynamic end-member, exemplified by Hydrate Ridge, offshore Oregon [Suess et al., 1999; Tryon et al., 2002; Heeschen et al., 2003; Trehu et al., 2004b; Weinberger et al., 2005].

2. The hydrogeologically less active, quiescent end-member, illustrated by Blake Ridge, offshore South Carolina [Holbrook et al., 1996; Dickens et al., 1997; Hornbach et al., 2007].

One of the fundamental observations at these two sites is the co-existence of methane hydrate, gas and brine within the hydrate stability zone (HSZ). This is especially noticeable in dynamic environments [Wood et al., 2002; Milkov et al., 2004; Torres et al., 2004; Zühlsdorff and Spiess, 2004; Heeschen et al., 2007; Sahling et al., 2008], but has been observed in low-flux hydrate provinces [Gorman et al., 2002]. It seems clear that, in some geologic settings, methane transport

through the HSZ cannot occur solely as diffusive and advective transport of dissolved methane in the aqueous phase [Torres et al., 2004; Trehu et al., 2004a; Liu and Flemings, 2006].

The scientific community is now undergoing a heated debate as to what are the reasons for co-existence of hydrate and gas [Milkov and Xu, 2005; Torres et al., 2005; Ruppel et al., 2005], which include: (1) kinetics of hydrate formation [Torres et al., 2004]; (2) regional geotherms [Wood et al., 2002]; (3) hypersaline brines as a result of hydrate formation [Milkov et al., 2004]; and (4) fast, focused flow of free gas through fractures and high-permeability conduits [Flemings et al., 2003; Hornbach et al., 2004]. The importance of methane migration as a separate gas phase, and the need to account for multiphase flow effects coupled with hydrate formation, have already been pointed out over a decade ago [Ginsburg and Soloviev, 1997; Soloviev and Ginsburg, 1997].

It has been proposed that free gas accumulation beneath the HSZ may reach a critical thickness to dilate fractures or activate pre-existing faults that will serve as conduits for fast upwards gas migration [Wood et al., 2002; Flemings et al., 2003; Trehu et al., 2004a; Hornbach et al., 2004; Zühlsdorff and Spiess, 2004; Obzhirov et al., 2004; Netzeband et al., 2005; Weinberger and Brown, 2006; Liu and Flemings, 2006, 2007]. Although they did not address the problem at the grain scale, Liu and Flemings [2007] also predicted that at fine grain size and high capillary entry pressure, fracture propagation would dominate the process as gas pressure exceeded the horizontal stress. In this case, it is clear that the study of the hydrate system must be coupled with the mechanical response of the host sediments containing hydrate.

Our hypothesis is that coupling of multiphase fluid flow and sediment mechanics leads—under certain conditions to be described below—to preferential fracturing of the sediment. The creation of these capillary pressure-driven fractures provides fast paths for upwards migration of methane gas through the HSZ, which in turn explains the co-existence of methane gas and hydrate [Behseresht et al., 2008; Jain and Juanes, 2008].

In this paper, we support this hypothesis by developing a mechanistic model at the *grain scale*. We develop a discrete element method (DEM) to model the strong coupling between the pore fluids and the mechanical behavior of the sediment. We rigorously account for the presence of one or more fluids in the pore space by incorporating additional sets of forces due to pore fluid pressures and interfacial tension between the fluids. We demonstrate the DEM's ability to reproduce core-scale behavior, as measured by triaxial laboratory experiments and fluid flow tests. The proposed methodology elucidates the depositional environments (grain size and earth stresses) under which migration of methane gas by fracturing of the sediment is favored over capillary invasion. This determines the distribution of methane gas and hydrate, and the likelihood that gas and hydrate will co-exist. Even though the analysis is done at the grain scale, these results have important implications at the geologic or planetary scale, such as for estimating the magnitude of methane fluxes into the ocean, and the overall size of the hydrate energy resource.

Theory, Formulation and Methods

The Discrete Element Method (DEM) [Cundall and Strack, 1979] has proved a valuable tool to study the mechanisms for deformation and failure of granular materials with variable degree of cementation [Bruno and Nelson, 1991]. Moreover, based on simple geometric arguments, stress variations (and subsequent deformation) have been shown to affect flow properties such as porosity and permeability [Bruno, 1994].

Each element or grain is identified separately by its own mass, moment of inertia and contact

properties. For each grain, its translational and rotational movements are described by solving Newton's second law of motion. The mechanical behavior at the deformation region of grain contact is approximated by introducing a grain contact model, such as a system of a spring, dashpot and slider (Figure 69).

Micromechanics of "dry" media

The movement of a grain is dictated by the net force and moment acting on it. For a *dry model*, that is, one in which pore pressures are negligible, the forces for each grain may include: (1) a contact force $\mathbf{F}_c$ due to the deformation at the grain contacts, (2) a damping force $\mathbf{F}_d$ due to grain non-elastic collisions; (3) an external force $\mathbf{F}_b$ due to gravity and prescribed tractions at the boundaries. The contact force $\mathbf{F}_c$ can be further split into normal and tangential components, $\mathbf{F}_c^n$ and $\mathbf{F}_c^s$, respectively.

The simplest (linear elastic) mechanical behavior at the grain contacts is described by the following equations:

$$F^n = k_n U_n, \quad \Delta F^s = -k_s \Delta U_s, \tag{1}$$

where U_n is the overlap, ΔU_s is the tangential displacement, and k_n and k_s are the normal and shear stiffness at the contact, respectively [ITASCA, 2004; Potyondy and Cundall, 2004]. Inelastic behavior emerges due to either slip between grains, or breakage of contact bonds. Inelasticity is reflected by the constraints:

$$F^s \leq \bar{\mu} F^n, \quad F^n \leq \varphi_n, \quad F^s \leq \varphi_s, \tag{2}$$

where $\bar{\mu}$ is the contact friction coefficient, and φ_n and φ_s are the normal and shear strengths (in force units) of the contact.

Bulk behavior of a granular system is a collective response determined by all the individual grain–grain interactions. For dry sample analyses, the interparticle interactions can be associated with a network of grain–grain contact forces connecting the centroids of grains that are in contact.

Given the set of forces $\mathbf{F}_j$ and moments $\mathbf{M}_j$ acting on the ith particle, its motion is described by the following equations:

$$m_i \ddot{\mathbf{x}}_i = \sum_j \mathbf{F}_j, \tag{3}$$

$$\mathsf{I}_i \ddot{\theta}_i = \sum_j \mathbf{M}_j. \tag{4}$$

Here, $\mathbf{x}_i$ and θ_i are the position vector of the grain centroid and the angle vector of rotation about the centroid; the double dots denote second time derivatives of the position and rotation angle; m_i is the mass; and I_i is the tensor of moments of inertia, respectively. The equations of motion (3)–(4) must be solved simultaneously for all grains in the system via a numerical integration scheme. A commercial three-dimensional DEM code, PFC2D [ITASCA, 2004], was used to integrate these equations in time.

Micromechanical vs. Macroscopic Parameters The parameters that need to be defined at the grain-scale level are ρ_s (grain density), $\bar{\mu}$, k_n, k_s, φ_n and φ_s, as well as the grain size distribution, which we shall characterize simply by the grain radius interval $[r_{\min}, r_{\max}]$.

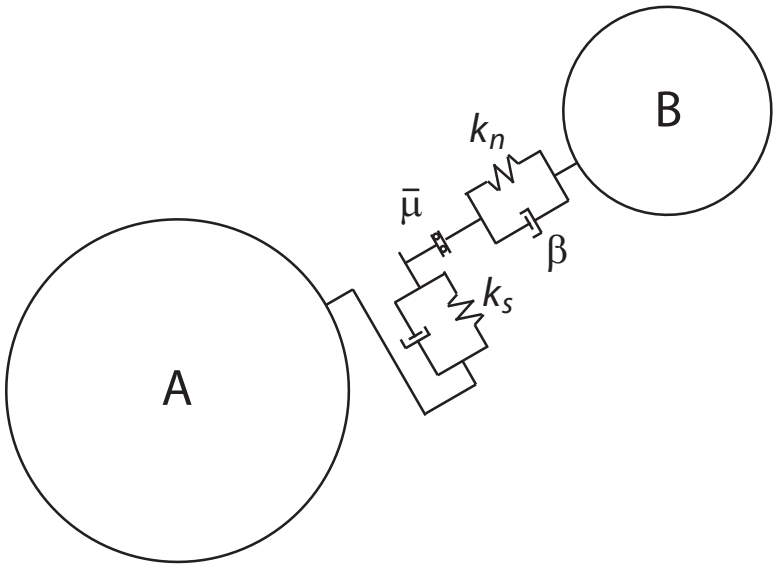

Figure 69: Schematic diagram of a grain–grain contact in a Discrete Element Model. Elastic forces are represented by springs, with normal stiffness k_n and shear stiffness k_s. The contact model includes inelastic and irreversible mechanics through friction (a slider with friction coefficient $\bar{\mu}$), viscous damping (dashpots with damping coefficient β), and bond rupture.

From DEM simulations of biaxial tests, the linear elastic *macroscopic* parameters (Young modulus E and Poisson ratio ν), as well as strength properties (yield stress σ_y, friction angle φ, cohesion c, etc.) may be computed. In order to obtain macroscopic parameters that are independent (or only slightly dependent) on the grain size, the contact strengths must scale with the grain size [Potyondy and Cundall, 2004]:

$$\varphi_n = \bar{\sigma}_c 2 r_g w, \quad \varphi_s = \bar{\tau}_c 2 r_g w, \tag{5}$$

where $\bar{\sigma}_c$ and $\bar{\tau}_c$ are the normal and shear contact strengths (in stress units)—assumed to be independent of grain size—and w is the width of the 2D assembly in the third dimension.

Time Step Selection for Mechanics Simulation Since explicit time integration is used, the time step is bounded by stability considerations. The characteristic time required to capture the dynamics is [ITASCA, 2004]

$$\delta t \sim \sqrt{m/k_n}, \tag{6}$$

where m is the mass of the particle. In PFC2D, grains are assumed to by disks of unit width ($w = 1$ m), so $m = 2\pi r_g^2 w \rho_s$ and, therefore, the critical time step for mechanical stability scales as follows:

$$\delta t_{\text{crit}}^{\text{m}} \sim r_g \sqrt{\rho_s / k_n}. \tag{7}$$

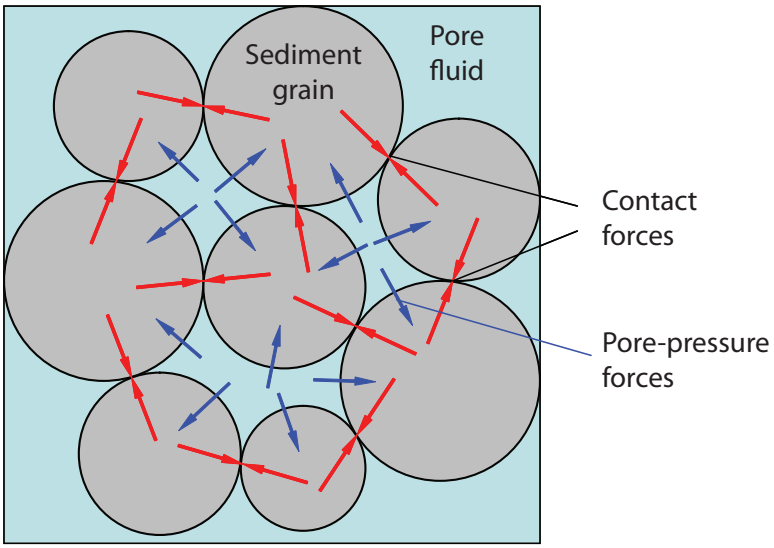

Figure 70: Conceptual picture of the fluid-solid interaction model at the pore scale when a single fluid is present.

Micro-Poromechanics of Single-Fluid Systems

From the theory of poromechanics [Biot, 1941], it is well known that pore pressure will influence mechanical behavior. Essentially, compressive stresses in granular media are transmitted both through a solid skeleton and the pore fluids. Recently, models have been developed to incorporate this effect in DEM with a single-phase pore fluid [Shimizu, 2004; Cook et al., 2004; Li and Holt, 2001, 2004].

When the pore space is filled with a single fluid phase at non-negligible pressure, the associated forces must be incorporated in the model. A conceptual view of the new set of forces is shown in Figure 70. Computationally, the model then consists of two overlapping and interacting networks: the grain network and the fluid network. A particular instance is shown in Figure 71. The force fluid in a given domain exerts on a neighboring grain is obtained by integrating the pressure along the pore–grain contact area. In our implementation, a pressure force is directed from the center of the fluid domain to the grain center. Therefore, pressure forces do not induce rotation.

Consider one particular fluid domain, as sketched in Figure 72. The micromechanical equations can be summarized as follows. The flow rate out of the fluid domain through a pore throat is

$$q_j = C_j \frac{p - p_j}{L_j}, \tag{8}$$

where C_j is the throat conductance, L_j is an effective distance between pore centers, and p, p_j represent the pressures in the fluid domain and its neighbor, respectively. The conductance is inversely proportional to the fluid viscosity μ, and proportional to the square of the effective throat area A_j:

$$C_j = \frac{\tilde{C}_j}{\mu} \frac{A_j^2}{2r_g} w, \tag{9}$$

where $\tilde{C}_j$ is a dimensionless throat conductance. The derivation of this equation from the solution of a Stokes flow problem, and the expressions for $\tilde{C}$ and A, are given in Appendix .

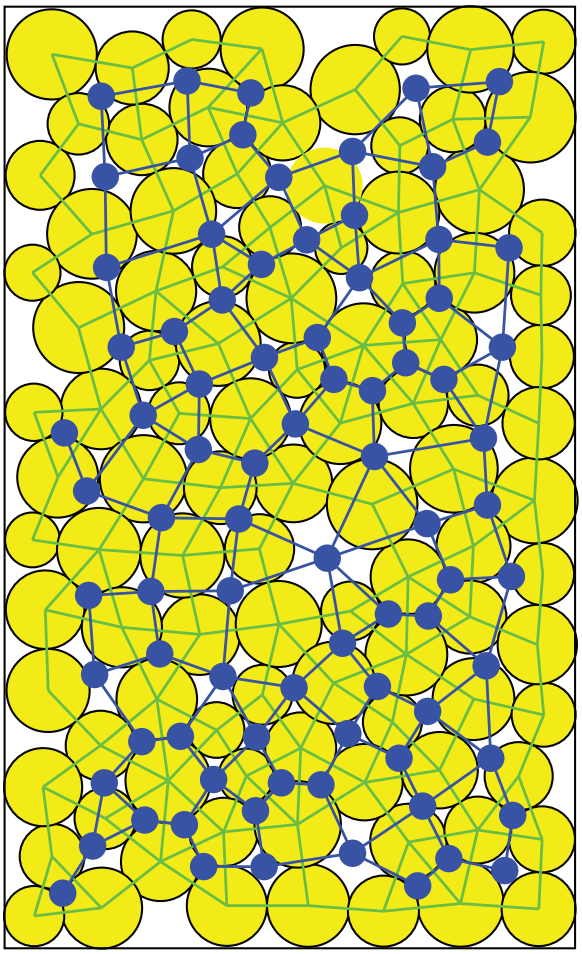

Figure 71: Representation of the grain assembly (yellow circles) and the grain network (green lines). At the center of each fluid domain is a pore body (blue dots), connected by the fluid network (blue lines).

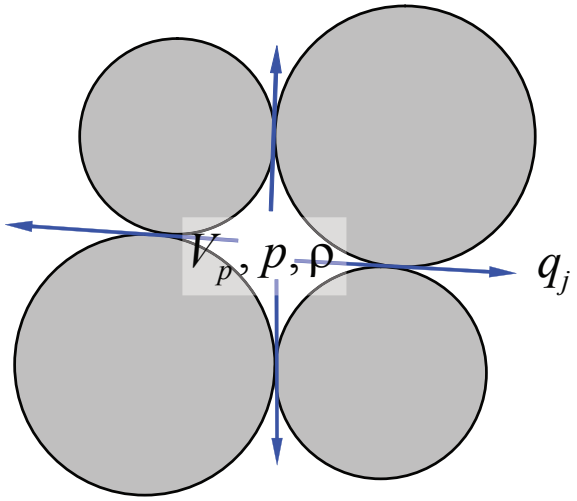

Figure 72: Schematic representation of a fluid domain. At any given time, each fluid domain is characterized by its pore volume V_p, and the pressure p and density ρ of the fluid. Fluid can go in and out of the pore domain at a rate q_j into the neighboring fluid domains.

The grains have certain compressibility, and the radius of a spherical grain varies according to

$$r_g = r_{g,0}\left(1 - \frac{p}{3K_s}\right), \tag{10}$$

where $r_{g,0}$ is the initial radius (at zero fluid pressure), K_s is the bulk modulus of the solid grain, and p is the average of the pore pressures around the grain. Finally, mass balance over a fluid domain gives the following pressure evolution equation for a pore volume V_p:

$$\delta p = \frac{K_f}{V_p}\left(-\delta V_p - \sum_j q_j \delta t\right), \tag{11}$$

where K_f is the fluid bulk modulus, and δp is the pressure variation after a time step δt. The main feature of our model is the term $-\delta V_p$, which accounts for the change in volume of each pore caused by changes in grain locations. This term has been neglected in previous investigations of pore-scale poromechanical models but is essential, for example, to reproduce pressurization of the fluid upon fast compaction. It also reflects the reverse coupling present in Biot's self-consistent theory of poroelasticity.

There is a formal analogy between the micro-poromechanical equations presented above and Biot's self-consistent theory of poroelasticity [Biot, 1941; Wang, 2000]. We expect the DEM formulation will reproduce the linear theory of poroelasticity only in the range of small deformations and small pressure changes. Under such conditions, the poroelastic parameters can then be determined from DEM simulations. When these conditions are not met, nonlinear/irreversible behavior is expected to emerge in the DEM model, driven by contact slip, bond breaking and grain rearrangement.

Time Step Selection For Fluid Flow Simulation The grain-scale fluid flow equations (11) are solved using an explicit time integration scheme. The time step must be restricted for the scheme

to be stable. The characteristic time associated with the microscopic fluid flow dynamics is

$$\delta t \sim \frac{V_p}{K_f} \frac{\delta p}{\sum_j q_j}. \tag{12}$$

Introducing Equations (8) and (9), we express the characteristic time as

$$\delta t \sim \frac{V_p}{K_f} \frac{2 r_g \mu}{w} \sum_j \frac{L_j}{\tilde{C}_j A_j^2}. \tag{13}$$

Using the scaling $V_p \sim r_g^2 w$, and $A \sim r_g^2$, the critical time step for fluid flow stability scales as follows:

$$\delta t_{\text{crit}}^{\text{f}} \sim \frac{\mu}{\tilde{C} K_f}. \tag{14}$$

In a coupled poromechanics simulation, the time step must be smaller than the minimum of the critical values in Equations (7) and (14).

Micro-Poromechanics of Two-Fluid Systems

In the environments of interest for methane hydrates—in particular, at the base of the hydrate stability zone—two fluid phases exist: a liquid brine phase, and methane gas. One of the key differences between single-fluid and two-fluid systems is the presence of a fluid–fluid interface. Due to surface tension effects, the pressures on both sides of the interface (that is, the pressure in the brine and the pressure in the methane gas) can be very different.

The key question is: what is the preferential mode of gas invasion? Two different fundamental mechanisms are at play (Figure 73): (1) capillary-dominated invasion of a rigid solid skeleton, and (2) fracturing of the sediment. While capillarity governs invasion of gas through the porous medium, mechanical effects may lead to deformation and fracturing of the sediment skeleton, thereby triggering invasion when it would otherwise not occur. Preferential fracturing of the sediment requires differences in pressure between neighboring pores. While this is typically not a favored scenario in single-fluid systems (unless a fluid is injected at very fast flow rates and pressures, as in hydraulic fracturing operations), it is natural in two-fluid systems because the two fluids have different pressures. Before the pore is invaded, the pore-pressure forces correspond to the water pressure. Once the pore is invaded by gas, it is the gas pressure that exerts a net force onto the surrounding grains. Since the two fluids do not mix, a pressure difference does not dissipate. This pressure difference may lead to preferential fracturing of the sediment. These processes clearly couple flow and deformation, at both the grain scale and the macroscopic scale.

Capillary Invasion Consider invasion of methane free gas by capillary invasion (Figure 73(middle)). The gas/water interface will invade a throat if the capillary pressure (that is, the difference between gas pressure and water pressure) is larger than the capillary entry pressure [Richards, 1931; Leverett, 1941; Mayer and Stowe, 1965]. The capillary entry pressure is proportional to the interfacial tension γ, and inversely proportional to the throat opening. Let d be the throat gap (which, in a 2D model, may be negative if there is overlap between the grains). In Appendix , we derive the

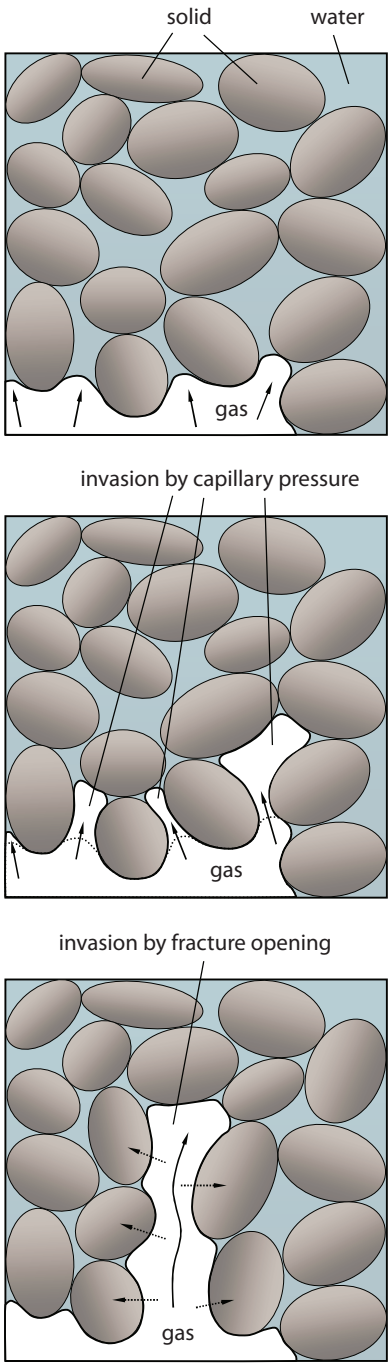

Figure 73: Schematic diagram of the two modes of methane gas invading a sediment. **Top:** before invasion, the gas–water interface of a buoyant gas plume underlies water-filled sediment. **Middle:** invasion will occur if the capillary pressure (the difference between gas pressure and water pressure) exceeds the capillary entry pressure, which is inversely proportional to the pore diameter. **Bottom:** invasion by fracture opening; if the exerted pressure is sufficient to overcome compression and friction at grain contacts, a fracture will form. In a multiphase environment, due to surface tension effects, the pressure difference between water and gas will *not* dissipate quickly through the porous medium, and water at grain contacts will increase cohesion.

following expression for the gas pressure to invade a throat:

$$p_g - p_w \geq \frac{2}{\sqrt{1 + \left(1 + \frac{d}{2r_g}\right)^2 - 1}} \frac{\gamma}{r_g}. \tag{15}$$

Fracture Opening Clearly, if the grain size is large, the process of capillary invasion is favored and gas invasion can occur even if the porous medium is rigid. In this case, the gas invasion pressure into the sediment is given by Equation (15). On the other hand, for small grain size (high capillary entry pressures), gas invasion will not occur until the grains are pushed apart (Figure 73(bottom)).

For an idealized scenario of cohesionless material under undrained plane-strain conditions, a fracture will propagate when the gas pressure exceeds the minimum compressive stress (assumed horizontal):

$$p_g - \sigma_H \geq 0. \tag{16}$$

This condition of fracture opening must be extended to the case when cohesion $\bar{\sigma}_c$ exists. In porous media filled with a single fluid, the source of cohesion (tensile strength) is grain cementation and consolidation. When the pore space is occupied by two fluids of different wettability, capillary forces induce additional adhesion between particles (Figure 74) [Orr et al., 1975; Lian et al., 1993; Cho and Santamarina, 2001].

Because there is stress concentration at the fracture tip, the fracturing pressure depends not only on the earth stresses and the cohesive stress, but also the fracture's length. In the realm of linear elastic fracture mechanics (LEFM), the fracturing pressure is

$$p_g - \sigma_H \geq C_{\text{LEFM}} \frac{K_{Ic}}{\sqrt{\pi a}}, \tag{17}$$

where K_{Ic} is the fracture toughness, a is the length of the fracture, and C_{LEFM} is a coefficient that depends on the geometry, the ratio of horizontal to vertical stresses, and loading conditions [Anderson, 1991]. In the context of particle assemblies, the "measurable" fracture toughness depends on the cohesive strength (and, therefore, on the interfacial tension between fluids) and on the grain size. This last dependency emanates from the observation that the internal lengthscale in the fracture toughness is determined by the grain size [Potyondy and Cundall, 2004]. Therefore, under the assumptions of LEFM, the gas pressure for fracture opening takes the form:

$$p_g - \sigma_H \geq C_{\text{LEFM}} \frac{\gamma \sqrt{r_g}}{r_g \sqrt{\pi a}}. \tag{18}$$

Even though LEFM conditions do not apply to natural sediments, Equation (18) indicates that asymptotically, $p_g^{\text{frac}} - \sigma_H \sim r_g^{-1/2}$. Equation (15) says that the gas pressure for capillary invasion scales like $p_g^{\text{cap}} - p_w \sim r_g^{-1}$. Both invasion pressures increase as the grain size decreases, but the capillary invasion pressure increases faster. This analysis suggests that fracturing is favored over capillary invasion for fine-grained sediments.

In any case, we do *not* use LEFM. It is the nonlinear evolution of the DEM micro-poromechanical model that determines when bonds break, and when the gap between grains is large enough for

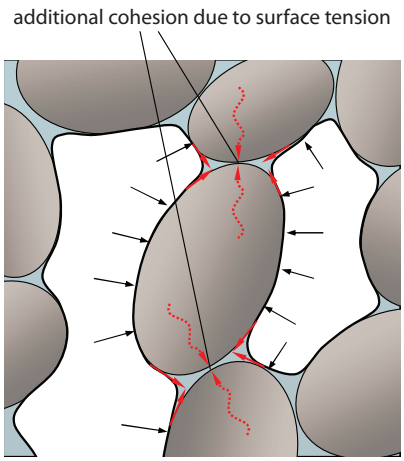

Figure 74: Meniscus pinning in the presence of two fluid phases in the sediment. During multiphase flow in porous media, the least wetting phase (gas, white) migrates through the center of the pores, while the most wetting phase (brine, blue) coats the grains (gray) and forms filaments around the crevices of the pore space. This configuration leads to gas–water menisci around the grain contacts. Due to interfacial tension (solid red arrows), these menisci are responsible for an attraction force between grains (dotted red arrows). At the macroscopic level, this can be interpreted as an increment in the cohesion of the material. This is a purely multiphase-flow effect, not present in single-phase poromechanics.

the gas interface to advance, according to Equation (15). In this fashion, the gas/water interface advances and a new pore is loaded with a higher pressure. The implementation of multi-fluid poromechanics is therefore very similar to that of single-fluid systems, except that the key hydraulic property (the conductance between pore bodies) is set to zero until condition (15) is satisfied.

Capillary invasion and fracture opening are the two end-member mechanisms for methane transport in its own gas phase, and our coupled grain-scale model allows us to investigate the competition between the two as a function of grain size, earth stresses, and sediment cohesion.

Results

Micromechanics of "Dry" Media

Sediment Model Generation and Initialization A model sediment is generated by first choosing the number of particles, and reproducing the desired grain size distribution. As we shall see below, several macroscopic properties (both mechanical and fluid-flow properties) are dependent on the grain size. Therefore, it is important that the sediment model either reproduces the desired grain size distribution, or that the assigned microproperties (e.g. bond strength) reflect the disparity in grain size [Potyondy and Cundall, 2004]. In most of the examples shown in this paper, we have chosen a relatively narrow, uniform grain radius distribution $[r_{\min}, r_{\max}]$, with $r_{\max} = (5/3)r_{\min}$.

The particles are randomly placed in a box and allowed to fall under gravity, simulating sedimentation (Figure 75). The settling process has two differentiating stages: (1) free fall under gravity, with limited grain–grain interaction, and (2) settling and grain rearrangement until static conditions are reached.

The time step is larger initially, during the "free fall" stage, and quickly converges to the value required for stability of the dynamical system dominated by grain–grain interactions. The time step is proportional to the grain radius, and inversely proportional to the square root of the grain stiffness, confirming the stability condition of Equation (7).

Uniaxial Compaction for "Dry" Media Here we show that DEM simulations of "dry" media (infinitely compressible pore fluid) are able to capture the mechanical behavior of real sediments. In Figure 76 we plot experimental stress–strain curves of sediment samples from Hydrate Ridge [Tan et al., 2006] along with curves from DEM simulations. The data come from triaxial tests that reproduce constant rate of strain (CRS) conditions, in which the lateral stress was also measured. The DEM model was created by sedimenting particles, and applying an isotropic confining stress of 20kPa, to start the uniaxial vertical compaction test at the same stress level as the experiments [Tan, 2004]. The only parameter that we varied to reproduce measured stress–strain behavior was the grain stiffness k_n. The rest of the micromechanical parameters are as follows: $k_s = k_n$, $\bar{\mu} = 0.5$, $\bar{\sigma}_c = \bar{\tau}_c = 0$.

The DEM simulations match the stress–strain behavior measured in the lab even for very high deformations (up to 16% strain), capturing the material nonlinearity. For an undisturbed ideal clay sample, the initial portion of the strain–log stress curve would be a straight line with slope equal to the unload/reload loop slope until reaching its preconsolidation stress. After this point, the slope would change to the virgin consolidation line slope. The Hydrate Ridge samples exhibit a large "rollover" at small strains (in the plot of vertical strain versus effective vertical stress on a

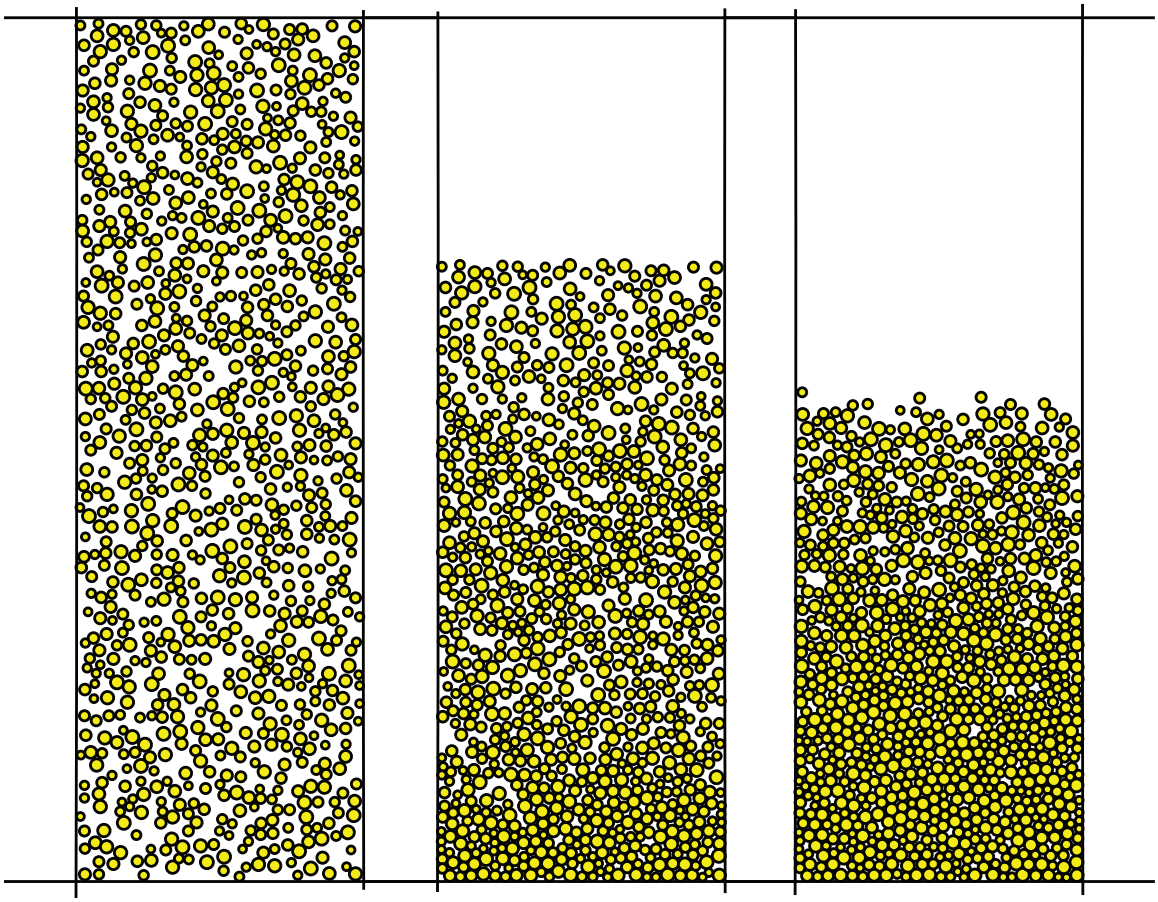

Figure 75: Snapshots of the particle settling process.

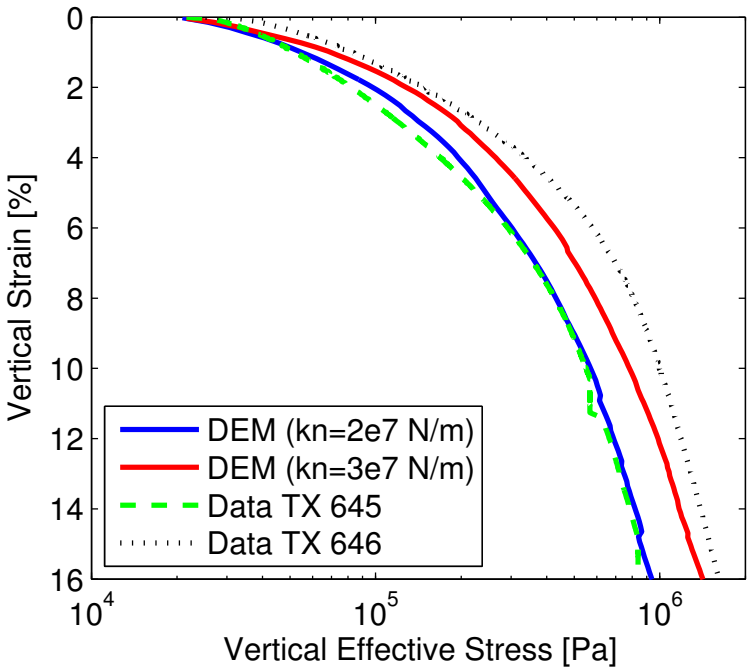

Figure 76: Experimental stress–strain curves for sediments from Hydrate Ridge [Tan et al., 2006], and comparison with DEM simulations for two different values of the grain stiffness.

logarithmic scale) because they are highly disturbed [Tan, 2004]. For the purpose of validation of the DEM model, the relevant portion of the curve is that above the pre-consolidation stress.

Although we do not show it here, the DEM model also displays irreversible behavior in that loading/unloading cycles show hysteresis. However, it is unable to reflect the dramatic increase in stiffness upon unloading that the data show [Jain and Juanes, 2008].

We also compared the lateral-to-vertical stress ratio, K_0, predicted by the DEM model with the values measured for Hydrate Ridge sediment samples [Tan et al., 2006]. The stress ratio is measured during 1D consolidation in triaxial cells. In preparation for the test, and to make sure the sample is fully saturated, initial vertical and horizontal effective stresses were brought to about 20kPa (which is small enough that there is not significant strain) to remove any bubbles from the sample. To reproduce these conditions, we isotropically consolidated the DEM samples to 20kPa as well prior to performing the 1D consolidation. Therefore, the initial K_0 value is 1. We used the same grain stiffness parameters employed to match the lab stress–strain behavior (Figure 76), and let the DEM model predict the evolution of the K_0 ratio for those experimental conditions (Figure 77). While the agreement between model and experiments is generally good, the experimentally-measured values drop down to about 0.5, while those predicted by the DEM model drop to about 0.6.

Micro-Poromechanics of Single-Fluid Systems

Uniaxial Fluid Flow In this section, we evaluate the fluid flow capabilities of the grain-scale model. We do so by simulating a one-dimensional fluid flow problem in a cell with drained top and bottom boundaries, and impervious fixed lateral boundaries. The initial pressure is constant,

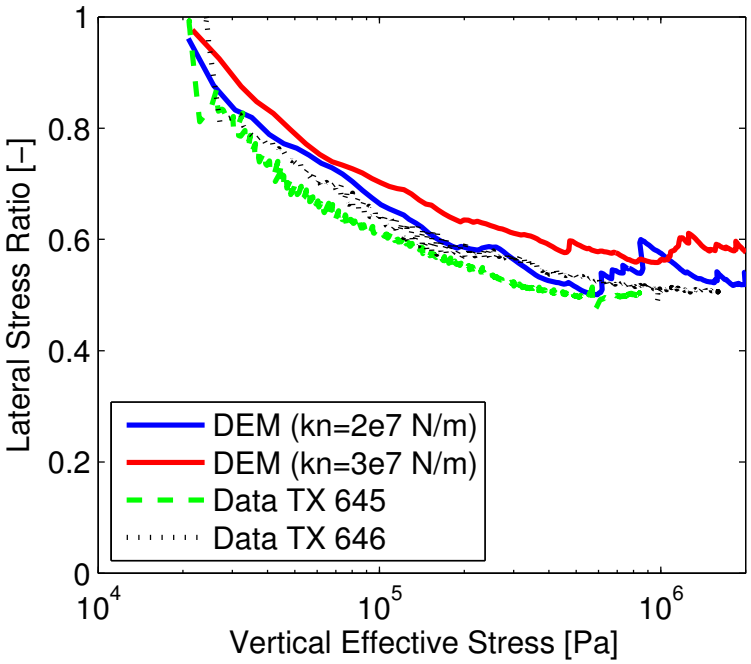

Figure 77: Experimental lateral-to-vertical stress ratio curves for sediments from Hydrate Ridge [Tan et al., 2006], and comparison with DEM simulations for the same values of grain stiffness used to match the vertical stress–strain behavior in Figure 76.

and equal to the boundary pressures. Suddenly, a pressure change is applied to the top boundary, and we simulate the evolution of the pressure and fluid inflow/outflow until a new steady state is reached. The continuum problem is described mathematically by the partial differential equation:

$$c_v \frac{\partial p}{\partial t} - \frac{k}{\mu}\frac{\partial^2 p}{\partial x^2} = 0, \quad 0 < x < H, \tag{19}$$

where x is elevation, H is the height of the cell, k is the intrinsic permeability, μ is the fluid viscosity, and c_v is the consolidation coefficient [Wang, 2000]. The initial condition is given by:

$$p(x,0) = 0, \quad 0 \le x \le H, \tag{20}$$

and the boundary conditions are:

$$p(0,t) = 0, \quad p(H,t) = \Delta p, \quad t > 0. \tag{21}$$

The problem can be expressed in dimensionless form by defining the following dimensionless quantities:

$$\begin{aligned}
\text{distance}: &\quad \xi = \frac{x}{H}, \\
\text{time}: &\quad \tau = \frac{t}{T_c}, \quad T_c = \frac{c_v \mu H^2}{k}, \\
\text{pressure}: &\quad p_D = \frac{p}{\Delta p}, \\
\text{flowrate}: &\quad Q_D = \frac{Q}{Q_c}, \quad Q_c = \frac{k}{\mu}\frac{\Delta p}{H} W w,
\end{aligned}$$

where W is the width and w is the thickness of the cell (that is, the dimensions of the cell in the directions perpendicular to the flow). The analytical solution to the problem can be found by the method of separation of variables [Crank, 1975]. The dimensionless pressure field is given by:

$$p_D(\xi,\tau) = \xi + \frac{2}{\pi}\sum_{n=1}^{\infty}\frac{(-1)^n}{n}\sin(n\pi\xi)\exp(-(n\pi)^2\tau). \tag{22}$$

By differentiating the expression above, we find the expression for the dimensionless flow rate in and out of the cell:

$$Q_D^{\text{in}} = 1 + 2\sum_{n=1}^{\infty}(-1)^n\cos(n\pi)\exp(-(n\pi)^2\tau), \tag{23}$$

$$Q_D^{\text{out}} = 1 + 2\sum_{n=1}^{\infty}(-1)^n\exp(-(n\pi)^2\tau). \tag{24}$$

The objective is to determine whether the grain-scale model reproduces the macroscopic behavior. The relevant macroscopic parameters are the intrinsic permeability k and the consolidation coefficient c_v. The intrinsic permeability is obtained by matching the flow rate at steady state. The consolidation coefficient is determined by matching the dimensionless inflow and outflow curves.

We generated an assembly with 1000 grains, and a minimum radius $r_{\min} = 1$ cm. The vertical and horizontal dimensions of the cell are, approximately, $H = 1$ m and $W = 0.7$ m. We set the pressure increment Δp to a small value, so that the effects of pore pressure on the mechanical deformation are minimal. Once the flow stabilizes, inflow and outflow rates are equal to Q_c, and the intrinsic permeability of the medium can be computed as:

$$k = \frac{\mu H Q_c}{W w \Delta p}. \tag{25}$$

The characteristic time T_c is then obtained by matching the numerical inflow and outflow curves, from which the macroscopic consolidation coefficient is computed as:

$$c_v = \frac{kT_c}{\mu H^2}. \tag{26}$$

In Figure 78 we plot the dimensionless inflow and outflow rates as a function of dimensionless time. The agreement between the DEM results and the analytical solution is excellent, indicating the flow formulation accurately captures the macroscopic behavior (Darcy flow in porous media). As a further validation of the model, we compare in Figure 79 the evolution of dimensionless pore pressure within the sample. By plotting the pressure values from the DEM simulation at individual pores, we obtain a scattered profile of the average pressure as a function of depth. We compare these results with the analytical solution at different dimensionless times. Again, the agreement is excellent.

By repeating the fluid flow simulations with different values of $r_{\min}$, we determine the dependence of the hydraulic and poromechanical parameters on grain size. The results are compiled in Table 1, where we confirm that the intrinsic permeability scales with the square of the grain size (as expected from Stokes theory, and the Kozeny–Carman relation for granular materials). Moreover, if the fluid is significantly more compressible that the skeleton, the DEM simulations also reflect that the effective consolidation coefficient c_v is inversely proportional to K_f, with the constant of proportionality being approximately equal to the porosity [Wang, 2000].

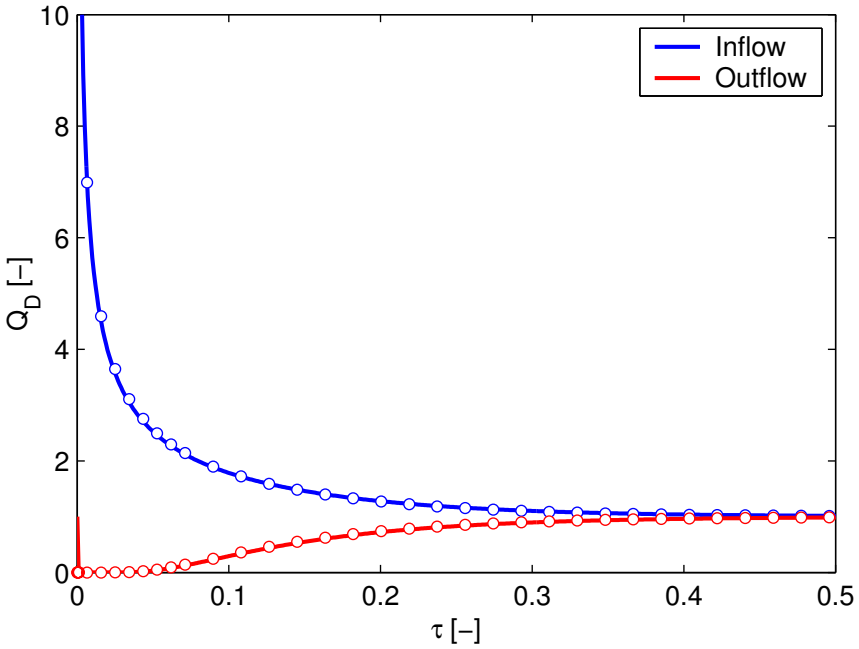

Figure 78: Inflow and outflow rates into the pressure cell. Comparison of DEM simulation (circles) and analytical solution (solid line).

Table 1: Macroscopic hydraulic and poromechanical parameters for different grain size distributions.

$r_{\min}$ [m]	k [m^2]	c_v/K_f [-]
0.01	0.289×10^{-6}	0.161
0.001	0.289×10^{-8}	0.156

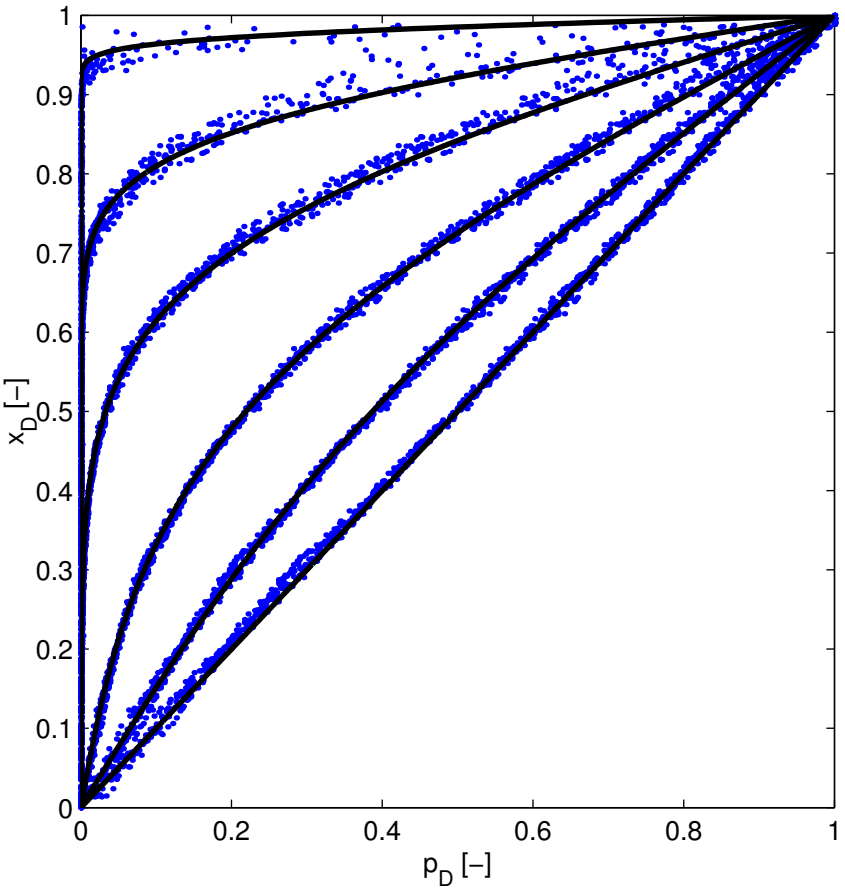

Figure 79: Evolution of pressure profiles during the uniaxial fluid flow test. Comparison of DEM simulation (dots) and analytical solution (solid line) at different dimensionless times: $\tau = 0.000242$, 0.00671, 0.0275, 0.0829, 0.175, 1.404.

Uniaxial Undrained Compaction A sensitive test of the DEM coupled model's validity is fluid–solid behavior during undrained consolidation tests. A sediment model is initialized by gravitational settling. Then the walls are adjusted to achieve an isotropic confining stress state of 0.1MPa (above atmospheric pressure). Until that point, the fluid is allowed to drain and the pore pressure is atmospheric ($p = 0$). Thus, the initial effective stress is 0.1MPa. After that, the sample is sealed so that no fluid is allowed to drain, and it is subjected to uniaxial compaction. During the undrained compaction process, the vertical strain ε, total vertical stress σ, and average pore pressure p are recorded. In view of the effective stress concept [Terzaghi, 1943; Biot, 1941], the total stress required to achieve a given deformation in a fluid-saturated medium is larger than for a dry medium. In the realm of the linear theory of poroelasticity, the *effective stress* is given by:

$$\sigma' = \sigma - bp, \tag{27}$$

where b is the Biot coefficient. The dependence of the Biot coefficient on the solid and fluid properties of the constituents is reasonably well understood [Coussy, 1995; Wang, 2000]. The Biot coefficient approaches a value of one only in the limit of incompressible grains and point grain–grain contacts. If the grain and fluid compressibilities are comparable, the Biot coefficient is less than one.

We used an assembly with 1000 grains, $r_{\min} = 0.01$ m, $k_n = 10^7$ N/m, $k_n/k_s = 2.5$, and $K_f = 10^7$ Pa. In Figure 80 we show the stress–strain curves for a cemented/cohesive sample (bond strength $\bar{\sigma}_c = \bar{\tau}_c = 10^6$ Pa—left figure), and for an unconsolidated/cohesionless sample (bond strength $\bar{\sigma}_c = \bar{\tau}_c = 10^2$ Pa—right figure). In both cases, we plot the stress–strain curves for the fluid-saturated medium (total stress), and for a dry medium. We confirm that the dry stress curve can be interpreted as the effective stress, and recovered by subtracting the pore pressure times the Biot coefficient from the total stress. We infer the Biot coefficient in this way, and the values obtained agree well with experimental values [Wang, 2000, Table C.1].

Micro-Poromechanics of Two-Fluid Systems

Migration of a gas phase through a deformable medium may occur by two end-member mechanisms: (1) capillary invasion through a rigid medium, and (2) fracture opening. Our DEM model is capable of reproducing *both* mechanisms, and can therefore predict the conditions under which one is favored over the other, and predict gas migration as a result of their *combined* effect.

Capturing the Fracturing Phenomenon We first illustrate that our DEM model of coupled two-phase fluid flow and grain mechanics can reproduce fracture initiation and propagation upon invasion of an immiscible gas phase.

In many (passive) depositional environments, the horizontal stress is lower than the vertical stress. In such scenarios, one expects the development of vertical fractures that open up the sediment in the direction of minimum compressive stress. In Figure 81 we show that fracturing of the sediment is not necessarily restricted to anisotropic earth stresses. Even when horizontal and vertical stresses are equal, the medium tends to fracture in a set of radial, geometrically complex fractures if gas is injected into a brine-saturated sediment.

Fracturing vs. Capillary Invasion: Influence of Grain Size We find the most sensitive factor in determining the mode of methane gas transport (sediment fracturing or capillary invasion) is the

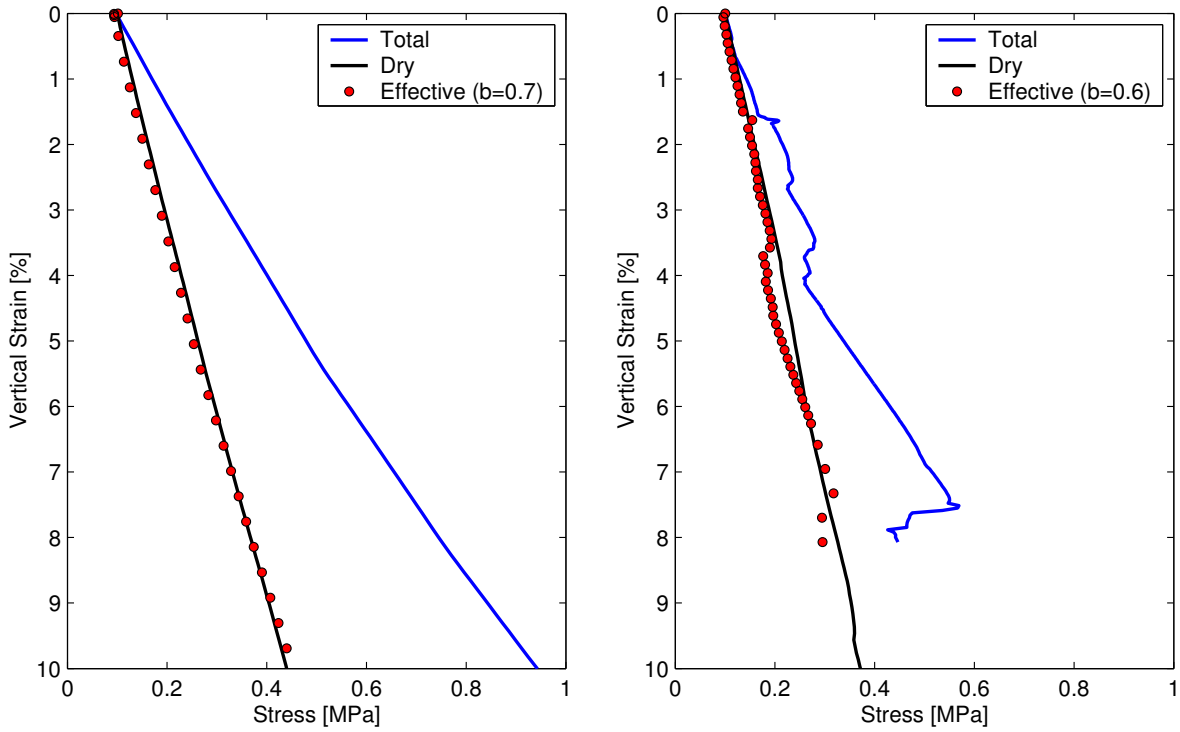

Figure 80: Stress–strain curves for uniaxial undrained compaction. The total stress in the fluid-filled sample (blue solid line) is higher than the stress in the "dry" sample (black solid line). The effective stress curve (red circles) is obtained by subtracting the pore pressure (not plotted) premultiplied by the Biot coefficient from the total stress. An appropriate value of the Biot coefficient is found by matching the effective stress curve with the "dry" stress curve. Left: cemented/cohesive sample. Right: unconsolidated/cohesionless sample.

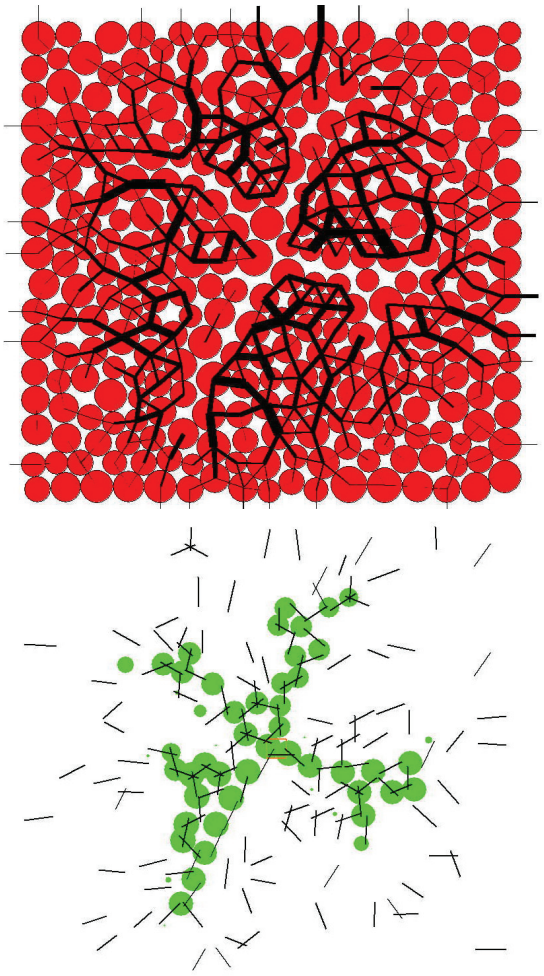

Figure 81: Illustration of the fracturing behavior of a model sediment upon injection of gas, when the vertical and horizontal stresses are equal. The sediment fractures "isotropically" into a set of radial, geometrically-complex fractures. Top: The grain assembly (red circles) after fracturing due to "injection" of gas at the center of the domain. The thick black lines denote compressive forces at the grain–grain contacts. Note that they are missing from the fractured areas. Bottom: Representation of the pores occupied by the injected gas (green circles). The thin black lines indicate grain–grain contacts that have exceeded the contact strength and have therefore "broken". Note the complementary nature of this set of lines to that of the force network above.

grain size: fracturing is favored for fine-grained sediments, while capillary invasion is favored for coarse-grained sediments. Here we illustrate these two end-members.

The simulation is set up as follows. A sample of 300 grains of grain size $[r_{\min}, 2r_{\min}]$ is generated by gravitational settling. Since the sample size is much smaller than a representative elementary volume of sediment, we only simulate a narrow range of grain sizes at a time. The lateral boundaries are fixed. The sediment is then compacted vertically under constant pore pressure until a vertical effective stress of 3MPa is achieved. This level of vertical effective stress corresponds to a depth of about 300m below seafloor. During this vertical compaction, the horizontal effective stress increases to a value of about 1.6MPa, that is, $K_0 \approx 0.53$. Inasmuch gravity effects are negligible in a grain-scale model, the results are independent of water depth; they depend on the relative magnitudes of capillary pressure (the difference between gas pressure and water pressure) and *effective* stress (the difference between the total stress and the pore pressure).

The interfacial tension is $\gamma = 50 \times 10^{-3}$ N/m. We assume that the cohesion is inversely proportional to grain radius. This is phenomenologically adequate (fine-grained material like clays are cohesive) and is also consistent with the adhesive forces that result from the presence of a gas–water interface [Kato et al., 2004]. For simplicity, we take $\bar{\sigma}_c = 2\gamma/r_g$. The only parameter that is left free is the grain size $r_{\min}$.

During the simulation, we inject gas at the bottom center pore. We incrementally increase the gas pressure. Between each increment, we allow sufficient time to pass for fluid flow and granular displacements to stabilize, so mechanical equilibrium is reached.

In Figure 82 we show two snapshots of the evolution of the methane–water interface for a coarse-grain sediment of characteristic size $r_{\min} = 50$ μm. It is apparent that during the invasion of methane gas, there is virtually no movement of the solid grains: the sediment acts like a rigid skeleton. Indeed, the network of grain contact compressive forces remains the same during the process. Invasion of gas from pore to pore occurs when the gas pressure (minus the water pressure) exceeds the capillary entry pressure of the throat (Equation (15)). In this case, the capillary entry pressure is much lower than the fracturing pressure (the left figure corresponds to $P_c \approx 5$ kPa), and fluid transport is well described by *invasion percolation* [Wilkinson and Willemsen, 1983; Lenormand et al., 1988]. Ultimately, if the gas pressure is sufficiently high, almost all the pores have been invaded by methane gas. In this case, this occurs at a slightly higher capillary entry pressure of $P_c \approx 6$ kPa.

The behavior is completely different when a much smaller grain size is used. The evolution of the methane gas migration for $r_{\min} = 0.1$ μm is shown in Figure 83. The range of capillary entry pressure for the initial configuration is now in the order of 3MPa. However, at this pressure, mechanical effects become dominant, and the solid skeleton no longer behaves like a rigid medium. At $P_c \approx 2.5$ MPa, the invading gas starts to initiate a fracture, with its characteristic stress concentration at the fracture tip captured by the DEM model [Potyondy and Cundall, 2004]. The fracture propagates vertically. The value of the capillary pressure needed to open the fracture corresponds to a gas column thickness of about 300m below the base of the HSZ. Gas column thicknesses of this magnitude have been observed in similar geologic environments [Holbrook et al., 1996; Hornbach et al., 2004], and interpreted as the cause of critical pressures for gas migration through faults [Flemings et al., 2003; Hornbach et al., 2004; Trehu et al., 2004a].

Our grain-scale model explains why focused gas flow can occur by means of fracture opening, even in the absence of pre-existing faults and fractures. It is likely, however, that our model overestimates the invasion capillary pressure required for fracturing, due to boundary effects. This can

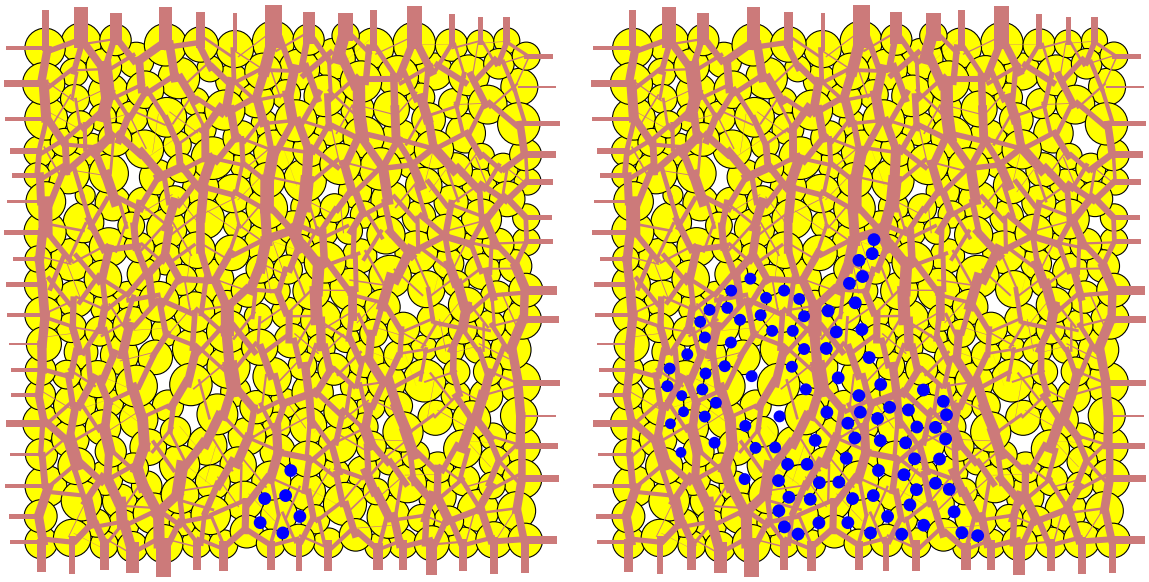

Figure 82: Snapshots of the evolution of the methane gas-water interface for the case $r_{min} = 50\mu\text{m}$. The pores occupied fully by gas are represented with blue dots at the pore centers. The maroon lines indicate compression at grain-grain contacts. The green lines represent tension, which is supported by cohesion between grains. Left: $P_c = 5$ kPa. Right: $P_c = 6$ kPa.

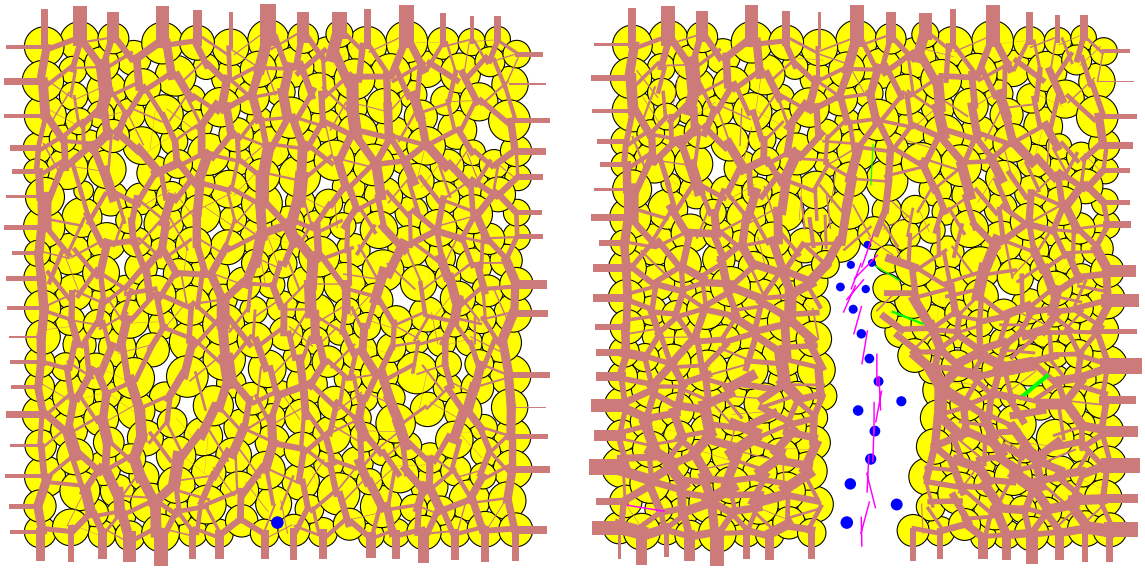

Figure 83: Snapshots of the evolution of the methane gas-water interface for an assembly with $r_{min} = 0.1$ μm. The pores occupied fully by gas are represented with blue dots at the pore centers. The maroon lines indicate compression at grain-grain contacts. The green lines represent tension, which is supported by cohesion between grains. The pink lines show where cohesive bonds were broken. Left: $P_c = 2.5$ MPa. Right: $P_c = 2.55$ MPa.

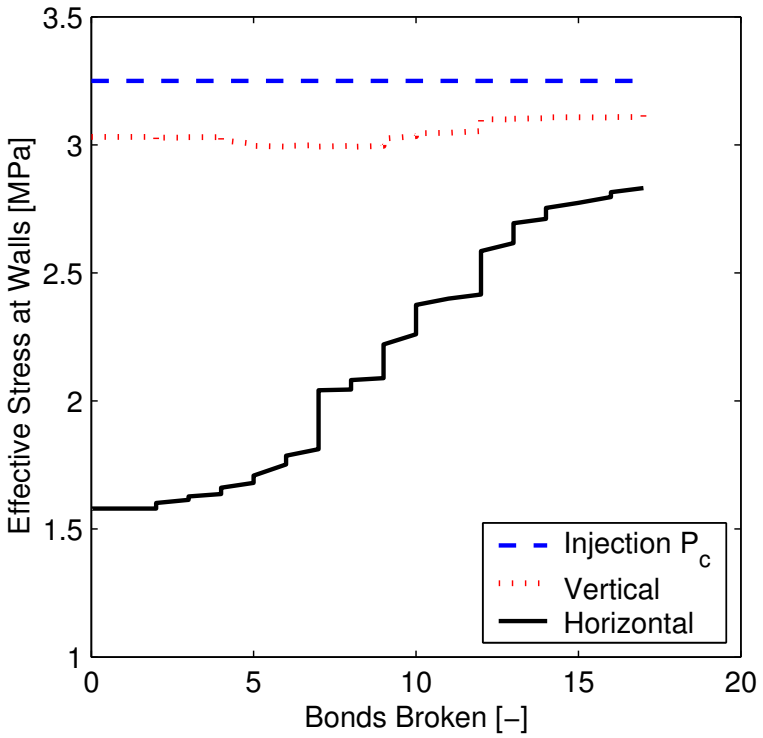

Figure 84: Evolution of the vertical and horizontal mean effective stress during fracture propagation for the simulation shown in Figure 83. The invading gas pressure remains constant throughout, but the vertical and, especially, the horizontal stress at the boundaries increase during fracture growth. The boundaries introduce an artificial stiffness in the problem that results in an overestimation of the gas invasion pressure.

be seen from the grain forces on the lateral boundaries in Figure 83, which change significantly as the fracture propagates. This is confirmed by the increase of the vertical and, especially, horizontal mean effective stress during fracture growth (Figure 84). The presence of computational boundaries near the propagating fracture introduces an artificial stiffness to the problem.

Discussion and Conclusions

We have presented a discrete element model for simulating, at the grain scale, gas migration in brine-saturated deformable media. The model has been validated for many processes, including: (1) generating sediment models by gravitational settling and compaction; (2) stress–strain behavior of ocean sediments; (3) transient single-phase flow for determining hydraulic parameters; (4) undrained compaction tests for determining poromechanical parameters.

The coupled model permits investigating an essential process that takes place at the base of the hydrate stability zone: the upward migration of methane in its own free gas phase. We elucidate the two ways in which gas migration may take place: (1) by capillary invasion in a rigid-like medium; and (2) by initiation and propagation of a fracture.

Each end member can be analyzed separately, and conditions for gas invasion can be found for the capillary-dominated and fracture-dominated regimes. We find the main factors controlling the

mode of gas transport in the sediment are the grain size and the effective confining stress. We have shown that coarse-grain sediments favor capillary invasion, whereas fracturing dominates in fine-grain media. Recent laboratory experiments of gas invasion and bubble growth in soft, fine-grained sediments provide convincing evidence that fracturing is a relevant mechanism for gas transport [Boudreau et al., 2005; Best et al., 2006]. The cornflake-shaped, subvertical fractures observed in those experiments are strikingly similar to those simulated with the mechanistic grain-scale model presented here.

The significant contribution of our coupled model is that it captures both phenomena and, as a result, allows us to study the transition between the two regimes. We synthesize the transition from capillary invasion to fracture opening in Figure 85. We plot the gas pressure required for invasion into a sediment at an effective confining stress of 3MPa (typical of a sediment-column depth of about 300m) as a function of grain size. For sufficiently coarse grain size, gas invades by capillarity. According to Equation (15), the invasion capillary pressure for this regime decreases with increasing grain size, and has the following scaling:

$$P_c^{\mathrm{cap}} \sim r_g^{-1}. \tag{28}$$

This scaling is clearly confirmed by our DEM simulations, which collapse onto a straight line of slope -1 on the log-log plot of P_c vs. r_g.

There exists a critical grain size, in this case $r_g \approx 0.1\ \mu\mathrm{m}$, at which the transition from capillary invasion to fracturing occurs. For grain sizes below this critical value, invasion is *always* by fracture opening. The pressure required for opening a fracture, however, does depend on grain size. Under LEFM conditions, the expected scaling from Equation (18) is:

$$P_c^{\mathrm{frac}} - \sigma'_H \sim r_g^{-1/2}, \tag{29}$$

which corresponds to a straight line of slope $-1/2$. This behavior is *not* confirmed by our grain-scale model, which accounts for the coupling between two-phase flow and *inelastic* grain-scale mechanics. This suggests that inelastic and capillary effects are essential in the fracturing process.

These emergent phenomena have important implications for understanding hydrates in natural systems (either ocean sediments and permafrost regions). Our model predicts that, in fine sediments, hydrate will likely form in veins that follow a fracture-network pattern. Since the mechanism of fracture propagation is self-reinforcing, our results indicate that it is possible, and even likely, that methane gas will penetrate deeply into the HSZ (and maybe all the way to the ground surface).

Our model supports the view that, in coarse sediments, the buoyant methane gas is likely to invade the pore space more uniformly, in a process akin to invasion percolation. While this is definitely affected by heterogeneity in grain-size distribution, the overall pore occupancy is likely to be higher than for a fracture-dominated regime, leading to larger time scales for transport. The predictions from our model are consistent with field observations of hydrates in natural systems [Suess et al., 1999; Sassen et al., 2001; Flemings et al., 2003; Trehu et al., 2004a; Hornbach et al., 2004; Trehu et al., 2006a; Riedel et al., 2006; Weinberger and Brown, 2006; Liu and Flemings, 2006, 2007; Collett et al., 2008].

We have not undertaken here an analysis on the relative importance of transport in solution versus as a separate free gas phase flowing through fractures. However, the importance of free

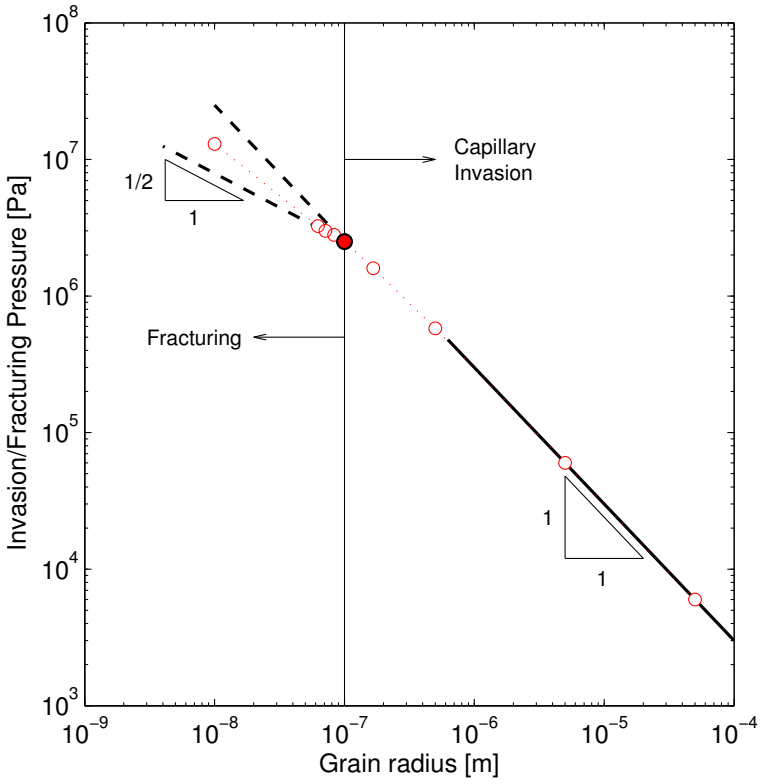

Figure 85: Plot of invasion pressure vs. grain size (red circles) for a sediment under 3MPa vertical effective stress (sediment column depth of about 300m). The red-filled circle denotes the critical grain size at which the transition in the mode of gas invasion occurs. For larger grain size, gas invades by capillarity. For smaller grain size, it invades by opening a fracture. In the capillarity-dominated regime, the invasion capillary pressure decreases with increasing grain size with a slope of -1 (black solid line), consistent with the theory (Equation (28). In the fracture-dominated regime, the invasion capillary pressure increases with decreasing grain size, though the predictions of linear elastic fracture mechanics (black dashed line with slope $-1/2$) are not in agreement with our coupled grain-scale model. This suggests the effects of capillarity and inelastic material behavior cannot be neglected.

gas fluxes through fractures is demonstrated by the massive free methane gas venting rates observed intermittently at northern Hydrate Ridge [Torres et al., 2002]. Tryon et al. [1999, 2002] hypothesized that fracture networks rapidly transport the gas from beneath the HSZ to the vents, a distance of 70–100m. The total methane flux coming out of 10 discrete vents ($\sim$1cm diameter each), clustered in a depression several meters in diameter, constitutes two-thirds of the total flux, calculated from seawater methane concentrations in the overlying water column [Heeschen et al., 2005]. Acoustic imaging shows massive bubble plumes at two other sites in the region [Heeschen et al., 2005], which likely account for the remaining one-third of the flux to the water column. Free gas ebullition through vents fed by fractures releases methane from the sea floor at rates many orders of magnitude faster than transport by advection of dissolved methane in solution through sediments [Torres et al., 2002]. In terms of velocities, the gas bubbles exit conduits episodically at about 1m/s [Torres et al., 2002], whereas pore water advection occurs at 0.5–1m/yr, calculated from dissolved calcium profiles in sediment pore water, or 0.3–1m/yr, calculated from sea floor methane seepage rates [Torres et al., 2002], so free gas exits conduits more than 10^7 times faster than the speed of fluid advection in the sediments. At less active regions, like Blake Ridge, advective fluxes are two to three orders of magnitude slower than those at Hydrate Ridge [Nimblett and Ruppel, 2003].

The results from this work also have important implications for carbon dioxide storage in the deep sub-seafloor, where sequestration is possible by hydrate formation [Koide et al., 1995, 1997b] and gravitational trapping [Koide et al., 1997a; House et al., 2006; Levine et al., 2007; Goldberg et al., 2008]. Whether the migration of supercritical CO_2 is dominated by capillary invasion or fracture opening may determine the viability of this sequestration concept in ocean sediments. In these systems, fractures will have a tendency to propagate vertically [Nunn and Meulbroek, 2002; Boudreau et al., 2005], which could provide fast pathways for the escape of injected CO_2 by pressure gradients. In order to avoid the fracturing regime, it is conceivable that one should inject in coarse-grained, high-energy sediments such as turbidites.

Appendix A. Throat Conductance

In this section we derive Equation (9) for the throat conductance. Our formulation resolves one fundamental problem of two-dimensional grain-scale models: the fact that when grains are in contact, the aperture of the throat between pores is zero. Three-dimensional models do not suffer from this problem, because the throat can be associated with the section of minimum cross-sectional area between two pore bodies.

Before discussing our formulation for 2D models, consider an individual pore throat in 3D, as shown in Figure 86. A throat can be considered a microfluidics pipe, with a certain angular cross section. For creeping flow in a small channel, the Navier–Stokes equations reduce to the elliptic Poisson equation. For a coordinate system in which one of the axes (say, the z-axis) is parallel to the channel, the equation and boundary conditions describing the flow read [Bird et al., 1960]:

$$\nabla^2 v = -\frac{\Xi}{\mu} \quad \text{in } \Omega, \tag{30}$$

$$\Xi = -\frac{\partial p}{\partial z}, \tag{31}$$

$$v(x,y) = 0 \quad \text{on } \partial\Omega, \tag{32}$$

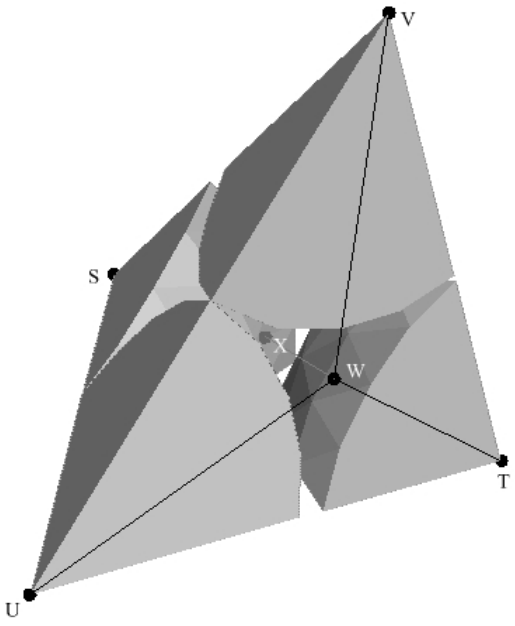

Figure 86: Representation of a pore throat in a three-dimensional grain-scale model [Prodanovic and Bryant, 2006]. The throat is the section with minimum cross-sectional area between two pore bodies. This area is positive even when the surrounding grains are in contact, or even if they overlap.

where μ is the fluid viscosity, Ξ is the (negative) pressure gradient, and $\partial\Omega$ is the boundary of the two-dimensional cross section Ω.

Many solutions to this equation exist for simplified geometries, and useful parameterizations have been developed in the context of pore-network models of fluid-flow through rocks [Øren et al., 1998; Patzek and Silin, 2001]. The total flowrate q through the throat cross section can be expressed in the following form:

$$q \equiv \int_{\Omega} v(x,y)\, \mathrm{d}\Omega = C\Xi, \tag{33}$$

where C is the throat conductance. Dimensional analysis dictates that the conductance can, in turn, be expressed as follows:

$$C = \frac{1}{\mu} A^2 \tilde{C}, \tag{34}$$

where A is the cross-sectional area of the throat, and $\tilde{C}$ is a dimensionless conductance. It has been shown that, for a very wide range of throat shapes, the dimensionless conductance is simply a function of the shape factor,

$$G = \frac{A}{P^2}, \tag{35}$$

where P is the perimeter of the throat. In fact, for triangular cross sections, the dimensionless conductance can be approximated by the simple expression [Patzek and Silin, 2001]:

$$\tilde{C} = \frac{3}{5} G. \tag{36}$$

With precise knowledge of the geometry of the grain assembly, one could compute the area and shape factor for each throat, and evaluate the throat conductance using the expressions above. However, since these equations themselves rely on the assumption of creeping flow in cylindrical channels, it is sufficient to consider a "master" geometry (like the one shown in Figure 86). In any case, it is important to note that the throat conductance scales with the fourth power of the grain size:

$$C \sim \frac{\tilde{C}}{\mu} r_g^4. \tag{37}$$

The question is: how do we apply this conductance formulation to *two-dimensional* grain-scale models? In 2D models, the cross section (or aperture) of a pore throat is zero if grains are in contact. This would lead to a model that does not conduct fluid. To address this issue, previous investigations typically resort to defining an artificial throat aperture using heuristic arguments [Bruno and Nelson, 1991; Li and Holt, 2001, 2004; ITASCA, 2004].

We resolve this problem by understanding a two-dimensional model as a collapsed three-dimensional model. We must make some approximations with respect to the grain arrangement in the third dimension. In particular, we assume cubic packing of the 3D assembly. Consider two grains of the same size that are in contact in the 2D model. For cubic packing in the third dimension, the geometry of the throats is well defined, and the flow rate through an individual throat can be computed with Equations (33)–(34).

Importantly, this model leads to physically-realistic throat geometries (and, therefore, throat conductances) regardless of whether the two grains defining a throat are just in contact (gap $d = 0$), whether there is a gap between them ($d > 0$), or whether there is overlap between them ($d < 0$). For each configuration, the shape factor can be computed using elementary geometry, and the dimensionless conductance evaluated therefrom. In Figure 87, we summarize the throat conductance formulation for 2D grain assemblies.

In a 2D model, we must collapse the third dimension, and compute the flow rate between pore bodies as

$$q_{2D} = q_{3D} \frac{w}{2r_g}, \tag{38}$$

where, if $w = 1$, Q is the flowrate per unit width. Combining Equation (38) with (33) and (34) leads to Equations (8) and (9), as desired.

Appendix B. Capillary Entry Pressure

The conceptual model presented above also provides a framework for determining capillary entry pressures in two-dimensional models, which is required to simulate two-phase flow.

Consider, first, invasion of gas through a throat in a three-dimensional setting (Figure 86). The surface tension between gas and brine is γ, and the contact angle between the gas–water interface and the solid surface is θ. Gas will penetrate through the throat cross section when the capillary pressure (the gas pressure minus the water pressure) exceeds the threshold capillary pressure. The Mayer–Stowe–Princen (MSP) [Mayer and Stowe, 1965; Princen, 1969a,b, 1970] method for calculating the threshold pressure relies on equating the curvature of the corner arc menisci to the curvature of the invading interface. Expressions for the drainage capillary entry pressure have been derived for a variety of cross sections [Mason and Morrow, 1991; Øren et al.,

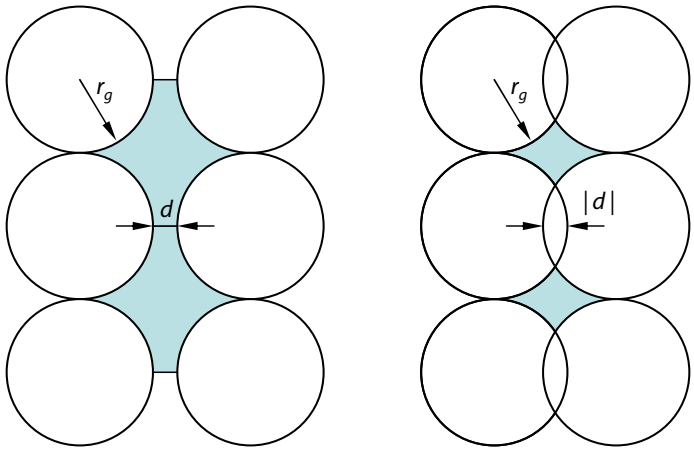

If $d > 0$ (gap)

$$A = 4r_g^2 \left(1 - \frac{\pi}{4} + \frac{d}{r_g}\right)$$

$$P = 2r_g \left(\pi + \frac{2d}{r_g}\right)$$

Elseif $d \leq 0$ (overlap)

$$A = 4r_g^2 \left(1 - \sqrt{\frac{|d|}{r_g} - \left(\frac{|d|}{2r_g}\right)^2}\right) \left(1 - \frac{|d|}{r_g}\right)$$

$$\alpha = \sin^{-1}\left(1 - \frac{|d|}{2r_g}\right)$$

$$P = 2r_g \cdot 2\alpha$$

Endif

$$G = \frac{A}{P^2}$$

$$\tilde{C} = \frac{3}{5}G$$

Figure 87: Summary of the throat conductance formulation for 2D grain assemblies. The figure shows the top view of the cross-sectional area of the throat in the collapsed 3D model. (See text for the definition of the variables and a discussion of the formulation.)

1998; Patzek, 2001]. They take the form:

$$P_c^e = \frac{2\gamma}{r_{\rm th}} F(\theta, G, D), \tag{39}$$

where $r_{\rm th}$ is the radius of the inscribed circle, and F is a function of the receding contact angle and the geometry of the throat—through the throat shape factor G and a function D of the throat corner angles. It turns out that, if the contact angle is small (as it normally is for gas invasion into a natural sediment), $F \approx 1$ [Lenormand et al., 1983; Patzek, 2001]. Therefore, for zero contact angle, the capillary entry pressure can be approximated by

$$P_c^e = \frac{2\gamma}{r_{\rm th}}. \tag{40}$$

For a throat formed in the space between three spherical grains of equal radius r_g that are in contact, elementary geometry leads to the expression:

$$r_{\rm th} = r_g \left(\frac{2}{\sqrt{3}} - 1 \right), \tag{41}$$

and, therefore, we obtain the simple and useful estimate:

$$P_c^e \approx 10 \frac{\gamma}{r_g}. \tag{42}$$

Once again, we apply this concept to two-dimensional grain-scale models, by assuming simple cubic packing in the third dimension. In this way, we can rigorously define a throat radius (and, from it, a capillary entry pressure) even when the 2D throat aperture is zero (because the 2D grains defining a pore throat are in contact). If the two grains are exactly in contact (see Figure 88), one can immediately obtain the relation:

$$r_{\rm th} = r_g(\sqrt{2} - 1). \tag{43}$$

When the two grains of equal size are separated by a gap ($d > 0$), or when they overlap ($d < 0$), the relation above can be extended as follows:

$$r_{\rm th} = r_g \left(\sqrt{1 + \left(1 + \frac{d}{2r_g} \right)^2} - 1 \right). \tag{44}$$

Substituting Equation (44) into (40) leads to Equation (15), as desired.

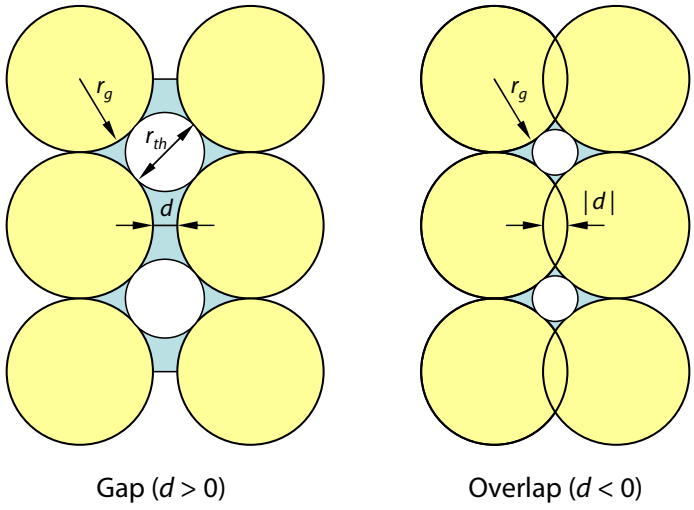

Figure 88: Geometry of the pore throat in the third dimension of a 2D grain-scale model, for the definition of the throat radius r_{th}.

Crossover from fingering to fracturing in deformable disordered media

The displacement of one fluid by another in disordered media—such as porous media, etched micromodels, nanopatterned surfaces, or biological tissues—gives rise to complex invasion patterns [Gollub and Langer, 1999]. The classical phase diagram of fluid–fluid displacement delineates three different regimes [Lenormand et al., 1988]: compact displacement, capillary fingering or invasion percolation [Wilkinson and Willemsen, 1983], and viscous fingering [Paterson, 1984; Måløy et al., 1985; Stokes et al., 1986]. This classification, which is based on micromodel experiments and modified invasion percolation models, is applicable to drainage in rigid media under negligible gravity effects. Much attention has been devoted to the characterization of each regime, as well as the transition among the different regimes [Chen and Wilkinson, 1985; Yortsos et al., 1997; Ferer et al., 2004; Toussaint et al., 2005]. It has been shown, for instance, that pore-scale disorder in rigid media impacts the regime transition from invasion-percolation to viscous fingering [Chen and Wilkinson, 1985; Toussaint et al., 2005].

Coupled fluid and granular flow also leads to a variety of patterns, including fractures [Chevalier et al., 2009], viscous fingers [Cheng et al., 2008], desiccation cracks [Meakin, 1991] and labyrinth structures [Sandnes et al., 2007]. The formation of these patterns typically involves large particle rearrangements. Interestingly, a transition from viscous fingering to fracturing has been observed for fluid displacement in viscoelastic fluids and colloidal suspensions [Lemaire et al., 1991; Lindner et al., 2000]. This crossover depends on the system deformability and on the Deborah number—a ratio of the characteristic times of a flow event and viscoelastic relaxation [Lemaire et al., 1991].

The fracturing process in a disordered medium has been studied at length [Meakin, 1991]. Block–spring network models that simulate fracture growth have emphasized the role of heterogeneity in the mechanical properties (elasticity or strength of the springs), using either annealed disorder [Meakin et al., 1989; Levermann and Procaccia, 2002] or quenched disorder [Tzschichholz and Herrmann, 1995; t. Leung and Néda, 2000]. However, the transition from fluid instability (capillary or viscous fingering) to fracturing remains poorly characterized at the pore scale. Recent modeling results suggest that the mode of gas invasion in a porous medium shifts from capillary invasion to fracture opening as the grain size decreases [Jain and Juanes, 2009], in agreement with observations of gas bubble growth in sediments [Boudreau et al., 2005], and drying in three-dimensional granular media [Xu et al., 2008].

In this paper, we investigate the crossover from fingering to fracturing patterns in deformable, disordered media, by means of a pore-scale model of the displacement of one fluid by another. Our pore-scale model captures the dynamics of pressure redistribution at the invading front, allowing us to characterize the effect of the initial disorder in hydraulic properties on the transition from capillary to viscous fingering. The model incorporates the two-way coupling between fluid displacement and mechanical deformation, providing the mechanisms for pore opening in response to pressure loading (direct coupling), and alteration of the flow properties by particle rearrangements (reverse coupling). Despite its simplicity, the model predicts the emergence of fracture opening as a dominant feature of the invasion pattern for sufficiently deformable systems.

We develop a 2-D discrete model of a random medium. Since we are interested in elucidating the general mechanisms of fluid invasion, rather than performing predictions for a particular type of

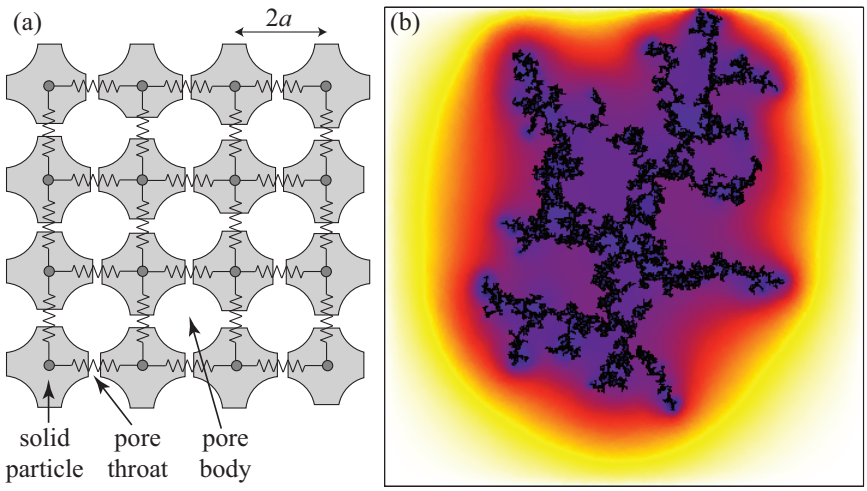

Figure 89: (a) Schematic of the model and simulation of drainage. The solid matrix is represented by a square lattice of dented blocks, connected mechanically by springs. The narrow openings between particles are the pore throats, which connect the larger openings (pore bodies). (b) An inviscid, nonwetting fluid is injected at the center of the network, displacing a viscous, wetting fluid. The pressure "halo" that surrounds the ramified invaded region reflects the finite timescale required for pressure dissipation in the defending fluid. The color scheme represents the log of pressure normalized by the invading fluid pressure. In all our simulations, we use networks of 400×400 pores ($L = 400a$), and set $a = 0.1$ μm, $\mu = 10^{-3}$ Pa $\cdot$ s, $\gamma = 0.07$ N m^{-1}, and $\epsilon_0 = 0.05$. Here, Ca $= 9 \times 10^{-4}$ and $\lambda = 0.3$.

medium, we assume a simple square-lattice arrangement of dented blocks [Fig. 89(a)]. Variation in particle shapes leads to disorder in throat apertures, which is assumed to be uncorrelated in space. Mechanical interaction among the particles is represented through a block-and-spring model. The springs are assumed to be uniformly pre-stressed under compression. Such confinement prevents large microstructural rearrangements.

We construct two interacting networks: a solid network and a fluid network, whose nodes are the solid particles and the pore bodies, respectively. We solve for particle displacements and fluid pressures at the pore bodies. The characteristic length scale is the pore size a, which here we take as half the distance between nodes in the lattice. We model pore-scale disorder by assigning different initial area A and permeability k to the throats between pore bodies. Both the throat area and permeability scale with the square of the throat aperture r, that is, $A \sim r^2$, $k \sim r^2$. We characterize the disorder in throat aperture by drawing values from a uniform distribution, $r \in [1-\lambda, 1+\lambda]\bar{r}$, where $\bar{r} \sim a$. The coefficient $\lambda \in (0,1)$ is a measure of the degree of disorder [Chen and Wilkinson, 1985].

We simulate the invasion of an inviscid, nonwetting fluid into a medium initially saturated with a wetting fluid of dynamic viscosity μ. The inviscid fluid pressure is spatially uniform. A fluid-fluid interface will advance from one pore to another if the capillary pressure (the difference between nonwetting and wetting phase pressures) exceeds the capillary entry pressure $2\gamma/r$, where γ is the interfacial tension between the fluids and r is the aperture of the connecting throat [de Gennes, 1985]. If both fluids are inviscid, pressure variations in response to interface movement dissipate instantaneously; then, the process is described by the classical invasion–percolation algorithm [Wilkinson and Willemsen, 1983], and depends exclusively on the quenched disorder.

Consideration of fluid viscosity introduces spatial non-locality due to redistribution of the defending fluid along the invasion front. Slow drainage in disordered media occurs in the form of bursts, which lead to sudden changes in the defending fluid pressure ("Haines jumps" [Haines, 1930]). When one or more pores are drained during a burst, the interface menisci at neighboring pores readjust, receding along throats or even leading to a backfilling of previously drained pores [Xu et al., 2008]. The short timescales associated with pressure buildup in the defending fluid relative to that of drainage out of the system makes fluid redistribution along the front a crucial mechanism [Måløy et al., 1992; Furuberg et al., 1996; Xu et al., 2008]. This mechanism reduces the capillary pressure (the local curvature decreases as the meniscus recedes) and suppresses further invasion until the excess pressure in the defending fluid is dissipated, thus limiting the burst size.

Incorporating meniscus readjustments in a dynamic pore-network model [Aker et al., 1998; Lam, 2004] is computationally intensive. Here, we introduce the main effect of front interface dynamics: an effective compressibility of the system, even though the defending fluid is nearly incompressible.

The effective compressibility c_t can be obtained by the following argument. The capillary number is a ratio of viscous forces over capillary forces at the pore scale, $\mathrm{Ca} = \Delta p_{\mathrm{visc}}/\Delta p_{\mathrm{cap}}$. Assuming Poiseuille flow, the viscous pressure drop over a pore length is $\Delta p_{\mathrm{visc}} \sim \mu v a/k$, with $k \sim a^2$, and v the average flow velocity evaluated from the cumulative values of the drained volume, time, and cross-sectional area along the boundaries [Furuberg et al., 1996]. Together with the Young–Laplace equation, $\Delta p_{\mathrm{cap}} \sim \gamma/a$, this leads to the classical definition $\mathrm{Ca} = \mu v/\gamma$. An alternative definition is the ratio of time scales for pressure dissipation and pore filling [Furuberg et al., 1996], $\mathrm{Ca}^* = \Delta t_{\mathrm{press}}/\Delta t_{\mathrm{fill}}$. Unlike [Furuberg et al., 1996], here we invoke pore-scale quantities only.

The time scale for pressure dissipation is $\Delta t_{\text{press}} \sim a^2/D$, where $D = (k/\mu)/c_t$ is the hydraulic diffusivity. The pore filling time scale is simply $\Delta t_{\text{fill}} \sim a/v$, leading to $\text{Ca}^* = (\mu v/\gamma)(c_t\gamma/a)$. Equating the two definitions of the capillary number provides the effective compressibility of slow drainage in a disordered medium:

$$c_t = \frac{a}{\gamma}. \tag{45}$$

In our simulations, the nonwetting fluid is injected at the center of the lattice at an approximately constant volumetric injection rate. Since the invading fluid is inviscid, we focus on the pressure evolution in the defending fluid. From mass conservation at a pore body, we write the equation of pressure evolution at an undrained pore, $p(t + \Delta t) = p(t) + \sum_j q_j \Delta t/(c_t V)$, where Δt is the time step, V is the pore volume, and the summation is over all neighboring pores. The volumetric flow rate between the pore and its neighbor j is given by Darcy's law $q_j = (Ak/\mu)(p_j - p)/\ell_j$, where ℓ_j is the length over which the pressure drop $p_j - p$ is applied. For flow between two undrained pores, $\ell = 2a$. If pore j is drained, the meniscus between the two pores starts advancing if $p_j - p > 2\gamma/r$. The consequent pressure variations in the undrained pore are governed by the ability of the medium to dissipate pressure through the effective compressibility. The length over which viscous pressure drop takes place decreases as the meniscus advances, according to the expression $\ell_j(t + \Delta t) = \ell_j(t) - (q_j/A)\Delta t$.

A typical invasion pattern from our model for conditions near the transition between capillary fingering and viscous fingering is shown in Fig. 89(b). The simulation clearly shows the presence of a pressure "halo" surrounding the invaded region, as a result of the non-negligible time required to dissipate pressure in the viscous defending fluid.

We are interested in the effect of heterogeneity on the flow pattern. The advancement of the interface is determined by the competition among different pores along the front, which depends on the distribution of throat apertures and pore pressures. We expect the transition from capillary to viscous fingering to occur when the characteristic macroscopic viscous pressure drop "perpendicular" to the interface, $\delta p_\perp$, exceeds the variation in capillary entry pressures along the front, $\delta p_\parallel$. We express $\delta p_\perp \sim \nabla p_\perp L$, where L is the macroscopic length scale, and use Darcy's law, $\nabla p_\perp \sim \mu v/k$, to obtain $\delta p_\perp \sim \mu v L/a^2$. We use a fixed value of the macroscopic length scale with $L \gg a$ for the viscous pressure drop in the defending phase, an assumption that is justified during the initial stages of the invasion but that becomes questionable at later stages, when the invasion front approaches the system's boundaries and becomes fractal [Lenormand, 1989]. The maximum capillary pressure difference along the front is $\delta p_\parallel = \gamma/r_{\min} - \gamma/r_{\max} \sim [\lambda/(1-\lambda^2)]\gamma/a$. Equating $\delta p_\perp \sim \delta p_\parallel$, and using the definition of the capillary number, $\text{Ca} = \mu v/\gamma$, we predict a transition from viscous fingering to capillary fingering with the scaling $\text{Ca} \sim [\lambda/(1 - \lambda^2)]a/L$.

We synthesize our results on a phase diagram in Ca–λ space (Fig. 90). The invasion patterns are classified by visual appearance, as well as by the fractal dimension D_f (see Appendix). The value of D_f by itself is insufficient to provide unequivocal classificiation due to expected fluctuations for finite samples. The simulations confirm our predictions on the transition from capillary to viscous fingering. For $\text{Ca}/\lambda \gg a/L$ the effect of heterogeneity is negligible relative to that of Laplacian-driven growth [Niemeyer et al., 1984], allowing the most advanced fingers to continue propagating. This results in long and thin fingers typical of viscous fingering. For $\text{Ca}/\lambda \ll a/L$, the heterogeneity in throat apertures dominates, leading to invasion that propagates at alternating locations. As a result, different parts of the front will coalesce and trap some of the defending fluid

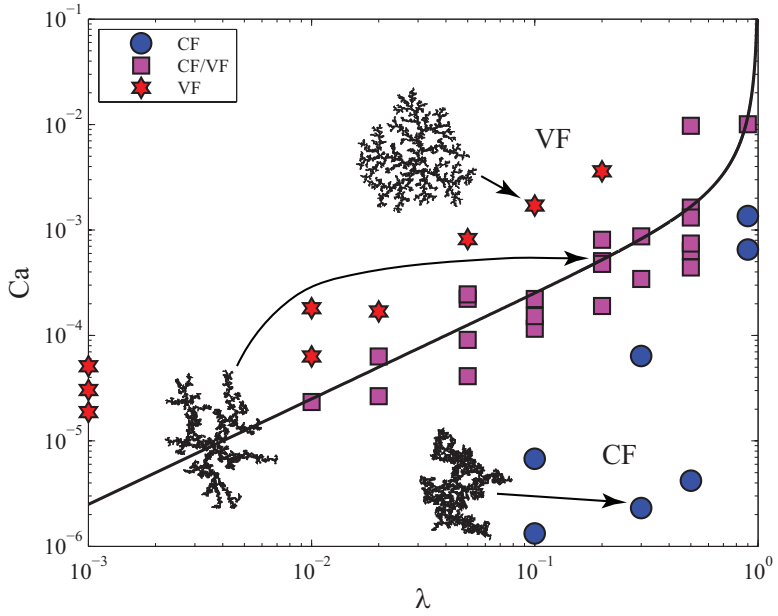

Figure 90: Phase diagram of the invasion pattern as a function of capillary number Ca and the pore-scale disorder λ, in a rigid solid matrix. The classification is based on visual appearance (see insets), as well as the mass fractal dimension D_f. Box counting [Niemeyer et al., 1984] provides estimates of $D_f \approx 1.82$ and $D_f \approx 1.64$ for capillary fingering (CF) and viscous fingering (VF), respectively, with standard deviation $\sigma_{D_f} = 0.08$ (see Appendix). The transition from capillary to viscous fingering (CF/VF) occurs at Ca $\approx [\lambda/(1-\lambda^2)]a/L$ (black solid line), reflecting a balance between viscosity and pore-scale disorder in capillary entry pressures.

behind, creating the fat clusters with thick fingers characteristic of capillary fingering.

The two regimes are separated by an intermediate regime centered around the theoretical curve Ca $\sim [\lambda/(1-\lambda^2)]a/L$. In the limit $\lambda \to 1$ the capillary disorder blows up. The analysis above indeed suggests that the capillary fingering regime always dominates in this limit (the crossover curve diverges in Ca–λ space). In the limit of nearly homogeneous media and high capillary number (not shown in Fig. 90), the model's anisotropy becomes dominant and dendritic growth occurs along the lattice axes, similar to the experimental results in [Chen and Wilkinson, 1985]. Our analysis suggests the existence of a crossover length scale $L_\times \sim [\lambda/(1-\lambda^2)]\text{Ca}^{-1}a$, at which the displacement experiences a regime shift from capillary fingering (below $L_\times$) to viscous fingering (above $L_\times$). A similar conclusion was drawn from the mass fractal dimension of the pattern in drainage experiments [Toussaint et al., 2005].

A compliant solid matrix can deform in drainage, which in turn may lead to fracture opening during fluid invasion. Here, we investigate the impact of system deformability on the emergence of invasion patterns. Particle displacements cause changes in the contraction of the springs over time, $h(t)$. To highlight the effect of disorder in flow properties, we assume the system is initially pre-stressed homogeneously, such that all springs are subject to the same compression, h_0, corresponding to a macroscopic strain $\epsilon_0 = h_0/2a$. Each particle is subject to two types of forces: pressure forces and contact forces. The force exerted on a particle by the fluid occupying an adjacent pore body is oriented at 45° and is of magnitude $f_p = pA_p$, where $A_p \sim a^2$ represents the area upon which the pressure acts. The interparticle contact forces f_c are updated by $f_c(t+\Delta t) = f_c(t) + K\Delta h$, where K is the spring stiffness and $\Delta h = h(t+\Delta t) - h(t)$ is the change in spring contraction. Particle positions are determined at the new time step by imposing force balance at every block, $\sum(\vec{f_p} + \vec{f_c}) = \vec{0}$, which leads to a linear system of equations to be solved for Δh of every spring. Particle displacements impact fluid flow because they modify the throat apertures. We evaluate changes in throat apertures and in interparticle forces from the particle displacements in analogy with cubic packing of particles with frictionless, Hertzian contacts, such that $\Delta r = -\Delta h(1-\epsilon)/[2\sqrt{1+(1-\epsilon)^2}]$, where $\epsilon = h(t)/2a$, and the spring stiffness $K = 2E^*\sqrt{R^*h}$, where $R^* = a/2$, and E^* is the constrained Young modulus of the particle material [Johnson, 1987]. We simulate material behavior that cannot sustain tension and, therefore, a spring is removed when there is net elongation between blocks ($h \leq 0$). A small cohesive force is applied as a regularization parameter. This force is orders of magnitude smaller than the typical pressure force, and we have confirmed that the results are insensitive to the value of this cohesive force, as long as it is small.

Our model predicts fracturing patterns that are strikingly similar to those observed in 2-D experiments, with thin, long features which are straight over a length larger than a pore size [Chevalier et al., 2009], and fractal dimension lower than in fingering, $D_f \approx 1.43$ (see Appendix). The straight segments of the invasion pattern form as a result of localized rearrangements: increasing throat aperture by displacing particles in a direction perpendicular to that of the finger advancement promotes finger growth in that direction. This mechanism is arrested when the front reaches a bottleneck, associated with either initial disorder or compaction ahead of another propagating fracture.

Emergence of a fracturing pattern requires sufficiently large change in throat apertures. Particle rearrangements depend on the balance between the forces applied by the fluids and the interparticle forces holding the particles in place. We define a dimensionless "fracturing number" N_f as the ratio

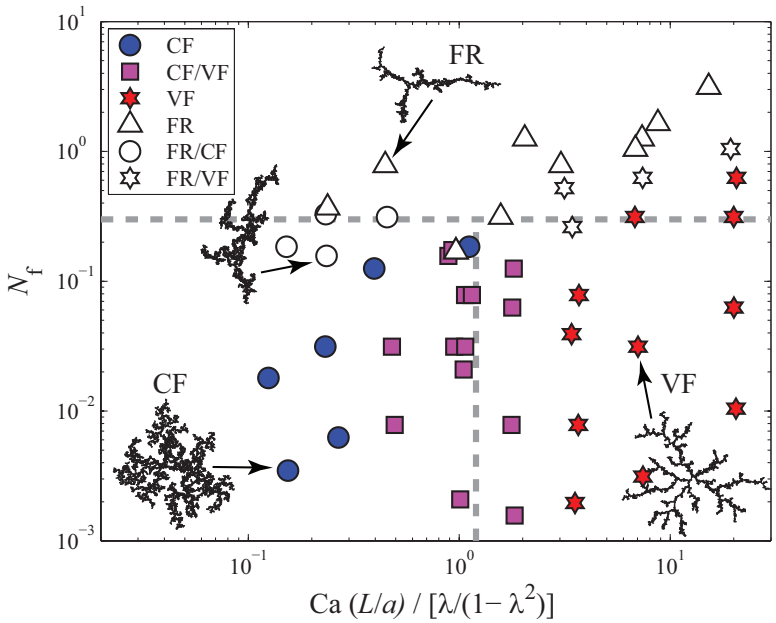

Figure 91: Phase diagram of drainage in deformable, disordered media, showing three distinct invasion patterns: viscous fingering (VF), capillary fingering (CF), and fracturing (FR). The gray dashed lines denote transitions among the different regimes. Intermediate regimes are marked by CF/VF, FR/VF and FR/CF. The deformability of the system is characterized by the "fracturing number" N_f: drainage is dominated by fracturing in systems with $N_\mathrm{f} \gg 1$. At lower N_f values, a transition between capillary and viscous fingering occurs around $\mathrm{Ca}(L/a)/[\lambda/(1-\lambda^2)] \approx 1$.

of the typical pressure force increment after drainage of a pore, $\Delta f_p \sim \gamma a$, and the force increment resulting from deformation, $\Delta f_c \sim \lambda E^* a^2 \epsilon_0^{1/2}$. The latter is obtained from the condition $\Delta h \sim \Delta r$, where the required change in throat aperture is $\Delta r \sim \lambda \bar{r} \sim \lambda a$, and using the initial overlap h_0 to compute the interparticle stiffness K. With that,

$$N_\mathrm{f} = \frac{\gamma}{\lambda a E^* \epsilon_0^{1/2}}. \tag{46}$$

An alternative expression for N_f is obtained by substituting the initial confining stress $\sigma_0 \sim E^* \epsilon_0^{3/2}$ into Eq. (46).

We synthesize drainage behavior in a deformable medium in a phase diagram with two dimensionless groups, the fracturing number N_f and a modified capillary number $\mathrm{Ca}(L/a)/[\lambda/(1-\lambda^2)]$—see Fig. 91. For a rigid medium ($N_\mathrm{f} \ll 1$), the transition from capillary to viscous fingering occurs at $\mathrm{Ca}(L/a)/[\lambda/(1-\lambda^2)] \approx 1$. Fracturing is evident when $N_\mathrm{f} \gg 1$. A crossover from fingering to fracturing occurs at $N_\mathrm{f} \approx 1$. Equation (46) implies that fractures tend to open in fine-particle media, suggesting that below a critical particle size—which decreases with the particle stiffness and the external confinement—invasion is dominated by fracturing. This is consistent with observations of gas bubble growth in sediments [Boudreau et al., 2005; Jain and Juanes, 2009] and drying in porous media [Xu et al., 2008].

In conclusion, this study explains the crossover among the different fluid displacement patterns of drainage in a deformable medium. The invasion behavior depends on two dimensionless groups.

One is related to the influence of pore-scale disorder on the balance between viscous forces and capillary forces. The other measures the deformability of the medium as a function of capillary effects, material properties and initial confinement. Despite its simplicity, our model predicts the transition from capillary fingering to viscous fingering in rigid media, and a crossover from fingering to fracturing in deformable media, suggesting that it captures the essential aspects of the interplay between multiphase fluid flow and mechanical deformation.

Appendix

In this appendix we demonstrate the ability of our pore-scale model to capture the transition among the different invasion regimes—viscous fingering (VF), capillary fingering (CF) and fracturing (FR). Our classification of the displacement pattern is based on visual appearance, as well as the fractal dimension D_f (using box counting [Niemeyer et al., 1984]). Visual appearance is an essential consideration in the classification because the estimation of the fractal dimension from the mass vs. distance curves is subject to large fluctuations for finite-size systems [Måløy et al., 1985; Blunt and King, 1990; Løvoll et al., 2004; Praud and Swinney, 2005].

First, we illustrate the transition between VF and CF. For a given value of the disorder parameter, $\lambda = 0.1$, we investigate the displacement pattern for a range of capillary numbers. For each value of Ca, we show the displacement pattern, and the curve of mass vs. distance from which the fractal dimension is obtained (Fig. 92). It is evident that the model predicts a transition from VF (high Ca) to CF (low Ca). Moreover, the values of the fractal dimension are in excellent agreement with experimentally-determined values of 1.60–1.65 for VF in a *porous* Hele-Shaw cell [Måløy et al., 1985; Løvoll et al., 2004] to the well known value of 1.82 for invasion–percolation corresponding to CF.

Next, we show the transition between VF and FR, by studying displacements with a similar value of the modified capillary number, $\mathrm{Ca}^* = \mathrm{Ca}(L/a)/[\lambda/(1-\lambda^2)] \approx 10$ and a range of values of the key dimensionless group, the fracturing number N_f. The fracturing pattern is characterized by fingers with straight segments and a lower fractal dimension (Fig. 93).

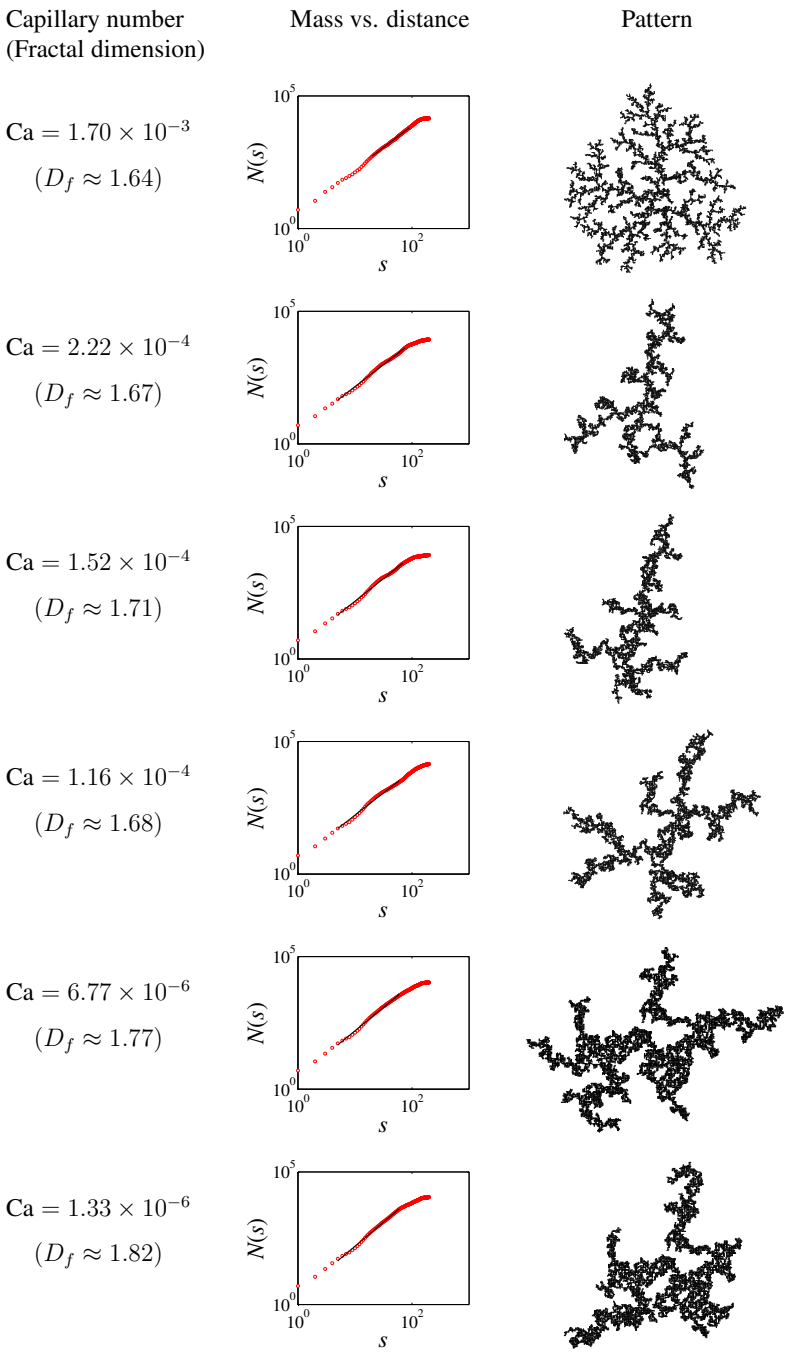

Figure 92: Fractal dimension and displacement pattern for rigid medium, with a value of $\lambda = 0.1$, showing a transition from viscous fingering to capillary fingering as the capillary number is reduced.

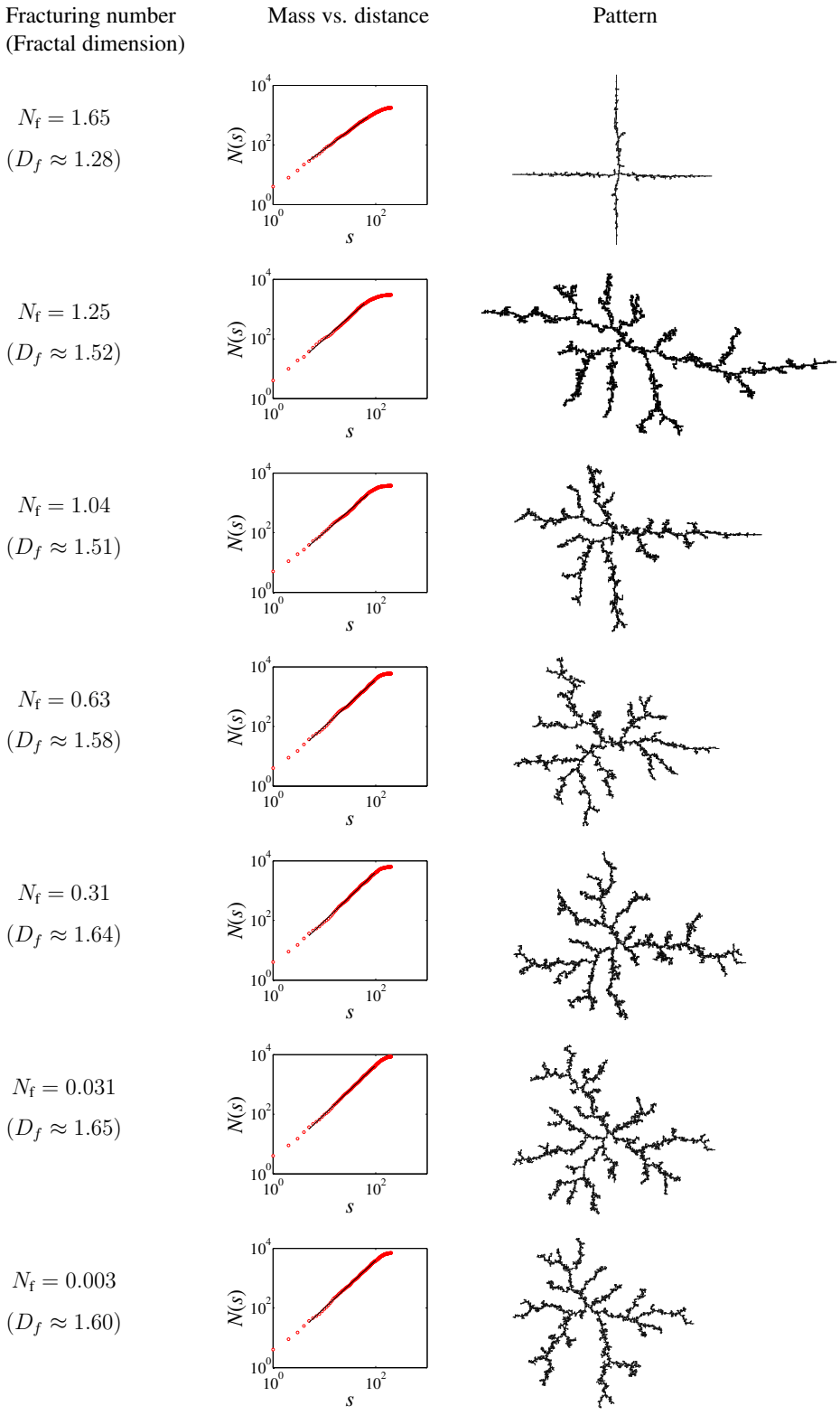

Figure 93: Fractal dimension and displacement pattern for deformable medium, with a value of $\mathrm{Ca}^* \approx 10$, showing a transition from fracturing to fingering as the fracturing number is reduced.

Thermodynamic and hydrodynamic constraints on overpressure caused by hydrate dissociation: A porescale model

Introduction

Methane hydrate is a solid compound that forms by crystallization of water and methane upon cooling and/or pressurization. Accumulations of methane hydrate in hydrate-bearing sediments (HBS) have gained much attention for their potential as an energy resource [Boswell, 2009] and their role as a greenhouse gas in future global warming [Archer et al., 2009]. Heating or depressurization cause hydrate to dissociate into free gas and water. Dissociation of hydrate within the pore space of sediments has often been invoked as a mechanism that may lead to significant overpressures (up to tens of MPa), in view of the multiple-fold volume increase that occurs upon dissociation [Xu and Germanovich, 2006; Kwon et al., 2006; Rutqvist and Moridis, 2009]. Overpressure induced by dissociation has been suggested as a trigger for sediment failure, including submarine landslides [Sultan et al., 2004; Mienert et al., 2005; Xu and Germanovich, 2006], soft-sediment deformation [Kennett and Fackler-Adams, 2000], pingo-like features [Paull et al., 2007], mud volcanoes [Van Rensbergen et al., 2002] and wellbore damage [Rutqvist and Moridis, 2009]. Warming of ocean waters and consequent dissociation of extensive HBS layers, leading to sediment failure and massive release of methane gas, has been proposed as the cause of the Paleocene-Eocene Thermal Maximum [Dickens et al., 1995], and as a potential key player in the current carbon cycle [Dickens, 2003; Westbrook et al., 2009].

The possible implications of dissociation raise the need for understanding the relevant mechanisms, in particular the interplay between dissociation and pressure evolution. Existing models predict large overpressures in fine-grained sediments, where the low permeability would prevent rapid pressure dissipation [Xu and Germanovich, 2006; Kwon et al., 2006; Rutqvist and Moridis, 2009; Kwon et al., 2010]. Xu and Germanovich [2006] evaluate overpressures as high as 50 MPa for undrained (no-flow) conditions and 7 MPa for low permeability sediment, assuming a constant dissociation rate which is independent of the pore pressure. The end-member scenario of no flow and restricted volumetric expansion was investigated by Kwon et al. [2006], who correctly point out that since rising pressure stalls further dissociation, additional heat is required to continue the dissociation process. This self-preservation mechanism leads to pressure-temperature (p-T) conditions which follow the three-phase (hydrate-gas-brine) equilibrium curve during dissociation. Therefore, a large overpressure (hereafter defined as the gas pressure above the initial water pressure p_0 prior to dissociation) implies a large temperature increase; for example, an increase of $\sim$9 MPa is accompanied by a temperature rise of over 9°C. A pressure increase of tens of MPa requires heating by tens of degrees. Simulating long-term thermal stimulation by a hot wellbore (90°C), Rutqvist and Moridis [2009] predict overpressures of $\sim$15 MPa in nearby sediments. Smaller pressures (less than 3 MPa) were predicted by Kwon et al. [2010] in simulating dissociation due to a wellbore ($\sim$20°C warmer than its surrounding) in a low-permeability clay. While the authors honor self-preservation by constraining the pressure by the equilibrium pressure, they do not account for dissociation kinetics, and assume that hydrate saturation is sufficiently low to neglect gas flow. However, we will show that gas flow and percolation can occur at hydrate saturations as low as 5%, in agreement with Tsimpanogiannis and Lichtner [2006].

A crucial mechanism which is missing from the models cited above is the coupling among

dissociation kinetics, flow of gas and water, and sediment deformation, including the formation of preferential flow paths and fractures. Consideration of this mechanism requires description of the pore-scale physics. Tsimpanogiannis and Lichtner [2006] investigated the flow patterns of methane gas produced by heating an HBS, and showed that larger pore apertures and a broader range of aperture sizes allow larger gas quantities to percolate through a sample, hence increasing the gas productivity. The authors used a pore-network model based on invasion percolation, assuming instantaneous dissociation and fixed network properties (no geomechanical effects).

In this paper we study the pressure evolution during thermally-induced dissociation. We present a mechanistic, pore-scale model that couples dissociation kinetics, multiphase flow and sediment mechanics. We explore the range of behaviors between the two end-members: (a) no-flow (undrained) conditions; and (b) instantaneous pressure dissipation (fully drained). We model the physics at the pore scale and thus perform all computations at the pore level. The collective dynamics give rise to global effects such as pressurization of the entire sample and gas-invasion patterns. While upscaling the results from our simulations with millimeter-size samples to the reservoir scale is not straightforward, our model elucidates fundamental mechanisms that control the sediment behavior at the pore scale. We demonstrate that rapid pressure buildup is not possible because of the negative feedback between dissociation rate and fluid pressure. The strict upper bound for the gas pressure is its thermodynamic limit: the equilibrium pressure. However, for typical values of the kinetic rates and medium permeability, our results show that pressure build-up by dissociation is slow compared with pressure dissipation by drainage. As a result, overpressures are controlled by the value of the gas pressure required to invade into the porous medium, and are typically much lower than the equilibrium pressure.

Model Formulation

We simulate a low-permeability sample saturated with water and dispersed hydrate crystals, subjected to a sudden temperature increase which brings hydrate out of thermodynamic equilibrium. The small inhibiting effect of the latent heat on the dissociation rate allows us to consider isothermal dissociation under fixed, uniform temperature and exclude heat transfer effects. We evaluate the temporal and spatial evolution of the mass, volume and pressure of hydrate, water and gas, and their impact on the sediment's mechanical and flow properties. At each time step we compute: (1) the dissociated hydrate mass for every crystal, given the surrounding fluid pressures; (2) pore pressure variations caused by the conversion of hydrate into water and gas; (3) flow of gas and water induced by the rising pore pressure; and (4) changes in hydraulic properties by deformation of the solid matrix (microstructural rearrangements).

We emphasize in our model the role of multiphase flow by assuming that the driving force for the flow is the generation of pressurized gas by hydrate dissociation. Once gas pressure overcomes the local capillary thresholds, gas expands by invading into nearby water-filled pores. We evaluate the pressure of gas clusters as they expand and coalesce and the local increase in water pressure due to fluid redistribution along the gas-water interface [Måløy et al., 1992; Xu et al., 2008].

We capture the interplay between pore pressure and dissociation by computing the decomposition rate of each hydrate crystal using a kinetic model. The hydrate mass dissociated during each time step Δt, $\Delta m_h = (dm_h/dt)\Delta t$, is determined according to a driving force which is proportional to the difference between the phase equilibrium fugacity f_{eq} and the methane fugacity at the hydrate crystal surface f [Kim et al., 1987],

$$\frac{dm_h}{dt} = -K_h \exp\left(\frac{-E}{RT}\right) F_A A_h \left(f_{eq} - f\right). \tag{47}$$

where K_h is the hydration reaction constant, E is the hydration activation energy, A_h is the surface area for the reaction, and $R = 8.314$ J mol^{-1} K^{-1} is the universal gas constant. Negative Δm_h implies decreasing mass. The area A_h is computed from the hydrate crystal volume (which is updated in time as it shrinks), assuming spherical crystal with area adjustment factor of $F_A = 1$. We evaluate f_{eq} and f from the equilibrium pressure p_{eq} (for a given temperature T) and the pressure of gas surrounding the dissociating crystal, p_g. The reverse process, hydrate reformation, can occur locally upon reversal of the driving force ($p_{eq} > p_g$) [Waite et al., 2008]; this process is excluded from our current model.

The gas pressure in each gas cluster, p_g, is evaluated through the ideal-gas equation of state (EOS), where we compute the cluster volume V_g from mass balance. Each mole of dissociated hydrate (with volume of $\Delta V_h = M_h/\rho_h$) is converted to N_h moles of water, which occupies a volume of $\Delta V_w = N_h M_w/\rho_w$. Here, $\rho_h = 900$ kg/m^3, $M_h = 0.119$ kg/mol, $\rho_w = 1000$ kg/m^3 and $M_w = 0.018$ kg/mol are the density and molar mass of methane hydrate and water, respectively, and $N_h = 5.75$ is the hydration number [Sloan and Koh, 2008]. To obtain the cluster volume V_g we note that $\Delta V_w/\Delta V_h \approx 0.8$, hence the remainder 20% of the dissociated hydrate volume ΔV_h is replaced with gas. For simplicity, we use here the ideal gas law, $p_g V_g = n_g RT$, where n_g is the number of gas moles in the cluster. We have confirmed that the use of a more accurate EOS does not alter our results substantially; for example, the difference between overpressures evaluated with the ideal gas law and with the EOS in Duan et al. [1992] in several representative simulations is $\sim$0.1%. The number of gas moles n_g is computed from the number of dissociated hydrate moles, $\Delta n_h = \Delta m_h/M_h$. Given the low solubility of methane in water [Sloan and Koh, 2008], we consider only two methane phases, hydrate and gas, neglecting the small quantities that dissolve in water.

Our model incorporates the two-way coupling between fluid displacement and mechanical deformation: pore opening in response to pressure loading (direct coupling), and alteration of the flow properties by grain rearrangements (reverse coupling) [Holtzman and Juanes, 2010]. A deformable porous material is represented by a 2-D square lattice of dented blocks (grains), connected mechanically by nonlinear springs [Fig. 94(a)]. The voids between the blocks define a pore network: the narrow openings at the contacts are the pore throats, which connect the larger openings (pore bodies). Variation in block shapes leads to variability in throat apertures, which is assumed to be uncorrelated in space. This provides two interacting networks, solid and fluid, whose nodes are the grain centers and the pore bodies, respectively. We solve for displacement of the grains and fluid pressures at the pore bodies.

Pore-scale disorder in hydraulic properties is represented by assigning a distribution of initial area A and permeability k to the pore throats. Both parameters scale with the square of the throat aperture r, that is, $A \sim r^2$, $k \sim r^2$ (assuming Stokes flow in cylindrical tubes provides $A = \pi r^2$, $k = r^2/8$). We characterize the disorder in the hydraulic properties through a scalar parameter, $\lambda \in (0, 1)$, drawing values from a uniform distribution, $r \in [1 - \lambda, 1 + \lambda]\bar{r}$, where $\bar{r} \sim a$. The characteristic length scale is the pore size a, which here we take as half the distance between nodes in the lattice [Fig. 94(a)]. Partially-drained conditions are simulated through a decrease in permeability and throat area at the boundary (each by 3 orders of magnitude, equivalent to a reduction in throat aperture by a factor of $10^{3/2}$) relative to the sample's interior. We enforce a

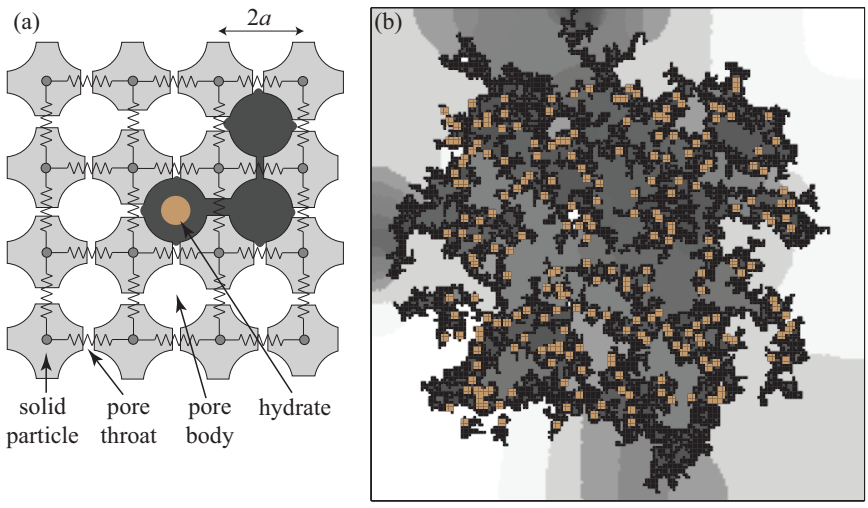

Figure 94: (a) Schematic of the pore-scale model. The solid matrix is represented by a square lattice of dented blocks (grains), connected mechanically by springs. The narrow openings between the grains are the pore throats, which connect the larger openings (pore bodies). Some pores are filled with hydrate crystals (brown), which decompose into water (white) and free gas (dark gray). (b) Pore pressure during simulation of dissociation. The grayscale intensity represents the pressure scaled to increase contrast: white corresponds to the ambient pressure p_0, black to high pressures in gas filled pores. The location of clusters of 3×3 pores originally occupied by hydrate crystals is marked in brown. The pressure halo that develops ahead of newly invaded pores reflects the finite timescale required for pressure dissipation. We use a network of 200×200 pores with $\lambda = 0.2$, $\epsilon_0 = 0.01$, $a = 1\,\mu$m, $\mu = 10^{-3}$ Pa s and $\gamma = 0.07\,$N/m. A system in equilibrium at $T_0 = 0.5°$C and $p_0 = 2.58$ MPa is subjected to $\Delta T = 10°$C.

constant hydrostatic pressure p_0 at the boundary pores.

In simulating flow we assume that gas is inviscid, such that its pressure adjusts instantaneously and is uniform within each cluster. The water pressure in a water-filled pore is updated from mass conservation at a pore body: $p_w(t+\Delta t) = p_w(t) + \sum_j q^j \Delta t/(c_t V)$, where V is the pore volume, c_t is an effective compressibility of the system (see below), and the summation is over all neighboring pores. The volumetric flow rate between the pore and its neighbor j is given by Darcy's law $q^j = (Ak/\mu)(p^j - p_w)/\ell^j$, where μ is the water dynamic viscosity and ℓ^j is the length over which the pressure drop $p^j - p_w$ occurs. For flow between two water-filled pores, $\ell^j = 2a$. If pore j is gas-filled, the meniscus between the two pores starts advancing once the capillary pressure exceeds the capillary entry pressure, $p^j - p_w > 2\gamma/r$, where γ is the gas-water interfacial tension. As the meniscus advances, the length is updated by $\ell^j(t+\Delta t) = \ell^j(t) - (q^j/A)\Delta t$.

The gas generated by hydrate dissociation invades the porous medium, displacing water. Slow drainage in disordered media occurs in the form of bursts ("Haines jumps" [Haines, 1930]), which lead to sudden changes in water pressure. When one or more pores are invaded during a burst, the interface menisci at neighboring pores readjust, receding along throats or even leading to a backfilling of previously invaded pores [Måløy et al., 1992; Xu et al., 2008]. This phenomenon suppresses further invasion until the excess water pressure is dissipated, thus limiting the burst size. The aggregate behavior resulting from this phenomenon is an effective system compressibility,

$c_t = a/\gamma$ [Holtzman and Juanes, 2010]. The finite time required for pressure dissipation leads to the development of a pressure halo around the expanding gas clusters [Fig. 89(b)].

Changes in pore pressure cause grain rearrangements, which are represented in our model through contraction of the springs over time, $h(t)$. We highlight the effect of disorder in flow properties by using uniform spring stiffness K and enforcing an initially uniform contraction of all spring, h_0, corresponding to a macroscopic strain $\epsilon_0 = h_0/2a$. This guarantees an initially uniform pre-stressed state, which becomes spatially-variable upon hydrate dissociation. The confinement ϵ_0 is sufficiently large to prevent granular flow. Each grain is subject to two types of forces: pressure and contact forces. The force exerted by the fluid occupying an adjacent pore body is oriented at 45° relative to the lattice axes and is of magnitude $f_p = pA_p$, where $A_p \sim a^2$ is the area upon which the pressure p acts. The intergranular contact forces f_c are updated by $f_c(t + \Delta t) = f_c(t) + K\Delta h$, where $\Delta h = h(t + \Delta t) - h(t)$ is the change in spring contraction. Grain positions are determined at the new time step by imposing force balance at every grain, $\sum(\vec{f_p} + \vec{f_c}) = \vec{0}$, which leads to a linear system of equations in Δh. Grain displacements impact fluid flow by modifying the throat apertures. We evaluate changes in apertures and in intergranular forces from the grain displacements in analogy with cubic packing of spherical grains with frictionless, Hertzian contacts, such that $\Delta r = -\Delta h(1-\epsilon)/[2\sqrt{1+(1-\epsilon)^2}]$, where $\epsilon = h(t)/2a$ [Jain and Juanes, 2009], and $K = 2E^*\sqrt{R^*h}$, where $R^* = a/2$, and E^* is the constrained Young modulus of the grain material [Johnson, 1987; Holtzman and Juanes, 2010]. We model an unconsolidated sediment with negligible tensile strength. Therefore, a spring is removed when there is net elongation between blocks ($h < 0$). A small cohesive force is applied as a regularization parameter.

Results

Our simulations demonstrate that the pressure always remains below the equilibrium value, $p_{eq}(T)$. Self-preservation, where increasing gas pressure diminishes the driving force for further dissociation [Eq. (47)], is evident from the decreasing rate of pressure buildup by dissociation between gas invasion (pore filling) events. Furthermore, comparison of the gas and water pressure evolution indicates that the timescale for pressure buildup by dissociation, t_{d}, is much larger than that of pressure dissipation following gas invasion of one or more pores and water flow ahead of the moving meniscus, t_{p} (Fig. 95). The contrast in timescales can be deduced by scaling: $t_{\mathrm{p}} \sim L_{\mathrm{p}}^2/D$, where $D = (k/\mu)/c_t$ is the hydraulic diffusivity, and L_{p} is the characteristic distance over which pressure dissipation takes place. With $k \sim a^2$ and $c_t \sim a/\gamma$ we obtain $t_{\mathrm{p}} \sim \mu L_{\mathrm{p}}^2/(\gamma a)$. The dissociation timescale can be obtained from Eq. (47), by using the EOS to relate the change in the number of gas moles ($-\Delta m_h/M_h$) to the change in gas pressure, Δp_g, and assuming that the latter scales as the fugacity driving force, $\Delta p_g \sim f_{eq} - f$. This provides $t_{\mathrm{d}} \sim M_h a/[RTK_h \mathrm{exp}(-E/RT)]$. Using published values of $E = 8.1 \times 10^4$ J mol^{-1} and $K_h = 3.6 \times 10^4$ kg m^{-2} Pa^{-1} s^{-1} [Clark and Bishnoi, 2001] suggests that t_{p} is smaller than t_{d} by 4 to 8 orders of magnitude, depending on the value of L_{p}; $L_{\mathrm{p}} \sim a$ provides an upper bound of 10^8, whereas the contrast becomes smaller as L_{p} approaches the system size. Since L_{p} reflects the spacing between gas clusters, the timescale ratio will be between the two values.

The rapid dissipation of pressure by drainage relative to its buildup by dissociation implies that the pressure evolution is governed by capillary effects: once the gas pressure exceeds the sum of the water pressure p_w and entry pressure p_c^e in an adjacent water-filled pore, gas expands by invasion

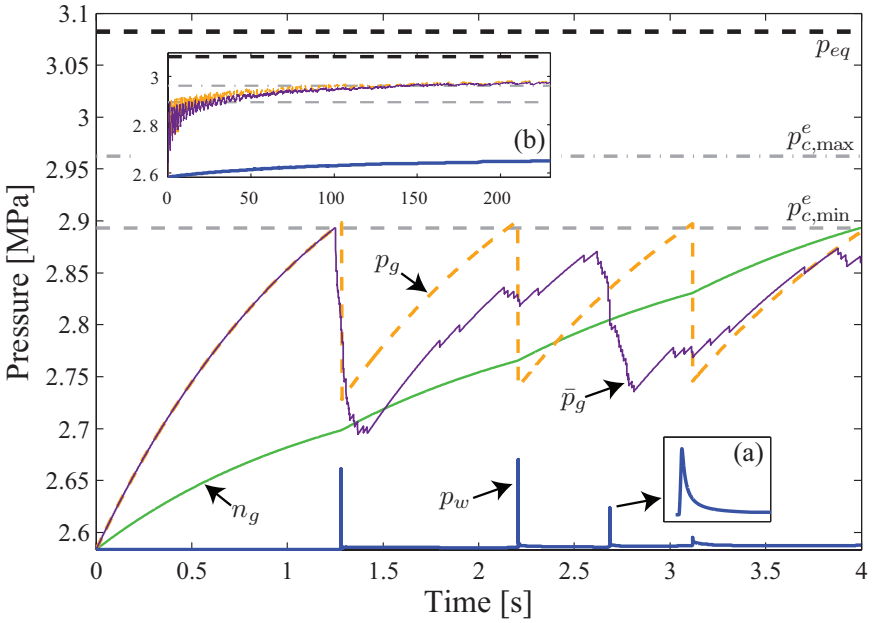

Figure 95: Pressure evolution during thermally-induced hydrate dissociation. The pressures p_g and p_w shown in the plot are measured in a specific gas cluster and in an adjacent pore, respectively. The effect of expansion and coalescence of different gas clusters is captured by the mean gas pressure, $\bar{p}_g = \sum_j (p^j V^j) / \sum_j V^j$ (summation over all gas-filled pores). The concave shape of both the gas pressure p_g and the (normalized) number of moles within a cluster n_g demonstrates the self-preservation mechanism: reduction in dissociation rate as p_g increases. The sharp drop in p_g marks gas expansion during an invasion event: once p_g exceeds the sum of the capillary entry pressure p^e_c and the water pressure in an adjacent water-filled pore p_w, gas invades that pore. The timescale for pressure buildup by dissociation, t_{d} $\sim$1 s, is 5 orders of magnitude larger than that of pressure dissipation following an invasion event, t_{p} $\sim 10^{-5}$ s [between the peak and the plateau in inset (a)]. During the entire simulation [inset (b)], the gas pressure is constrained by both thermodynamics ($p_g < p_{eq}$) and hydrodynamics ($p_g < p^e_c + p_w$). We use a network of 100$\times$100 pores and $\lambda = 0.1$. Here, we simulated a relative low temperature increase, $\Delta T = 1.5$°C, to emphasize the effect of self-preservation.

and its pressure drops. For the scale of interest here, we can understand gas invasion driven by hydrate dissociation as a quasi-static process, where the water pressure relaxes quickly to a value close to p_0 (Fig. 95). Thus, gas overpressure is controlled by the capillary entry thresholds for gas invasion.

To demonstrate the role of capillarity we compare the maximum pressure that develops during the simulations (until complete dissociation) in systems of different permeability. We vary the permeability by scaling a given aperture distribution (r_0, similar in all samples) by a pore-to-throat parameter $\beta = r_0/r$, keeping the pore size a fixed. The resulting gas overpressures in most simulations are bounded between the minimum and maximum capillary entry pressures, $p^e_{c,\text{min}} = 2\gamma/[(1+\lambda)\bar{r}]$ and $p^e_{c,\text{max}} = 2\gamma/[(1-\lambda)\bar{r}]$, with values closer to $p^e_{c,\text{max}}$ as the permeability increases and to $p^e_{c,\text{min}}$ as it gets smaller (Fig. 96). This behavior is caused by two mechanisms: heterogeneity and matrix deformation. The higher capillary pressures that develop in low-permeability systems result in smaller number of invaded pores (higher-density gas compressed into a smaller volume), where the invasion of only the widest throats (lowest p^e_c) implies that a smaller portion of the aperture distribution is sampled. In addition, higher capillary entry pressures cause more pore opening through grain rearrangements, creating fractures [Jain and Juanes, 2009; Holtzman and Juanes, 2010]. Fracturing allows gas invasion at a capillary pressure lower than the original threshold p^e_c in the undeformed system. Fractures as conduits for gas migration have been observed in experiments [Boudreau et al., 2005] and inferred in the field [Scandella et al., 2011]. In our model, for a given aperture distribution, the mode of invasion is determined by the grain stiffness (E^*) and the external confinement (ϵ): fracturing tends to occur in softer sediments under lower confinement [Holtzman and Juanes, 2010]. In addition, fracturing is more pronounced in sediments with lower heterogeneity in hydraulic properties, corresponding to smaller values of λ (Fig. 97).

Finally, the scaling of the characteristic time for dissociation t_d suggests that it can become comparable to that of pressure dissipation t_p if the kinetics were much faster, that is, for much larger reaction constant K_h or characteristic distance L_p values. We investigate this theoretical limit by simulating dissociation with K_h values up to 10^4 higher than published values [Clark and Bishnoi, 2001]. While the resulting overpressures are higher than those of a quasi-static process controlled by the capillary entry pressures, they always remain well below the thermodynamic equilibrium value p_{eq}.

Conclusions

In conclusion, we have shown that the overpressure from hydrate dissociation in sediments is governed by the competition between kinetic dissociation rate and pressure dissipation. Due to self-preservation, the overpressures cannot exceed the phase equilibrium pressure, regardless of the heat supply and sediment permeability. If the intrinsic kinetic rate was many orders of magnitude faster than its published value, the dissociation rate could be controlled by the ability of the medium to dissipate the pressure. Our results suggest, however, that the timescale for pressure buildup by dissociation is much larger than that of pressure dissipation by drainage, even for low-permeability sediments. We can thus view gas invasion driven by dissociation as a quasi-static process, where the water pressure relaxes quickly and the gas pressure is limited by the characteristic capillary thresholds. Hence, the pressure evolution is dominated by hydrodynamics, where the maximum pressure depends on the mode of gas invasion. In systems with large pore apertures,

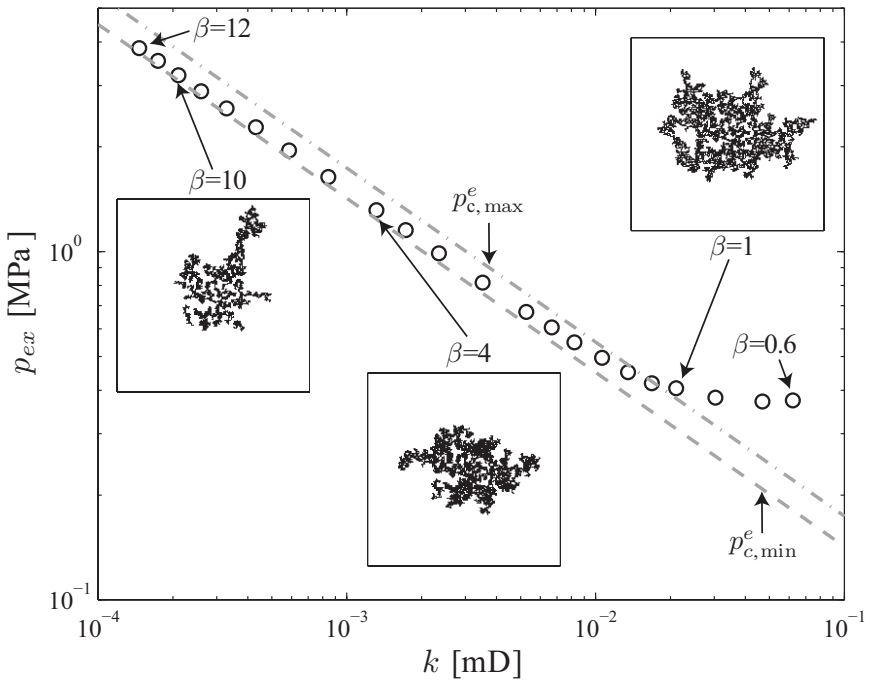

Figure 96: Mean overpressure $p_{ex} = \bar{p}_g - p_0$ and typical invasion pattern (insets) in systems of different permeability $k \sim \bar{r}^2$ (varied by scaling the aperture distribution by β). Because dissipation of pressure by drainage is much faster than its buildup by dissociation, the overpressure is governed by the capillary entry thresholds. In most simulations, $p^e_{c,\min} < p_{ex} < p^e_{c,\max}$. As the permeability becomes smaller, p_{ex} approaches the lower bound $p^e_{c,\min}$, due to the combined effect of heterogeneity and deformation. In low-permeability systems, the highly-pressurized gas occupies a smaller volume and hence samples a smaller portion of the aperture distribution, with only the widest throats (lowest p^e_c) invaded. In addition, the high capillary pressures can lead to fracture opening, which is the preferred mode of gas invasion in soft, fine-grained sediments (see Fig. 97). In the coarsest samples ($k > 0.02$ mD), the overpressures slightly exceed $p^e_{c,\max}$ (by $\sim$0.1 MPa) due to a similar increase in water pressure (Fig. 95) which elevates the gas pressure required for invasion. Such pressure increment is negligible relative to the high gas pressure that develops in lower-permeability systems. We use networks of 100$\times$100 and 200$\times$200 pores for the main plot and the insets, respectively, with $\lambda = 0.1$ and $E^* = 2$ GPa.

Figure 97: Modes of gas invasion following hydrate dissociation in systems of different permeability, showing a transition from capillary fingering for more permeable media ($\beta = 1$) to fracture opening for less permeable media ($\beta = 10$). In these simulations, we used parameters reflecting slightly lower pore-scale heterogeneity ($\lambda = 0.05$), slightly softer grains ($E^* = 1.85$ GPa) and more concentrated hydrate distribution at the center of the sample than in Fig. 96. Hydrate dissociation in the low-permeability medium (left, $\beta = 10$) leads to the creation and propagation of a fracture.

gas invades with negligible amount of matrix deformation, and the overpressures are constrained by the capillary thresholds. The overpressure may be further limited by geomechanical effects, especially in soft, low-permeability sediments where fracturing is the preferred gas invasion mechanism. Gas invasion by way of fracturing is a mechanism that offers a plausible explanation for massive sediment failure and methane venting by hydrate dissociation.

Capillary fracturing in granular media

The invasion of one fluid into a porous medium filled with another fluid occurs in many natural and industrial processes. These processes include gas venting, hydrocarbon recovery, geologic CO_2 sequestration, and soil wetting and drying. Pore-scale disorder, hydrodynamic instabilities, and mechanical deformation of the pore geometry result in complex displacement patterns. Understanding the emergent patterns is both scientifically fascinating and technologically important [Gollub and Langer, 1999].

Fluid-fluid displacements in rigid porous media have been studied in depth. While many fundamental questions remain, a basic understanding of the different displacement regimes, including compact displacement, capillary fingering, and viscous fingering, has been obtained through laboratory experiments and computer simulations [Lenormand et al., 1988; Wilkinson and Willemsen, 1983; Paterson, 1984; Måløy et al., 1985; Stokes et al., 1986; Chen and Wilkinson, 1985; Yortsos et al., 1997; Ferer et al., 2004; Toussaint et al., 2005]. These regimes depend on the the flow velocity, the degree of pore-scale disorder, and the interfacial tension and viscosity contrast between the fluids.

In a deformable medium such as a granular bed, fluid flow can displace the particles and affect the pore geometry, which in turn can affect the flow. This interplay between the displacements of the fluids and the particles leads to a variety of patterns, including desiccation cracks [Meakin, 1991], granular fingers [Cheng et al., 2008], labyrinth structures [Sandnes et al., 2007], stick-slip bubbles [Sandnes et al., 2011], open channels [Kong et al., 2010; Varas et al., 2011] and fractures [Chevalier et al., 2009; Boudreau et al., 2005; Xu et al., 2008; Shin and Santamarina, 2010; Choi et al., 2011; Sandnes et al., 2011].

While fracturing during gas invasion in liquid-saturated media has been observed in several experiments [Chevalier et al., 2009; Boudreau et al., 2005; Xu et al., 2008; Shin and Santamarina, 2010; Choi et al., 2011; Sandnes et al., 2011] and simulations [Jain and Juanes, 2009], the underlying mechanisms and controlling parameters behind the morphodynamics of gas invasion in liquid-filled deformable granular media remain poorly understood. Holtzman and Juanes [Holtzman and Juanes, 2010] developed a model that predicts the transitions among capillary fingering, viscous fingering, and fracturing. The authors used pore-scale simulations and scaling analysis to show that fracturing caused by elastic deformation of particles is the dominant mode of invasion for fine, soft particles under low confining stress. In this Letter, we study fracturing in a system of rigid particles. We show that frictional sliding, rather than elastic deformation, is the key mechanism controlling fracturing. We provide experimental evidence for three displacement regimes—capillary fingering, viscous fingering, and capillary fracturing—and derive two dimensionless groups that govern the transitions among these regimes [Holtzman et al., 2012].

We inject air into a thin bed of water-saturated glass beads packed in a cylindrical cell. We prepare each granular bed by pouring beads into the cell and then vibrating it to increase the packing homogeneity (see Appendix). There are three control parameters: the mean particle diameter, d, the air injection rate, q, and the confining weight, w. The confinement is applied by weights placed on a rigid disk that rests on top of the beads. To allow fluids (but not the particles) to leave the cell, the disk is made slightly smaller than the interior of the cell (inner diameter L), leading to a thin gap along the edge of the cell. We inject the fluids with a syringe pump at a fixed rate to the center of the cell, and image the invasion pattern during the experiment with a digital camera (Fig. 98). To analyze the images, we subtract the initial image prior to injection. For most experimental

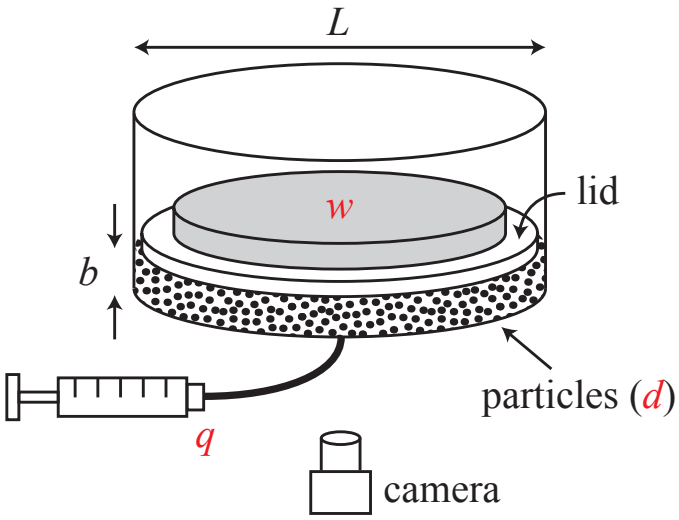

Figure 98: Experimental setup: a thin bed (thickness b) of water-saturated glass beads (mean diameter d) is confined in a cylindrical acrylic cell (internal diameter L). Vertical confinement is supplied by a weight, w, placed on a disk ("lid") that rests on top of the beads. The disk is slightly smaller than the cell to allow fluids (but not particles) to leave the cell. Air is injected into the center of the cell at a fixed flow rate q. Time-lapse images are captured by a camera placed underneath the cell.

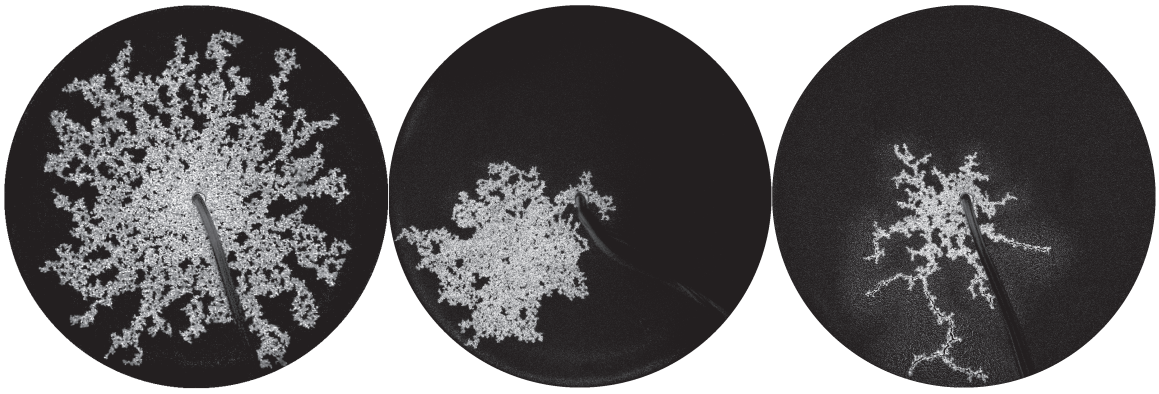

Figure 99: Examples of experimentally-observed patterns. We classify these patterns into three regimes: viscous fingering, capillary fingering, and fracturing. In these difference images, obtained by subtracting the initial image prior to air invasion, air shows as clear white, water and beads as black, and deformed regions as a sparkly halo (bead displacements changes the reflected light). Experimental conditions: d=360 μm; w=181 N (a, b) and 3 N (c); and q=100 (a), 0.1 (b), and 1 mL/min (c).

conditions, we perform repeatability experiments.

The experiments exhibit three displacement regimes: viscous fingering, capillary fingering, and capillary fracturing. We identify the regimes based on the qualitative characteristics of the invasion pattern, as has been done previously [Paterson, 1984; Chen and Wilkinson, 1985; Lenormand et al., 1988; Chevalier et al., 2009; Holtzman and Juanes, 2010]. In viscous fingering, the air-water interface grows continuously and at several locations simultaneously. The resulting pattern is radial and exhibits thin fingers and few trapped water clusters. The pattern appears more space-filling than in 2-D experiments (e.g. in a monolayer of beads [Måløy et al., 1985]) because in 3-D water clusters that appear to be trapped actually remain connected vertically across layers (Fig. 99a). In capillary fingering, the air-water interface propagates intermittently at alternating locations, leading to a pattern that is non-radial, irregular, and patchy, with multiple trapped water clusters (Fig. 99b). In capillary fracturing, the air-water interface advances continuously in thin fingers with long, straight segments. The resulting pattern is asymmetric and occupies a much smaller portion of the cell compared with capillary fingering and viscous fingering. While capillary fracturing exhibits a distinct morphology, we identify it exclusively from visual observation of bead displacements. These displacements appear as "halos" in the subtracted images, caused by changes to light reflection by bead displacements (Fig. 99c). The three regimes display transition zones, in which the invasion patterns exhibit mixed characteristics of the end-member patterns.

The mode of displacement depends on the competition between forces. The transition between capillary fingering and viscous fingering depends on the competition between viscous forces and capillary forces, whereas the transition between fingering and fracturing depends on the competition between hydrodynamic forces that promote pore opening, and mechanical forces that resist it. Since these forces depend on a combination of the control parameters, the same transition between the regimes can be achieved by changing different parameters: the displacement can transition from capillary fingering to viscous fingering by increasing the injection rate, q, or reducing the bead size, d; and from fingering to fracturing by reducing the confining weight, w, or the bead size, d (Fig. 100). The wide transition zone between capillary and viscous fingering has been observed previously [Lenormand et al., 1988], and is due to gradual changes in the governing forces with the experimental conditions. The capillary fracturing patterns transition from few, small fractures to many, large fractures as the confinement is reduced, though this trend is not conveyed in the plots since our identification of fracturing does not account for the frequency or magnitude of bead displacements. Repetition of experiments with similar conditions yield the same invasion regime, even if the details of the invasion pattern differ.

We rationalize these transitions by computing the ratio between the driving forces that promote the development of a particular pattern. For a rigid medium, the transition between capillary fingering and viscous fingering occurs when the characteristic macroscopic viscous pressure drop in the direction parallel to flow, δp_{v}, exceeds the variation in capillary entry pressures along the interface, δp_{c}. We compute δp_{v} as $\nabla p_{\mathrm{v}} L$, and use Darcy's law, $\nabla p_{\mathrm{v}} \sim \eta v/k$ with $k \sim d^2$, to obtain $\delta p_{\mathrm{v}} \sim \eta v L/d^2$. Here, η is the dynamic viscosity of water, and $v \sim q/(bd)$ is the flow velocity. We use a fixed value of the macroscopic length scale with $L \gg d$ for the viscous pressure drop in the defending phase, an assumption that is justified during the initial stages of the invasion but that becomes questionable at later stages, when the invasion front approaches the system's boundaries and becomes fractal [Lenormand, 1989]. The maximum difference in capillary pressures along the interface is $\delta p_{\mathrm{c}} = \gamma/r_{\mathrm{min}} - \gamma/r_{\mathrm{max}} \sim \gamma\chi(\lambda)/\bar{r}$, where γ is the air-water interfacial tension, $\bar{r} \sim d$ is the mean throat aperture, and $\chi(\lambda)$ describes the distribution of throat apertures, a function of the

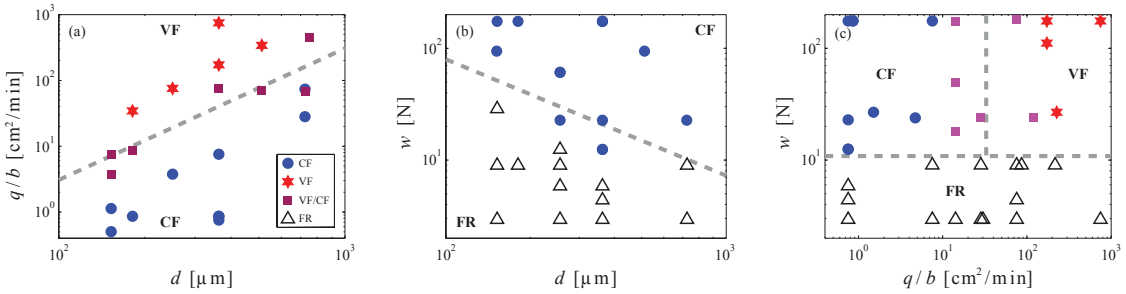

Figure 100: Phase diagrams of fluid-fluid displacement patterns in the experiments. The diagrams demonstrate how changing the control parameters affects the patterns. Diagram (a) shows that the transition from viscous fingering (VF) to capillary fingering (CF) occurs at $q/b \sim d^2$ (fixing w=181 N). Intermediate patterns are marked as VF/CF. Diagram (b) shows that the transition from capillary fingering to fracturing (FR) occurs at $w \sim d^{-1}$ (q=0.1 mL/min). Diagram (c) shows that the transition from fingering to fracturing is independent of q/b (d=360 μm).

degree of pore-scale disorder $\lambda \in (0, 1)$ [Holtzman and Juanes, 2010]. For instance, for a uniform aperture distribution, $r \in [1-\lambda, 1+\lambda]\bar{r}$, we get $\chi(\lambda) = \lambda/(1-\lambda^2)$.

The transition from viscous to capillary fingering occurs when $\delta p_\mathrm{v} \sim \delta p_\mathrm{c}$, and is therefore controlled by the following "modified capillary number", $\mathrm{Ca}^* = \delta p_\mathrm{v}/\delta p_\mathrm{c}$:

$$\mathrm{Ca}^* = \mathrm{Ca}\frac{L}{d}\chi^{-1}(\lambda) = \frac{\eta q L}{\gamma b d^2}\chi^{-1}(\lambda), \tag{48}$$

where $\mathrm{Ca} = \eta v/\gamma$ is the classical capillary number. For a given pair of fluids, the viscosity and interfacial tension are fixed. Assuming similar disorder across experiments, this scaling suggests that the phase boundary between viscous fingering and capillary fingering is $q/b \sim d^2$, in agreement with our experimental data (Fig. 100a).

In a granular medium, fractures open when forces exerted by the fluids exceed the mechanical forces that resist particle rearrangements. In cohesionless granular material, these forces include elastic compression and friction. For systems with densely packed, highly compliant particles, pore opening occurs by means of particle deformation [Holtzman and Juanes, 2010]. However, for many types of particles including most mineral grains and manufactured beads, the high particle stiffness limits interparticle compression, making frictional sliding the dominant deformation mechanism that alters the pore geometry.

To demonstrate this quantitatively, we compare the two characteristic resisting forces. The increment in elastic compressive force associated with a relative particle displacement (interparticle deformation) Δh is $\Delta f_\mathrm{e} \sim K\Delta h$, where K is the interparticle contact stiffness. The stiffness $K \sim E\sqrt{dh}$ is computed by assuming Hertzian interparticle forces, $f_\mathrm{e} \sim E\sqrt{d}h^{3/2}$, where E is the Young's modulus of the particle material and h is the total interparticle deformation [Johnson, 1987]. We evaluate K at $h = h_0$, where h_0 is the initial (prior to fracturing) interparticle deformation. We obtain h_0 from the expression for the initial interparticle force, $f_{\mathrm{e},0} \sim E\sqrt{d}{h_0}^{3/2}$, which, assuming homogenous force distribution, can also be evaluated from the vertical confinement, $f_{\mathrm{e},0} \sim w/(L/d)^2$. Fracturing requires a sufficiently large change in the throat apertures, $\lambda\bar{r} \sim \lambda d$, implying interparticle displacement of $\Delta h \sim \lambda d$. The elastic resisting force is therefore $\Delta f_\mathrm{e} = \lambda E^{2/3} L^{-2/3} w^{1/3} d^2$. We compare this force with the frictional resistance force, evaluated

from the limiting value at sliding, $\Delta f_{\mathrm{f}} \sim \mu f_{\mathrm{e},0} \sim \mu w/(L/d)^2$, where μ is the coefficient of friction. The resulting force ratio is then:

$$\frac{\Delta f_{\mathrm{e}}}{\Delta f_{\mathrm{f}}} = \frac{\lambda E^{2/3} L^{4/3}}{\mu w^{2/3}}. \tag{49}$$

For our experimental system, with E=70 GPa, μ = 0.3 [Li et al., 2005], L=0.2 m, λ=0.75 and w=3–181 N, the elastic resistance is 5–6 orders of magnitude higher than frictional resistance, suggesting that pore opening occurs by overcoming friction. Elasticity would play an important role in fracturing only for much softer beads and much larger confining stresses.

We predict the emergence of fracturing through a dimensionless parameter we call the "fracturing number", N_{f}, that measures the system deformability as the ratio of the pressure forces that drives fracturing, Δf_{p}, and the resisting force, Δf_{f}. The driving force is the product of the local pressure difference at the front tip, Δp, and the area over which it acts, $A_p \sim d^2$. The pressure difference is the sum of the capillary pressure, γ/d, and the local viscous pressure drop, $\nabla p_{\mathrm{v}} \sim \eta v/d$. Thus, $\Delta f_{\mathrm{p}} = \gamma d + \eta v d = \gamma d(1 + \mathrm{Ca})$, and

$$N_{\mathrm{f}} = \frac{\gamma L^2}{\mu w d}(1 + \mathrm{Ca}). \tag{50}$$

This scaling suggests that, for a given fluid pair, particle material, and system size, the transition from fingering to fracturing occurs at $w \sim d^{-1}$. This is consistent with our observations (Fig. 100b). While the scaling accounts for the effects of both the capillary pressure and the local viscous pressure drop, the capillary pressure is the dominant cause of fracturing in our experiments (with $\eta \approx 10^{-3}$ Pa s, $\gamma \approx 0.07$ N/m, $q \leq 100$ mL/min, and therefore $\mathrm{Ca} \ll 1$). As a result, the observed transition does not depend on the flow rate (Fig. 100c).

The scaling analyses allow us to collapse our data from a three-parameter dimensional phase space (q, w, d) into a two-parameter dimensionless space (Ca^*, N_{f}). For $N_{\mathrm{f}} \gg 1$, fracturing is the dominant mode of invasion. For $N_{\mathrm{f}} \ll 1$, the medium is essentially rigid (negligible particle rearrangements), and the transition from capillary to viscous fingering occurs at $\mathrm{Ca}^* \approx 1$ (Fig. 101).

These results demonstrate and rationalize the crossover among three regimes of drainage in granular media: capillary fingering, viscous fingering, and capillary fracturing. They show that the crossover between capillary fingering and viscous fingering can be characterized by a modified capillary number, Ca^*. Our results demonstrate the emergence of capillary fracturing, in which capillary forces dilate pore throats by exceeding the internal frictional resistance of the medium. The scaling of the fracturing number [Eq. (50)] suggests that, in granular systems with rigid solid particles, capillary fracturing tends to occur when the particle size falls below a critical value, $d_c \sim \gamma L^2/\mu w$. This provides a rationale to observations of capillary-induced fracturing in a variety of natural systems, such as drying in granular media [Meakin, 1991; Xu et al., 2008], gas venting in lake sediments [Boudreau et al., 2005; Scandella et al., 2011], and hydrate veins in the ocean floor [Hester and Brewer, 2009]. In all of these settings, the formation of fractures provides open conduits that allow fast exchange of elements, which are likely critical to the water, carbon and energy budgets in the biosphere.

Appendix. Experimental procedure

We begin the experiments by pouring a known volume V of glass beads with mean diameter d into a cylindrical acrylic cell of internal diameter L. To distribute the beads uniformly across the

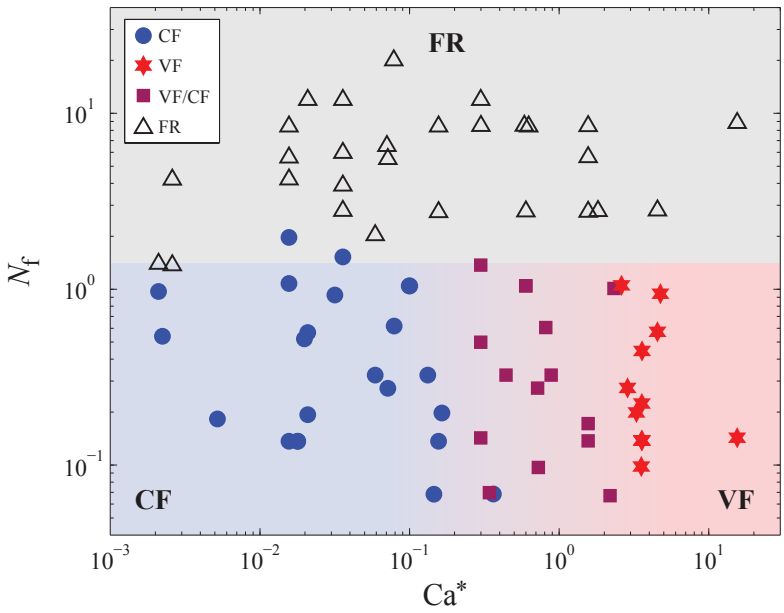

Figure 101: Phase diagram of drainage in granular media, showing three invasion regimes: viscous fingering (VF), capillary fingering (CF), and fracturing (FR). The dashed lines denote the approximate locations of the transitions among regimes. The tendency to fracture is characterized by the "fracturing number" N_f: drainage is dominated by fracturing in systems with $N_f \gg 1$. At lower N_f values, the type of fingering depends on the modified capillary number, Ca^*.

cell and homogenize the packing, we vibrate the cell by tapping on it in the horizontal direction in two rounds: first with no confinement, and then after placing an acrylic disk (the "lid" in Fig. 1, weighing 0.3 kg) on top of the beads. After tapping, the bed is a few layers thick with approximate thickness $b = V/(\pi L^2/4)$. To saturate the bed, we place weights (18.5 kg total mass including the lid) on top of the lid and then inject water at a constant rate into the center of the cell with a syringe pump. We inject at a sufficiently high rate to avoid trapping of air, but at a sufficiently low rate to avoid displacing the beads. After the bed is saturated, we load the desired weight w onto the lid and inject air at a constant rate q. To observe the invasion pattern, we illuminate the bottom of the cell with reflected light from LED panels and take images with a digital camera.

Creating a mechanically and hydraulically homogeneous packing—with uniform distribution of interparticle forces and pore apertures—is an extremely difficult task. We evaluate the hydraulic homogeneity by observing the invasion front of the water during the initial saturation step: a radially symmetric, circular invasion front indicates that the permeability field is homogeneous in the cross-radial (θ) direction. We infer that a symmetric, circular front also indicates permeability homogeneity in the radial direction. We further infer that a bed that is hydraulically homogeneous is also mechanically homogeneous. We reject experiments for which the invasion pattern during water injection is not circular.

To investigate the reproducibility of our results, we perform repeatability experiments for most of the experimental conditions. For a given condition, the invasion patterns in the experiments differ in the details—since our packing procedure does not create a perfectly homogeneous or reproducible bed—but always fall in the same regime.

A conduit dilation model of methane venting from lake sediments

Introduction

Atmospheric methane (CH_4) concentrations have risen steadily over the past two centuries, following an anthropogenically-driven trend that is similar to that for carbon dioxide [IPCC, 2007]. Global warming is in turn affecting natural methane emissions, particularly in the largely land-covered Northern latitudes where newly-produced methane is often emitted directly to the atmosphere through an intervening (oxidizing) biofilter [Rudd et al., 1974], accessing carbon long sequestered from the global carbon cycle [Walter et al., 2006; Archer et al., 2009]. Ebullition of methane from sediments in lakes, the deep ocean, wetlands, and estuaries is a primary means for emitting methane to the ocean-atmosphere system [Walter et al., 2006; Solomon et al., 2009; Shakhova et al., 2010; Greinert et al., 2010; Bastviken et al., 2011].

Past studies have made fundamental contributions to understanding the life cycle of methane in sediments including microbial methane production, bubble growth and migration within sediments, emission at the sediment-water interface, and bubble rise, dissolution and oxidation in the water column [Martens and Klump, 1980; Valentine et al., 2001; Judd et al., 2002; Rehder et al., 2002; Heeschen et al., 2003; Boudreau et al., 2005; Leifer and Boles, 2005; McGinnis et al., 2006; Greinert et al., 2010]. The importance of methane gas in limnetic environments has also been long recognized [Fechner-Levy and Hemond, 1996], and evidence is mounting that transport of methane in the gaseous phase dominates dissolved transport both within lake sediments and once methane reaches the water column [Crill et al., 1988; Keller and Stallard, 1994; Walter et al., 2006; Delsontro et al., 2010; Bastviken et al., 2011]. The magnitude of the atmospheric release—the portion of bubbles not dissolved during rise through the water column—depends on the mode and spatiotemporal character of venting from sediments [Leifer et al., 2006; Gong et al., 2009], so models of methane transport in the sediment column must reproduce the spatiotemporal signatures of free-gas release from the underlying sediments to correctly predict the fraction that by-passes dissolution and reaches the atmosphere.

Here, we introduce a quantitative model of methane production, migration and release from fine-grained sediments. We constrain and test the model against a record of variations in hydrostatic load and methane ebullition from fine-grained sediments in Upper Mystic Lake (UML), a dimictic kettle lake outside Boston, Massachusetts [Varadharajan et al., 2010] (Figure 102a). Our model is motivated by two key observations: ebullition is triggered by variations in hydrostatic load [Martens and Klump, 1980; Mattson and Likens, 1990; Fechner-Levy and Hemond, 1996; Leifer and Boles, 2005; Varadharajan et al., 2010], and gas migration in fine sediments is controlled by the opening of fractures or conduits [Boudreau et al., 2005; Jain and Juanes, 2009; Algar and Boudreau, 2010; Holtzman and Juanes, 2010]. The high degree of synchronicity in ebullative fluxes among distant venting sites located at different depths (Figure 102) suggests that the release mechanism is governed by the effective stress, which is the average stress between solid grains [Terzaghi, 1943]. We propose that gas bubbles escape by dilating conduits upward to the sediment surface as falling hydrostatic pressure reduces the compressive effective stress below the effective tensile strength of the sediments. This model of "breathing" conduits for gas release couples continuum-scale poromechanics theory with multiphase flow in porous media to capture the

episodicity and variable rates of ebullition. The ability of the model to match the flux record from UML, as well as the direct observation of episodic gas venting (Figure 102c), suggests that this mechanism indeed controls ebullition from lake sediments.

Model Formulation

Methane is generated in anoxic lake sediments by microbial decomposition of organic matter, and the generation rate depends on organic carbon availability, reduction-oxidation potential, and temperature. Once the total pressure of all the dissolved gases exceeds the hydrostatic pressure, any additional gas exsolves into a bubble. Gas bubbles—often mostly comprised of methane—grow, coalesce, and are transported vertically through the sediment until they are released into the water column. Gas is buoyant with respect to the surrounding water filling the pore space, but mobilization of gas bubbles in a rigid, fine-grained porous medium requires connected gas bubbles of very large vertical dimension [Hunt et al., 1988], $L_v \approx \frac{2\gamma}{(\rho_w - \rho_g) g r_t}$, where γ is the interfacial tension, ρ_w and ρ_g are the water and gas densities, respectively, g is the gravitational acceleration, and r_t is the pore throat radius, which is of the order of one-tenth of the particle radius. For a typical value of $\gamma \sim 0.070$ N/m, and a conservative value of the particle diameter at UML, $d_g \sim 10$ μm, we estimate that a connected bubble height $L_v \sim 30$ m would be required to overcome capillary effects. This is three orders of magnitude larger than observed bubble sizes [Martens and Klump, 1980; Sills et al., 1991; Boudreau et al., 2005], clearly indicating that capillary invasion in a rigid medium cannot explain methane venting, and that methane release must involve sediment deformation. A drop in hydrostatic load on the sediments lowers the compressive sediment stress and provides an opportunity for buoyant bubbles to overcome their confinement and expand by deforming the sediments. However, theoretical analysis shows that spherical bubbles of realistic size would be mobilized in sediments with reasonable shear strength only under unrealistically large vertical stress variations on the order 10 m of water head [Wheeler, 1990]. The ebullition record from UML [Varadharajan et al., 2010], however, shows gas venting in response to head drops of less than 0.5 m (5 kPa, Figure 102b), which implies that some other mechanism must mobilize bubbles for vertical transport.

The observation that bubbles in clayey sediments grow in a highly-eccentric, cornflake-shaped fracture pattern [Boudreau et al., 2005; Algar and Boudreau, 2010], rather than as spherical bubbles, suggests that this mode of growth may also allow for vertical mobility. The relevance of this transport mechanism in fine-grained sediments is supported by micromechanical models of gas invasion in water-filled porous media [Jain and Juanes, 2009; Holtzman and Juanes, 2010]. Following these observations, we hypothesize that the dilation of near-vertical conduits is the primary mechanism controlling free-gas flow and release from lake sediments. Instead of modelling the rise of individual bubbles through sediment, we propose that gas cavity expansion dilates a vertical conduit for free gas flow to the sediment surface (Figure 103). Since the flow conductance of these conduits is several orders of magnitude larger than that of undisturbed sediments, we assume that bubble release is much faster than the daily timescale resolved here, and in the model implementation we evacuate gas instantaneously from the entire depth range of the open conduit. We have confirmed that the flux records using this simplification are nearly identical to those from more detailed simulations that assume Darcy flow of gas through the conduits [Scandella, 2010].

Flow conduits dilate in response to changes in effective stress, σ', which is the average stress carried by the solid skeleton and is the primary determinant of deformation [Terzaghi, 1943]. When

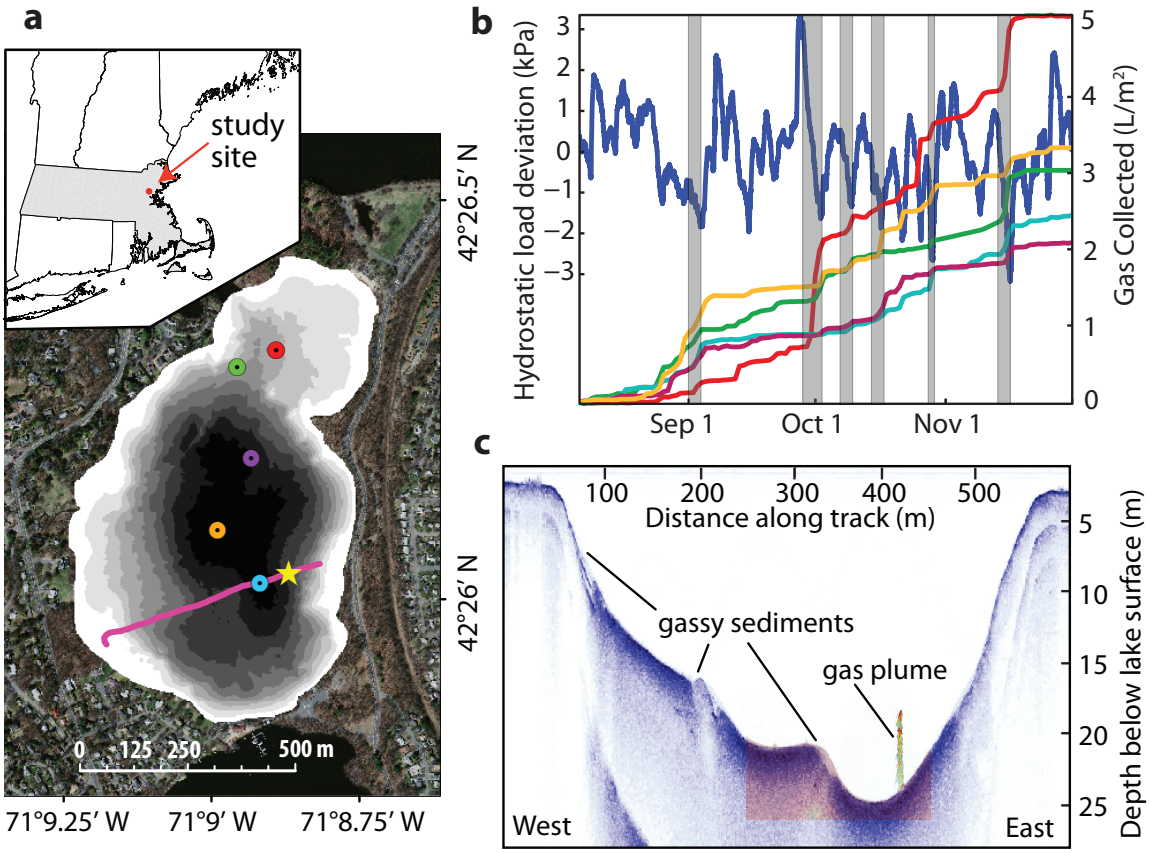

Figure 102: Spatially- and temporally-concentrated ebullition from lake sediments in response to hydrostatic pressure drops. (a) Location of Upper Mystic Lake (inset, Massachusetts shaded) and bathymetry at 2.5-m shaded intervals superposed on an aerial photomosaic. Colored circles mark bubble trap locations that produced the data shown in (b), and the profile shown in (c) was collected along the pink transect, with the star marking the gas plume location. (b) Record of hydrostatic load variations (left axis, blue curve) and cumulative gas collected (right axis) from early August through November 2008. The flux records from individual traps are highly synchronous, especially during periods of pronounced drop in hydrostatic head, denoted by grey bars. (c) Acoustic sub-bottom profile across UML (blue), where lighter shading indicates reduced reflectivity associated with gassy areas near the sediment surface. Overlain is a sonar image showing a bubble plume rising ~ 5 m from the sediments, following a drop in hydrostatic pressure in December 2009.

two fluid phases are present, the effective stress is a function of both fluid pressures [Coussy, 1995], but a series of experiments on fine, gassy sediments suggests that the overall deformation depends primarily on the total (vertical) stress and gas pressure alone [Sills et al., 1991]. This is consistent with the view that sediment and water form a coherent "mud" phase, where gas bubbles have a characteristic size much larger than the pore size [Sills et al., 1991; Boudreau et al., 2005]. Thus, we approximate the effective stress in gassy sediments as:

$$\sigma' = \sigma - P_g, \tag{51}$$

where σ is the total vertical stress—the sum of integrated bulk sediment weight and hydrostatic load—and P_g is the gas pressure. In soft, cohesive sediments, the ratio of lateral to vertical effective stress is often around one, so vertical and horizontal stresses are roughly equal. Conduits dilate when the effective stress at a particular depth becomes negative and matches the magnitude of the effective tensile strength, T.

A drop in hydrostatic load may reduce σ' to this cohesive yield limit and initiate bubble transport to the sediment surface. While the total stress is forced by changes in hydrostatic load, the gas pressure evolves in response to compression and dilation of gas cavities within a plastic, incompressible matrix of sediment and water. Therefore, two separate mechanisms are at play: cavity deformation and conduit opening. Cavity deformation changes the gas pressure and volume whenever the effective stress reaches tensile or cohesive limits. The conduits, however, open only at the tensile limit. The gas generation rate is assumed to be constant and to increase the bubble volume only. Thus, changes in gas pressure occur only in response to changes in hydrostatic load. Specifically, the gas cavities maintain their pressure until the effective stress in the surrounding matrix reaches a plastic yield limit [Coussy, 1995] under compression (C) during hydrostatic loading, or tension (T) during hydrostatic unloading,

$$-T(z) \leq \sigma'(z,t) \leq C(z), \tag{52}$$

where both $T(z)$ and $C(z)$ are assumed to increase linearly with depth from a zero value at the sediment surface, reflecting that sediment strength increases with the degree of compaction (Figure 103). Experiments confirm that the compression of gas cavities is a plastic process, in which compressed cavities do not expand upon subsequent unloading [Sills et al., 1991] (see Figure S1 of the auxiliary material). When the effective stress reaches either yield limit, the gas pressure changes during dilation or contraction to keep the effective stress within these bounds, and gas volume variations are calculated using the ideal gas law. Because gas conduits dilate at the tensile yield limit, these changes in gas pressure and volume impact the timing and magnitude of gas release from each depth interval.

The model of plastic cavity evolution and release through dynamic conduits is designed to capture the average gas venting behavior from a representative area (such as an entire lake), rather than to simulate the detailed dynamics of a single venting site. The model was run for a period of four months from an initial gas-free state, and the simulated lake-surface fluxes were compared against data from UML, which were collected near the lake surface using bubble traps (Figure 102a). Each surface-buoyed bubble trap—an inverted funnel connected to a PVC pipe that collects a column of free gas—continuously records the buoyant force from the gas as a proxy for the column height, which allows estimation of the rate at which gas enters the funnel [Varadharajan et al., 2010]. The dynamics of bubble dissolution during rise through the water column are complex [Rehder et al.,

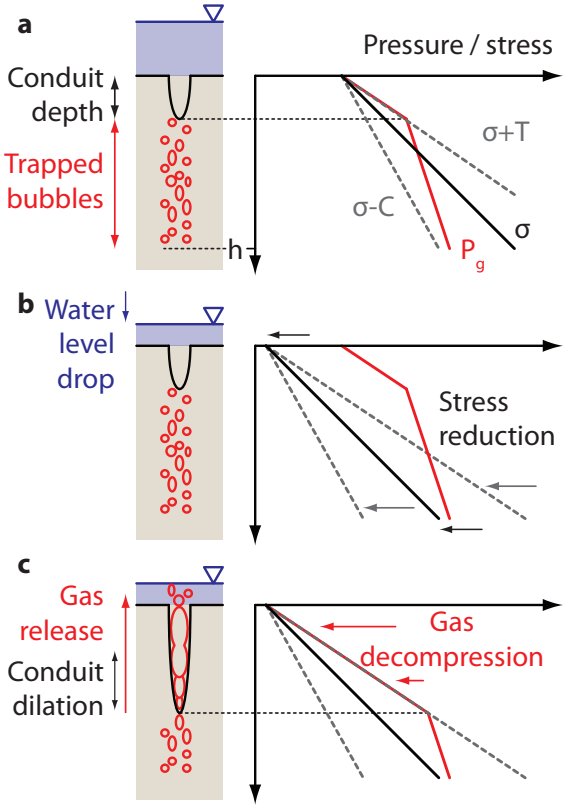

Figure 103: Model response to water level drop. (a) Initial condition: the cartoon at left shows the lake level (blue) above a sediment column with gas bubbles trapped below the open conduit depth and down to the active bubble generation depth, h (not to scale). The conduit opens to the surface from the greatest depth where the effective stress, $\sigma' = \sigma - P_g$, falls to its tensile limit, $-T$. The stress and pressure profiles at right show that this occurs when P_g (red solid line) equals $\sigma + T$ (gray dashed line). (b) A drop in hydrostatic load reduces σ throughout the sediment column. (c) Plastic cavity dilation allows shallow gas bubbles to decompress to $\sigma + T$. The conduit opens from the deepest location where $\sigma' = -T$ and releases the formerly trapped bubbles. In the case of a hydrostatic load increase (not shown), the stress rises, and the cavity compression mechanism pressurizes gas bubbles to enforce $\sigma' \leq C$, or equivalently $P_g \geq \sigma - C$. The effective stress would nowhere equal its tensile limit, and the conduit would close completely.

2002; McGinnis et al., 2006; Gong et al., 2009], and beyond the scope of this sediment-centric study. Here, we assume that volume fluxes at the sediment and lake surfaces are proportional, and the season-averaged release from the model is scaled to the season-averaged flux from the lake-surface trap data, averaged over all traps. Although the assumption of proportional fluxes at the lake bottom and lake surface is clearly an approximation (water depths at the bubble traps vary between 9 and 25 m), it is justified given the uncertainty in sensing the spatially heterogeneous surface flux using only five, randomly placed bubble traps. The assumption of constant methane generation rate is also a simplification, but it is well justified for our four-month venting record given the anoxic conditions through the measurement period and the near-sediment water temperature of $\sim 4^\circ$ C in all measurements [Varadharajan, 2009].

Results

We applied our model to study the dynamics of methane venting at UML during a period of $\sim$120 days over which gas flux was recorded (Figure 104). Because the seasonally-integrated model flux is scaled to match the cumulative gas collected by the five traps, the overall magnitude of the model flux has little significance. The timing and *relative* magnitudes of the venting events, however, are characteristics that our model predicts given the input hydrostatic pressure variations and a single, dimensionless parameter. These characteristics of the data are clearly well-reproduced, suggesting that the model captures the essential dynamics of methane ebullition.

The distribution of ebullition in time is controlled by three physical quantities: the generation zone depth, h, and the vertical gradients in tensile and compressive strength, dT/dz and dC/dz, respectively. These variables, however, do not act independently. The amount of gas released following a given drop in hydrostatic load depends on the depth to which the flow conduit dilates, and the drop required at a given depth depends on the total sediment strength, the sum of T and C. The appropriate dimensionless parameter characterizing the balance of total sediment strength and hydrostatic load variations is the *ebullition number*,

$$N_e = \frac{h(dT/dz + dC/dz)}{\Delta P_h}, \tag{53}$$

which defines the drop in hydrostatic load, normalized by an arbitrary characteristic variation ΔP_h, required to evacuate the entire active generation zone. Alternatively, N_e^{-1} defines the fraction of the active zone evacuated by a characteristic drop in hydrostatic load, ΔP_h. The value of the ebullition number, N_e, must be obtained by calibration of the model response to flux data. Taking ΔP_h as the standard deviation of nearly normally-distributed hydrostatic pressure inputs, $\sim$1 kPa, the best model fit for UML is obtained with $N_e = 5$. Smaller values of N_e in the model result in methane being released in response to smaller hydrostatic variations, and predictions that are less sensitive to extreme pressure drops—the model flux signal is composed of more frequent, smaller peaks. Larger values of N_e in the model cause gas stored deep in the sediment column to remain trapped during the smallest hydrostatic drops; this trapped gas is released more vigorously but less frequently during the largest pressure drops (see Figure S2 of the auxiliary material).

Discussion and Conclusion

We have shown that the timing and distribution of flux magnitudes predicted by our single-parameter model match the flux data, averaged over 5 traps (Figure 104). However, the methane venting signals from individual traps are composed of fewer, more vigorous events because not all venting sites activate strictly simultaneously (Figure 102b). The single parameter, called the ebullition number, controls the venting episodicity and reflects the balance between hydrostatic pressure forcing and sediment strength. The model calibration of the ebullition number ($N_e = 5$) is more representative for the average flux of the system, and larger values of N_e are required to capture the dynamics of individual venting sites.

Our mechanistic model of methane transport captures the dynamics of ebullition by coupling the plastic evolution of trapped gas bubbles with their release through dynamic flow conduits. Reproducing these dynamics is important not only to understand how gas escapes the sediments into the water column, but also to understand the subsequent dissolution and atmospheric release [Leifer et al., 2006; McGinnis et al., 2006; Gong et al., 2009; Greinert et al., 2010]. The same mechanisms likely control gas release from fine, methane-bearing sediments under other surface water bodies, including marine sediments controlled by tides [Martens and Klump, 1980] or swell [Leifer and Boles, 2005], and the model could be extended to systems where the methane source pressurizes gas sufficiently to drive the episodic releases [Tryon et al., 2002]. Our model lays the groundwork for integrated modelling of methane transport in the sediment and water column, linking estimates of methane generation [Price and Sowers, 2004] with models of water column dissolution [Leifer et al., 2006; McGinnis et al., 2006] to constrain the global methane release from lakes, wetlands, estuaries and shallow continental margins.

Appendix A. Methods Summary

Ebullition measurements.

The ebullition data were collected using surface-buoyed bubble traps, which funnel rising methane bubbles into a column and measure the gas volume collected with a temperature-corrected pressure sensor at the top. A pressure sensor fixed relative to the lake bottom measured the total hydrostatic load. Both gas flux and hydrostatic load data were recorded at 5-minute resolution and smoothed using a 1-hour moving average filter to remove noise from surface waves [Varadharajan et al., 2010].

Geophysical surveys.

Acoustic imagery was acquired in December 2009 using an Edgetech 424 Chirp fish towed $\sim$30 cm below the lake's surface and operating at 4 to 24 kHz with 4 ms sampling. Acoustic data and GPS navigation were recorded in real-time in SEGY files, and two-way travel time to depth conversion was accomplished using freshwater sound velocity of 1472 m/s. The superposed water column image of a methane plume was simultaneously captured using the 83 kHz mode of a Humminbird 798ci fishfinder with built-in GPS. The bathymetric data shown in Figure 102a were gridded in ESRI ArcMap software using lake bottom depths picked from Chirp data acquired during 3 surveys in 2009 and 2010, as well as depths independently recorded by the fishfinder in October 2010.

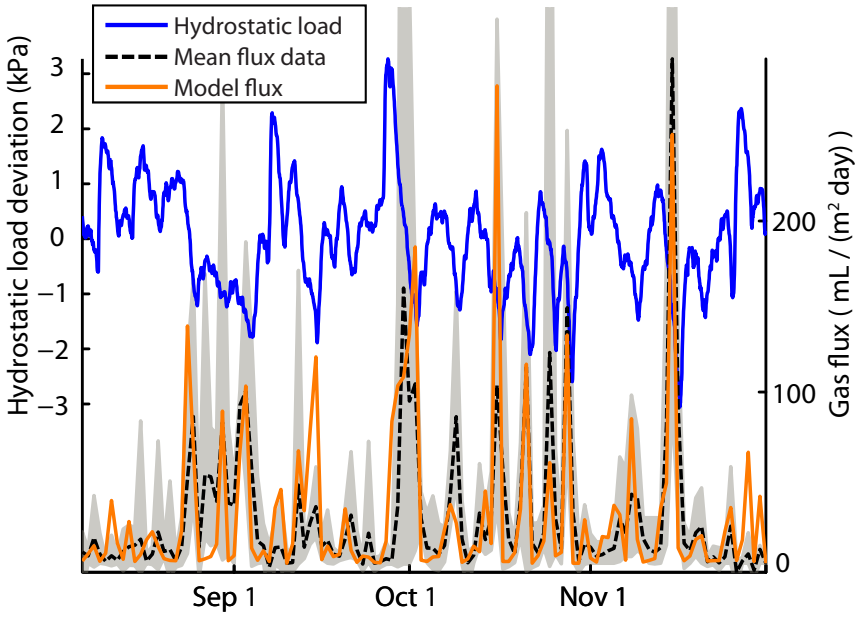

Figure 104: Best fit of model gas ebullition fluxes to data from Upper Mystic Lake. The left axis and solid blue line show a time series of the hydrostatic load forcing, and the right axis shows the methane fluxes from the mean bubble trap data (black, dashed) and model (orange, solid). The gray shaded area indicates the range of flux values from the five traps; note that in four instances the range extends above the limit of the vertical axis up to a value of $\sim$700 mL/m^2/day. The fluxes are binned daily, and the cumulative model release is constrained to match the data. The calibrated value of the ebullition number, $N_e = 5$, reflects that a hydrostatic pressure drop of about 5 standard deviations (5 kPa in this case) is required to evacuate the methane from the entire active generation depth, h (equation (3)). The single-parameter model accurately predicts the timing of large flux events and usually their magnitude, as well.

Numerical methods.

We solved the model equations numerically to evolve the gas pressure and gas saturation (fraction of the pore volume occupied by gas), in each depth interval in response to variations in the hydrostatic load at the surface. We discretized the equations in space using a second-order finite volume scheme with linear reconstruction and a central limiter to ensure monotonicity. Time integration was performed using second-order Runge-Kutta method, following the poromechanical evolutions in a staggered manner. The numerical grid was the same for poromechanics and flow, with 64 control volumes in the vertical direction. Both the cm-scale vertical resolution and hourly time-step were fine enough that the results are insensitive to further refinement [Scandella, 2010].

Numerical modeling of hydrate formation and methane gas transport through dynamic conduits

Introduction

The dissociation of methane hydrates in shallow ocean sediments has long been suggested as a potential feedback to climate change [Dickens et al., 1995; Judd et al., 2002; Archer et al., 2009]. One of the primary modes of methane export from submerged sediments is free-gas ebullition, but gas bubbles dissolve during rise, exposing the methane to oxidation to the less potent greenhouse gas CO_2 [Valentine et al., 2001]. The ability of rising bubbles to transport methane to the atmosphere depends on the release depth, bubble density and size distribution [Leitch and Baines, 1989; Greinert and Nutzel, 2004; Leifer et al., 2006; McGinnis et al., 2006; Gong et al., 2009]. Thus, the atmospheric release depends not only on how much hydrate dissociates but how it is released from the sediments.

Focused ebullition has been observed at Hydrate Ridge, especially in a periodic pattern during low tides [Torres et al., 2002]. The gas is likely supplied from a deep geologic reservoir, but the mechanism that allows it to travel through the Hydrate Stability Zone (HSZ) from near the base of the HSZ (BHSZ) and to escape only during low tides has yet to be determined. Multiple mechanisms have been proposed for coexistence of free gas and hydrates in the HSZ [Milkov and Xu, 2005; Torres et al., 2005; Ruppel et al., 2005]: (1) regional geotherms, (2) reduction in hydrate stability by salt accumulation, (3) kinetics of hydrate formation, and (4) fast, focused flow of free gas through high-permeability conduits. Evidence of fractures and flow through them at Hydrate Ridge has been inferred from field observations [Torres et al., 2002; Flemings et al., 2003; Trehu et al., 2004a; Weinberger and Brown, 2006] and modeling studies [Liu and Flemings, 2007; Daigle and Dugan, 2010].

The combined observations of tidally-controlled ebullition with evidence of gas flow through conduits gives us an opportunity to investigate the mechanisms controlling gas migration through the hydrate stability zone. Previous modeling work has sought to estimate the distribution of hydrates by considering methane transport in the dissolved phase only [Xu and Ruppel, 1999; Buffett and Archer, 2004; Daigle and Dugan, 2010] or as gas flowing by capillary invasion [Liu and Flemings, 2007; Garg et al., 2008; Reagan and Moridis, 2009; Daigle and Dugan, 2010]. These models capture slow processes of pore water flow, heat and salt transport to capture important impacts on hydrate stability and the equilibrium distribution of hydrates [Kowalsky and Moridis, 2007]. Other models have been used to estimate the hydrate response to slow sea level change [Liu and Flemings, 2009] and the onset time for fracturing [Liu and Flemings, 2007; Daigle and Dugan, 2010].

In contrast, we model fast processes of free-gas flow through fractures, tidal variations, and kinetic hydrate formation. Previous modeling of gas release from hydrate-free lake sediments has shown that conduit flow can reproduce the observed, hydrostatically-forced episodicity of gas venting [Scandella et al., 2011], and we hypothesize that a similar mechanism controls tidally-forced venting from hydrate-bearing sediments. Here, we develop a numerical model of this mechanism and show that it can indeed reproduce the tidally-dependent ebullition record observed at Hydrate Ridge. In addition, we find that within a tidal low the ebullition will manifest as distinct bursts that arise from a geyser-like instability. The ability of gas to traverse the HSZ depends on the vertical

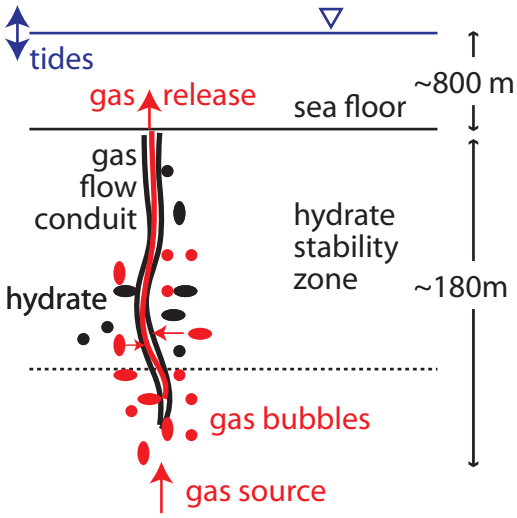

Figure 105: Conceptual model of gas flowing through the hydrate stability zone by dilating near-vertical conduits. These conduits access gas in a small domain of surrounding porous media, especially through conductive horizontal strata [Weinberger and Brown, 2006], and transport the gas vertically. Vertical dimensions reflect the south summit of Hydrate Ridge, where tidally-forced ebullition has been observed [Torres et al., 2002].

gas conductivity and kinetic hydrate formation rate.

Theory, Formulation and Methods

Model domain

We investigate the dynamics of gas flow through the hydrate stability zone with a one-dimensional, continuum-scale numerical model. The model attempts to capture the aggregate behavior of sediments fractured periodically in space. Because the model is 1D, the transport and accumulation reflect the vertical flow through the fractures as well as the fluid exchange between the fracture and the sediment matrix.

The model is intended to resolve the release of methane at sub-tidal timescales (minutes to hours). At this timescale, fast transport mechanisms such as gas-phase flow are expected to dominate pore-fluid solute advection and diffusion. Thus, we neglect the accumulation and transport of dissolved methane, salt, and heat, with hydrate formation and aqueous flow. These mechanisms control the hydrate distribution by changing the local hydrate stability conditions [Bhatnagar et al., 2007; Liu and Flemings, 2007; Garg et al., 2008; Liu and Flemings, 2009; Daigle and Dugan, 2010] and thus the long-term hydrate distribution. In turn, hydrate formation can influence the transport regime by cementing the grains [Waite et al., 2009; Klar et al., 2010] or clogging the pores [Nimblett and Ruppel, 2003; Liu and Flemings, 2007; Daigle and Dugan, 2010]. We neglect these slow feedback mechanism to develop a simple continuum model of fast gas flow through conduits that respond to both internal pressurization and a tidal forcing.

Poromechanics

Gas behaves differently in fine-grained sediments, such as the clay-dominated sediments found in the HSZ at Hydrate Ridge [Trehu et al., 2004a], compared with coarse-grained sediments. Gas invades large-grained porous media when the capillary pressure ($P_g - P_w$) becomes large enough for the curved interface to squeeze through a pore throat. In fine-grained sediments, gas invades by deforming the grains because the capillary pressure required to squeeze through the throats is prohibitively large [Jain and Juanes, 2009]. Instead of small interstitial bubbles characteristic of a capillary-controlled system, gas bubbles in fine sediments take the form relatively large gas cavities surrounded by a matrix of water and sediment grains [Sills et al., 1991]. Because these bubbles grow in a highly-eccentric, cornflake-shaped fracture pattern [Boudreau et al., 2005; Algar and Boudreau, 2010], rather than as spherical bubbles, this mode of growth may also allow for vertical mobility.

The effective stress, σ', controlling the deformation of this continuum around the gas cavities may then be approximated as,

$$\sigma' = \sigma_h - P_g, \tag{54}$$

where σ_h is the horizontal stress and P_g is the gas pressure [Scandella et al., 2011]. This contrasts with the typical form of the effective stress, in which the fluid pressure of concern is the water pressure [Terzaghi, 1943; Daigle and Dugan, 2010] or when both fluid pressures are considered [Bishop, 1959; Klar et al., 2010]. Equation 54 is consistent with the view that sediment and water form a coherent "mud" phase against which large gas bubbles must push to expand.

The deformation of this matrix-water continuum may be treated as a plastic process that occurs at yield limits in tension (σ_T) and compression (σ_C):

$$-\sigma_T \leq \sigma' \leq \sigma_C. \tag{55}$$

Cavities dilate in tension ($\sigma' = -\sigma_T$), reducing the gas pressure sufficiently to maintain the plastic equilibrium defined in Equation 55. In compression ($\sigma' = \sigma_C$), the cavities shrink and the gas pressure rises in step with the horizontal stress. This mechanism of cavity deformation is used to attribute accumulation of gas mass to changes in pressure and volume, in the following order as necessary:

1. Generate maximum gas pressure change at current volume, up to a plastic yield limit

$$\Delta P_g^{max} = \frac{\Delta M_g RT}{S_g \phi m_{CH_4}}. \tag{56}$$

2. If a yield limit is reached, deform cavities to change volume. Vary saturation at the new fixed gas pressure, according to the ideal gas law, up to a maximum that satisfies the volume constraints $S_g + S_h \leq 1$ and $S_g \geq S_g^{min}$.

3. If a volume constraint is reached, allow pressure to rise or fall outside the plastic limits ($\sigma_h - \sigma_C \leq P_g \leq \sigma_h + \sigma_T$) at the new fixed saturation according to the ideal gas law.

Thus, gas accumulation first forces the gas pressure to a yield limit before changing the gas saturation. This allows for compressible gas flow but requires a small time step to resolve frequent pressure changes.

In all simulations here we assume $\sigma_C = 0$ and $\sigma_T = 0.3$ MPa, consistent with estimates from combined modeling and field observations at South Hydrate Ridge [Weinberger and Brown, 2006]. The gas pressure may exceed the plastic yield limits, especially when hydrate formation depletes the gas to a minimum saturation (for stability) $S_g^{min} = 0.005$. However, this does not occur in any of the simulations shown here.

Gas flow through conduits

The core of our model is free-gas flow through dynamic, vertical conduits. These conduits dilate at the tensile plastic yield limit and close at the compressive limit (Figure 106). In addition to the dependence on effective stress, we impose a minimum gas saturation, $S_g^{conduit} = 0.1$, which is required for the conduits to connect across depth intervals [Weinberger and Brown, 2006]. Similar model behavior is obtained when $S_g^{conduit} = 0$, except the low gas saturations exacerbate the gas pressure fluctuations during cavity deformation (Equation 56), and resolving these larger pressure swings requires a smaller time step.

The model captures gas flow through fractured porous media without distinguishing the pools of gas in the conduit and porous medium separately. Instead, the effect of dilation is captured by increasing the vertical intrinsic permeability, k, from 0 to a parameterized permeability of the conduit-matrix continuum, $k_{conduit}$, which accounts for both the dimensions and lateral spacing of conduits. The gas mass conservation equation uses a multiphase extended form of Darcy's law for the gas flux [Muskat, 1949]:

$$\partial_t(\phi\rho_g S_g) = -\partial_z F_g + Q_g^h \tag{57}$$

$$F_g = -\rho_g \frac{k k_{rg}}{\mu_g}\left(\partial_z P_g - \rho_g g\right) \tag{58}$$

$$k_{rg} = S_g \tag{59}$$

where Q_g^h is the rate of gas mass generation from hydrate per unit volume and constitutes all the gas loss from hydrate dissociation, Q_h:

$$Q_g^h = -\chi_h^{CH_4} Q_h \tag{60}$$

The model is initially free of hydrate but includes gas saturations equal to the minimum for conduit opening, $S_g^{conduit}$, in order to eliminate the initial time necessary to accumulate this minimum saturation. The gas pressure, however, is assumed to begin at the compressive yield limit so that the conduit is initially closed everywhere. At the top boundary the gas pressure equals the tidally-forced hydrostatic pressure, with $S_g = 0$, and the gas flux in the bottom is set by the parameter F_g^{source}, which represents the source supplied through Horizon A at the BHSZ [Trehu et al., 2004a; Weinberger and Brown, 2006].

Hydrate formation and dissociation

Given the high temporal resolution of the model (seconds to minutes), a kinetic model of hydrate formation was adopted following [Kim et al., 1987]. The model for microscale hydrate formation is driven by the departure from equilibrium fugacity, and we simplify this by considering the nearly-equivalent departure from equilibrium pressure [Duan et al., 1992]. We also adopt the same

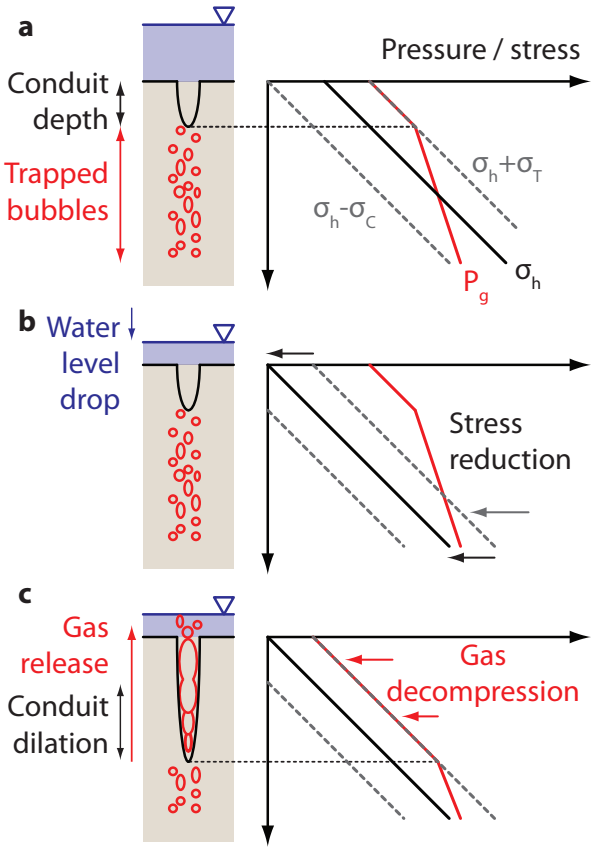

Figure 106: Model response to water level drop. (a) Initial condition: the cartoon at left shows the water level (blue) above a sediment column with gas bubbles trapped below the open conduit (not to scale in vertical). The conduit opens when the effective stress, $\sigma' = \sigma_h - P_g$, falls to its tensile yield limit, $-\sigma_T$. The stress and pressure profiles at right show that this occurs when P_g (red solid line) equals $\sigma_h + \sigma_T$ (gray dashed line). (b) A drop in hydrostatic load reduces σ_h throughout the sediment column. (c) Plastic cavity dilation allows shallow gas bubbles to decompress to $\sigma + \sigma_T$. The conduit opens from the deepest location where $\sigma' = -\sigma_T$ and releases the formerly trapped bubbles. In the case of a hydrostatic load increase (not shown), the stress rises, and the cavity compression mechanism pressurizes gas bubbles to enforce $\sigma' \leq \sigma_C$, or equivalently $P_g \geq \sigma_h - \sigma_C$. On open conduit remains open until this compressive limit is reached. Modified from [Scandella et al., 2011].

temperature dependence but neglect the dependence on surface area of hydrate [Kim et al., 1987]. The rate of hydrate mass generation per bulk volume is:

$$Q_h = K_h(P_g - P_{eq}) \exp(-\frac{E}{RT}), \tag{61}$$

where K_h is a rate constant with units of kg/m^3/Pa/s, $E = 8.1 \times 10^4$ J/mol is the activation energy of the reaction, $R = 8.314$ J/mol/K is the gas constant. This model transfers mass of CH_4 from the gas to hydrate phases when $P_g > P_{eq}$, in the hydrate stability zone, and it transfers mass in the other direction when $P_g < P_{eq}$, generally below the hydrate stability zone. The equilibrium pressure is evaluated as the hydrate-gas phase boundary, P_{eq}[kPa] $= \exp(40.234 - 8860/T$[K]) [Kwon et al., 2006], for a temperature profile from a seafloor temperature of 277 K and constant geothermal gradient of 0.053 K/m at Hydrate Ridge [Daigle and Dugan, 2010]. This causes hydrate to form slightly below the traditional BHSZ, defined as $P_w = P_{eq}$, because $P_g \geq P_w$ when free gas is present. Whenever either phase is depleted or when the sum of gas and hydrate saturations exceeds 1, the rate of transfer is reduced to avoid unphysical mass transfer.

Tidal forcing

Impact on vertical stress. A central goal of our model is to capture the observed relationship between tides and ebullition from hydrate-bearing sediments [Torres et al., 2002], and the link is made through the impact of hydrostatic pressure on total and effective stresses. The total vertical (lithostatic) stress, σ_v, is the sum of the hydrostatic pressure at the sea floor and the integrated bulk density:

$$\sigma_v(z,t) = P_h(t) + \int_0^z \rho_b(z')g dz' \tag{62}$$

$$P_h(t) = \rho_w g \left(D + z_{tide} * \sin\left(\frac{2\pi t}{t_{tide}}\right)\right), \tag{63}$$

where ρ_b is the bulk density, P_h is the hydrostatic pressure at the seafloor, z_{tide} and t_{tide} are the tidal amplitude and period, respectively. These equations simply show that tidal variations reflect the total vertical stress throughout the HSZ.

Lateral and vertical stresses. The total vertical stress varies with tides as shown above, but near-vertical conduits should in the direction where the gas opposes the minimum stress, which is generally horizontal near the crest of south Hydrate Ridge [Weinberger and Brown, 2006]. We calculate the horizontal stress that would be imposed on the model domain by the surrounding, water-saturated sediments. The vertical and lateral stresses are connected through the water-saturated effective stresses by the lateral stress coefficient, K_0. In water-saturated rock and soil, K_0 may be expressed as

$$K_0 = \frac{\sigma'_{hw}}{\sigma'_{vw}} = \frac{\nu}{1-\nu}, \tag{64}$$

where $\sigma'_{hw} = \sigma_h - P_w$ and $\sigma'_{vw} = \sigma_v - P_w$ are the water-saturated effective stresses, and ν is Poisson's ratio [Wang, 2000]. We adopt $\nu = 3/7 \rightarrow K_0 = 0.75$ and for our system [Thomas,

1987]. Estimating the horizontal stress from the vertical stress requires both the lateral stress coefficient and water pressure:

$$\sigma_h = \sigma'_{hw} + P_w = K_0\sigma_v + (1 - K_0)P_w \tag{65}$$

The water pressure response on short timescales and deep in sediments is undrained, where the fluid pressurization with laterally-uniform variations in vertical stress is determined by the loading efficiency, $\lambda = \partial P_w/\partial\sigma_v$ [Wang, 2000]. For the water-saturated sediments surrounding the model domain, we assume $\lambda = 1$ [Liu and Flemings, 2009], and therefore that the water pressure changes synchronously and in the same amount as vertical stress.

Combined model

During each time step, the mechanisms are applied in a staggered manner:

1. Impose hydrostatic forcing.
2. Determine where conduits open and close to impose permeability profile.
3. Flow gas through the open conduits.
4. Exchange mass between gas and hydrate phases.
5. Deform cavities, altering P_g and S_g, to plastic equilibrium in response to the hydrostatic forcing and the mass accumulation combined from flow and phase transfer.

Results

Episodicity of gas release at the seafloor

We perform a base-case scenario designed to reproduce the general pattern of ebullition during tidal lows for conditions observed at the southern summit of Hydrate Ridge [Torres et al., 2002]. The parameter values used for this base scenario are $D = 800$ m, $H = 180$ m, $z_{tide} = 1$ m, $t_{tide} = 12$ hours, $k_{conduit} = 2 \times 10^{-14}$ m^2, $K_h = 100$ kg/m^3/Pa/s, $F_g^{source} = 10^{-4}$ kg/m^2/s, $\sigma_T = 0.3 \times 10^6$ Pa, and $S_g^{conduit} = 0.1$. Under these conditions gas indeed traverses the HSZ and escapes during falling tides (Figure 107).

The time for gas to traverse the HSZ may be estimated using the multiphase Darcy flux (Equation 58):

$$t_{flow} \sim \frac{z_{BHSZ}\mu_g\phi}{k_{conduit}\rho_b g}, \tag{66}$$

where the characteristic gas pressure gradient has been approximated by a characteristic value relative to the lithostatic gradient, $\rho_b g$. The model predicts that gas typically accumulates beneath the sediment surface until the hydrostatic pressure falls with tides (Figure 108) and the tensile plastic deformation at the surface allows gas to escape into the water column. After an initial peak in gas flux, the ebullition continues at a moderate rate until the near-surface gas is depleted or the tides begin to rise again and cause the conduits to close (Figure 107).

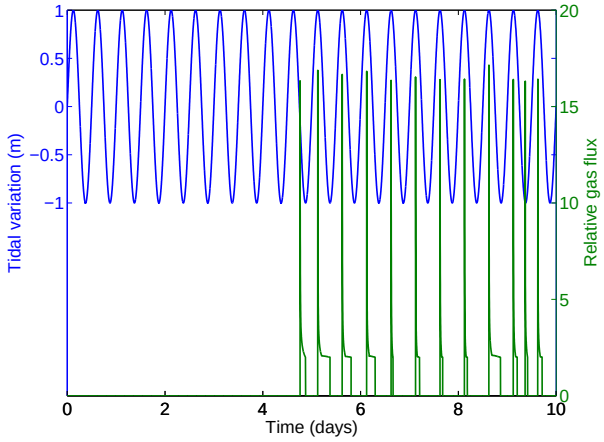

Figure 107: Periodic venting of gas (green, right scale) at the seafloor in response to 1 m tidal signal (blue, left scale). Gas flux is normalized by the input flux at the bottom of the model, F_g^{source}. The delay before the initial release reflects the timescale for gas to build up pressure and traverse the HSZ. The strong peak leading each release reflects a buildup of pressure just below the seafloor that is released during plastic tensile opening of the gas flow conduit at the surface, after which the gas pressure drive is reduced. Gas vents only during falling tides.

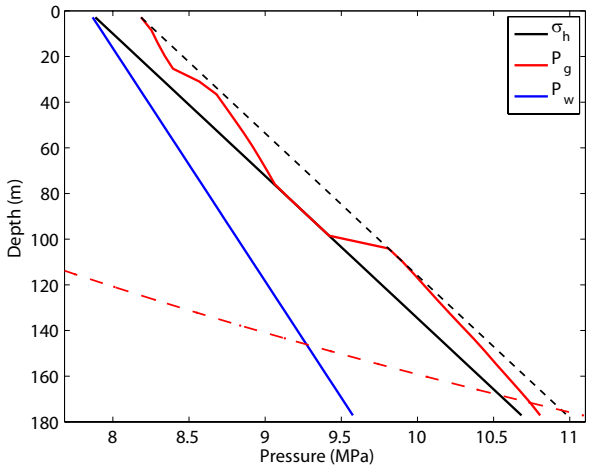

Figure 108: Profile of pressures and stresses at the end of the base simulation. The horizontal stress, gas and water pressures appear as solid lines of black, red and blue, respectively. The tensile limit on gas pressure, $\sigma_h + \sigma_T$, is shown as a dotted black line, and the equilibrium gas pressure, P_{eq} is a red dashed curve. The region from $0 - 80$ mbsf is a connected gas plume where the conduit remains open because $P_g > \sigma_h - \sigma_C$. This plume is separated from the other rising plume, from $100 - 180$ mbsf, by a region where the gas pressure has fallen to the compressive yield limit and the conduit has closed.

Timescales of flow through dynamic conduits. Even without a tidal forcing or hydrate formation, compressible gas flow through a system of dynamic conduits displays two primary time scales at steady state: the release time for a connected gas plume, and the duration of an individual ebullition event. Each rising gas plume, displayed as a region of gas pressure elevated above the horizontal stress and the conduit remains open (Figure 108), may reach the sediment surface and escape over a time period on the order of 1 day (Figure 109, top). This release time scales as

$$t_{plume} \sim t_{flow} \frac{h_{plume}}{z_{BHSZ}}, \tag{67}$$

where h_{plume} is the height of a rising gas plume. This height depends on the ratio of gas influx from below (F_g^{source}) and the vertical conductivity and may be estimated as

$$h_{plume} \sim t_{flow} \frac{F_g^{source}}{M_g^0}, \tag{68}$$

where M_g^0 is the initial mass of gas per unit bulk volume. This equation yields an estimate of ~ 130 m for the base simulation and agrees well with the observed heights of ~ 100 m in Figure 108.

However, a plume is not necessarily released in a continuous event. The release of methane gas from the top of the sediment column locally reduces the gas pressure and can close the conduit before the underlying gas plume is depleted. This geyser-like instability releases a rising gas plume as multiple separate ebullition events (Figure 109, bottom).

Interaction of flow with tides and hydrates. The inherent episodicity of gas release through conduits is complicated by the influence of tides and hydrate formation. The relatively slow release of a connected plume may be broken up into individual releases as falling tides facilitate conduit opening by reducing the hydrostatic load and total stress (Equation 62 and Figure 110, top). The release during a single cycle may then be further divided by the geyser instability (Figure 110, bottom).

Hydrate formation simultaneously reduces the gas pressure and closes the conduits more quickly, which delays the arrival at the surface, reduces the total output of gas, and changes the fine-scale episodicity of gas release (Figure 111).

Gas survival through the HSZ

The amount of methane that traverses the HSZ depends on the relative rates of gas flow and conversion to hydrate. The time required for gas to traverse the HSZ is estimated from Equation 66, although the flow timescale itself depends on the rate of hydrate formation because hydrate formation tends to close the conduits or prevent their opening by reducing the gas pressure. The flow timescale should be compared with the timescale for hydrate formation, which may be estimated from Equation 61 as the time required to consume the initial gas at its initial pressure:

$$t_{hydrate} \approx \frac{M_g^0 / \chi_{CH_4}^h}{K_h (P_g - P_{eq}) \exp(-E/(RT))}, \tag{69}$$

where $\chi_{CH_4}^h$ is the mass fraction of methane in hydrates. Because the initial pressure and temperature profiles are not spatially uniform, $t_{hydrate}$ is estimated as the average over all depth intervals.

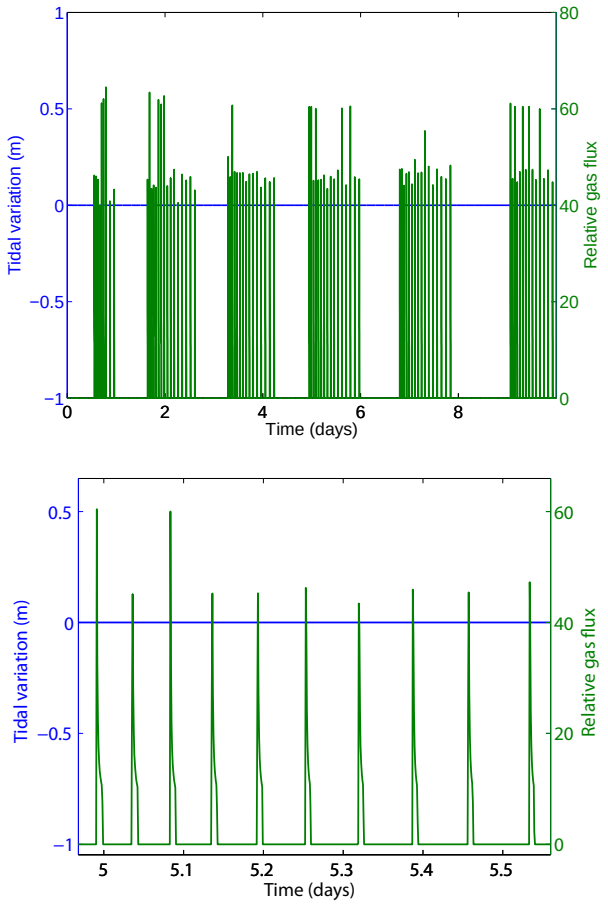

Figure 109: Time series showing an internally-driven run with no tidal forcing. The top figure shows two timescales relevant to the release: a longer timescale created by the rise of connected gas plumes, which vent for and are separated by about a day, and a shorter timescale of discrete ebullition events. The zoomed bottom figure shows that these releases are separated by about $1/20$ day.

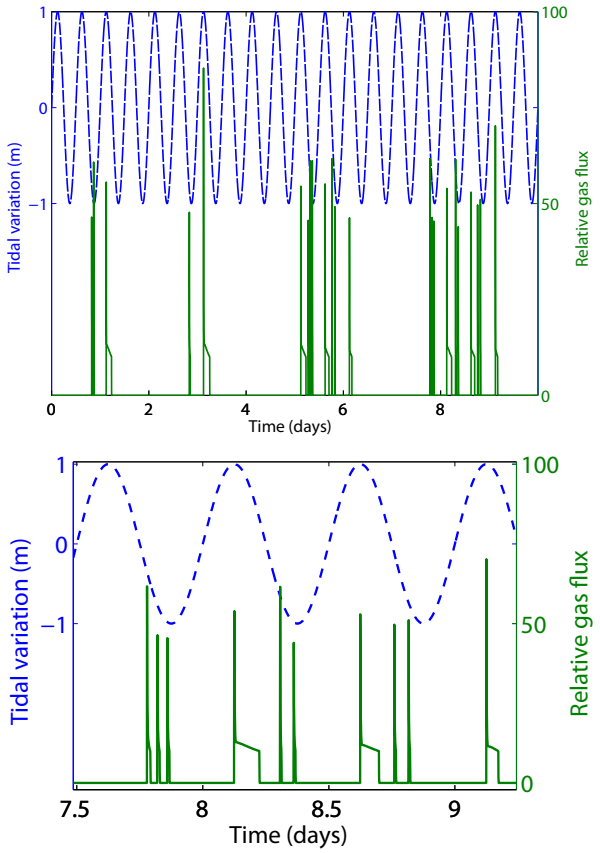

Figure 110: Impact of combined internal and external forcings on gas flow without hydrate formation. Top: time series showing the long timescale of plume release of $\sim$ 2 days (days 1,3, 5, and 8) along with other effects within each plume release. Bottom: zoom of the top figure shows that, within a given plume release, the individual ebullition events occur only during falling tides and display different geyser-driven episodicity depending on the pressure and saturation conditions in the near-surface sediments.

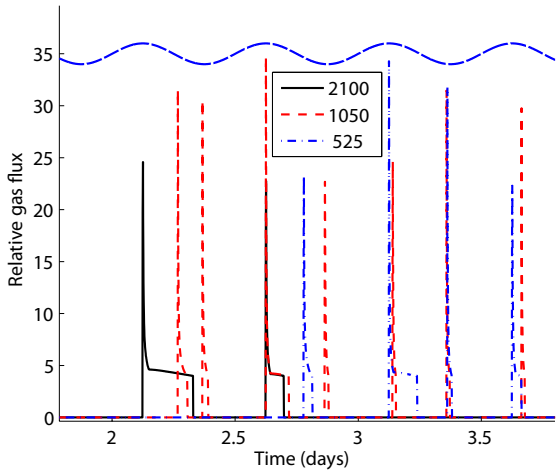

Figure 111: Sensitivity of venting timeseries to rate of hydrate formation. In all cases, $k_{conduit} = 5 \times 10^{-14}$ m^2, $z_{tide} = 1$ m (blue dashed sinusoid centered on 35 on the vertical axis), and K_h is varied to control the ratio $t_{hydrate}/t_{flow}$, shown in the legend. Smaller values of $t_{hydrate}/t_{flow}$ relate to faster hydrate conversion and both delay the first ebullition event and reduce the total gas vented to the ocean and (see Figure 112).

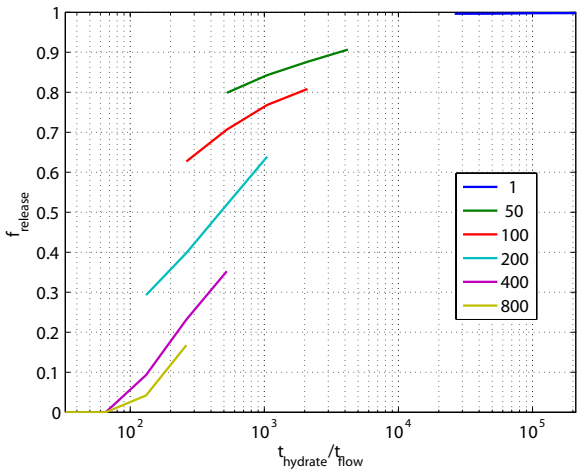

Figure 112: Sensitivity of gas release to rates of gas flow and hydrate formation. The fraction of gas that escapes without conversion to hydrate, $f_{release}$, increases as the timescale of hydrate formation increases relative to the timescale of flow. The timescale ratio $t_{hydrate}/t_{flow}$ was varied using both $k_{conduit}$ and K_h. The legend shows particular values of K_h, and the discontinuities show that the release fraction is somewhat dependent on $t_{hydrate}$ independently of $t_{hydrate}/t_{flow}$.

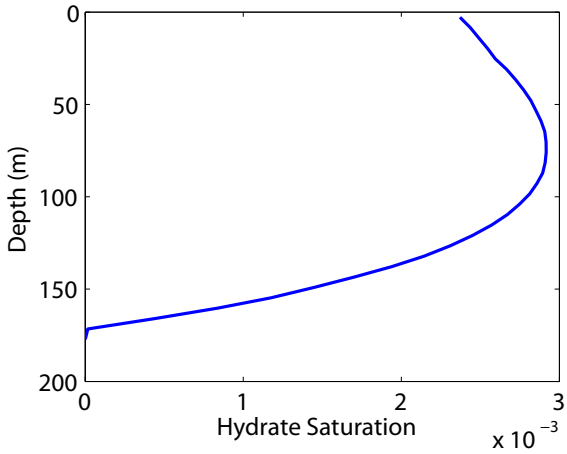

Figure 113: Final hydrate saturation profile for the same conditions as in Figure 107 after 10 days.

We quantify the fraction of methane flowing through the model that reaches the ocean by tracking these fluxes over the course of a given simulation. If the time period is long enough to reach pseudo-steady state conditions, changes in the methane storage become small relative to the cumulative fluxes into and out of the system. In this case, the ability of methane to escape to the sediment surface may be estimated as the ratio of time-integrated fluxes across the top and bottom of the model. However, the poorly-constrained initial gas content of the system motivates us to account for the change in *gas* storage over the time period:

$$\Delta M_g = \int_0^H \left(M_g(z, t_f) - M_g(z, t = 0) \right) dz \tag{70}$$

$$f_{release} \approx \frac{\int_0^{t_f} F(z = 0, t) dt}{\int_0^{t_f} F(z = H, t) dt - \Delta M_g}, \tag{71}$$

where $M_g = \rho_g S_g \phi$ is the mass of accumulated gas per volume. This release fraction is highly sensitive to the ratio of flow and hydrate timescales, and it also depends on the hydrate generation rate (Figure 112).

Vertical hydrate distribution

Hydrate formation increases the saturation of hydrate, but the assumed formation rates are slow and cause little to appear during the course of simulations here. A profile of hydrate saturation shows this growth throughout the HSZ (Figure 113). The distribution reflects the balance of the driving force, $P_g - P_{eq}$, which increases upwards (Figure 108), against the temperature-dependent term, which increases about threefold downward from the water column to the BHSZ. Hydrate may form or dissociate based on Equation 61, but because the HSZ is always populated with gas for these simulations, $P_g \geq P_{eq}$ in this region and hydrate only forms and never dissociates.

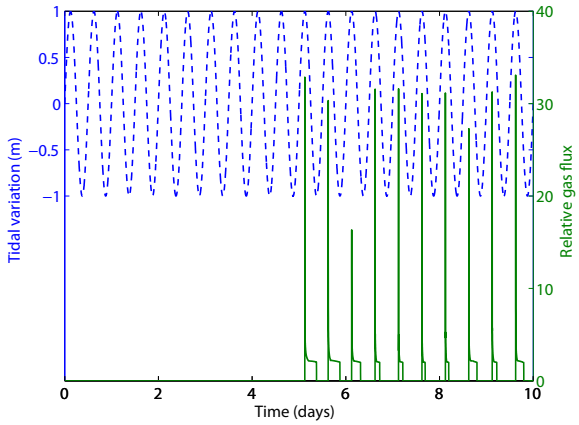

Figure 114: Spatial discretization sensitivity with $nz = 64$ and $dz = 2.8$ m, compared with $nz = 32$ and $dz = 5.6$ m in Figure 107. Increasing the spatial discretization causes the initial peaks in gas release to be larger due to the stronger gas pressure gradient between the top cell and seafloor. In both these cases, the finite volume interface permeabilities were estimated from the cell values using a moving average filter with enough cells to cover a width of 10 m.

Numerical techniques

The flow Equations (57–59) are discretized in space using a finite volume method with first-order upwinding and integrated in time using a forward Euler scheme. The model is sensitive to the spatial discretization because of the nonlinear relationship between permeability and effective stress through conduit dilation. This means that the gas pressure gradients which build up at the top of the sediment column are larger for finer discretization, and hence the driving force for gas flow is stronger and the initial peak in ebullition is larger (compare Figures 107 and 114).

The model timestep is chosen dynamically to keep the magnitude of gas pressure changes from flow and hydrate formation small compared with the sediment strength. This condition is strict enough that the results do not change when a smaller timestep is imposed.

Discussion and Conclusions

The model developed here shows that free gas flow through dynamic conduits is a potential mechanism by which tides trigger ebullition from hydrate-bearing sediments at South Hydrate Ridge [Torres et al., 2002] (Figure 107). Although the model neglects spatial heterogeneity and processes that control the long-term dynamics of hydrate-bearing sediments, its ability to balance free-gas flow through dynamic conduits against conversion to hydrates allows us to identify emergent behavior and the relevant temporal and spatial scales that may control venting at the seafloor. For example, the tidal forcing imposes gas-flux periodicity on the release of connected gas plumes that rise through the HSZ, and within a tidal ebb the release may break into multiple bursts as the flow conduit opens and closes near the surface, in a mechanism reminiscent of fluid expulsion from a geyser.

This fraction of injected gas that escapes conversion to hydrate is sensitive to the timescales of fluid flow and hyrdate formation. More gas escapes conversion to hydrate when the ratio

$t_{hydrate}/t_{flow}$ is larger, but even at a given value of this ratio, faster hydrate formation causes less gas to survive the rise (Figure 112). We suggest the explanation that gas rises more slowly as the hydrate formation rate increases because hydrate formation reduces the gas pressure and delays conduit opening. As the time for gas to rise increases, a corrected ratio $t_{hydrate}/t_{flow}$ would be smaller, and the lines might coincide better in Figure 112.

A number of neglected mechanisms impact the efficiency of gas transport and hydrate formation assumed by our model. The transport and accumulation of heat and dissolved methane and salt all tend to inhibit gas flow and hydrate formation and dissociation. Gas and hydrate are only stable when surrounded by methane- saturated pore water, and background aqueous flow flushes away concentrated methane, dissolving gas and hydrates. Our model overestimates the efficiencies of both vertical gas transport and mass transfer from gas to hydrate phases. Meanwhile, salt expulsion from pore water and heat generation during hydrate formation reduce hydrate stability, providing negative feedbacks on hydrate generation.

Given that neither gas flow nor hydrate formation in our model depends on the presence of hydrates, the current model is not an ideal tool for speculating on the impact of gas flow on the vertical hydrate distribution. Future models may be made sensitive to hydrates by considering increased tensile strength [Waite et al., 2009; Klar et al., 2010] or pore clogging [Nimblett and Ruppel, 2003; Liu and Flemings, 2007; Daigle and Dugan, 2010] with hydrate formation, as well as a dependence of the hydrate formation rate on the available hydrate surface area [Kim et al., 1987]. Such models may test the stability of hydrate distributions suggested by models that capture long-timescale effects in the presence gas flow through fractures.

References for Fracturing Dominated Behavior

E. Aker, K. J. Måløy, and A. Hansen. Simulating temporal evolution of pressure in two-phase flow in porous media. *Phys. Rev. E*, 58(2):2217–2226, 1998.

C. K. Algar and B. P. Boudreau. Stability of bubbles in a linear elastic medium: Implications for bubble growth in marine sediments. *J. Geophys. Res.*, 115:F03012, 2010.

A. L. Anderson, F. Abegg, J. A. Hawkins, M. E. Duncan, and A. P. Lyons. Bubble populations and acoustic interaction with the gassy floor of Eckernförde Bay. *Cont. Shelf Res.*, 18:1807–1838, 1998.

A. L. Anderson and L. D. Hampton. Acoustics of gas-bearing sediments. 1. Background. *J. Acoust. Soc. Am.*, 67(6):1865–1889, 1980.

T. L. Anderson. *Fracture Mechanics: Fundamentals and Applications*. CRC Press, Boca Raton, Florida, 1991.

D. Archer, B. Buffett, and V. Brovkin. Ocean methane hydrates as a slow tipping point in the global carbon cycle. *Proc. Natl. Acad. Sci. U.S.A.*, 106(49):20596–20601, 2009.

D. Bastviken, L. J. Tranvik, J. A. Downing, P. M. Crill, and A. Enrich-Prast. Freshwater methane emissions offset the continental carbon sink. *Science*, 331(6013):50, 2011.

J. Behseresht, Y. Peng, M. Prodanovic, S. L. Bryant, A. K. Jain, and R. Juanes. Mechanisms by which methane gas and methane hydrate coexist in ocean sediments. In *Offshore Technology Conference*, Houston, TX, May 5–8, 2008. (OTC 19332).

A. I. Best, M. D. Richardson, B. P. Boudreau, A. G. Judd, I. Leifer, A. P. Lyons, C. S. Martens, D. L. Orange, and S. J. Wheeler. Shallow seabed methane gas could pose coastal hazard. *Eos Trans.* AGU, 87(22):213,217, May 2006.

G. Bhatnagar, W. G. Chapman., G. R. Dickens, B. Dugan, and G. J. Hirasaki. Generalization of gas hydrate distribution and saturation in marine sediments by scaling of thermodynamic and transport processes. *Am. J. Sci.*, 307(6):861–900, 2007.

M. A. Biot. General theory of three-dimensional consolidation. *J. Appl. Phys.*, 12(155–164), 1941.

R. B. Bird, W. E. Stewart, and E. N. Lightfoot. *Transport Phenomena*. John Wiley and Sons, New York, 1960.

A. W. Bishop. The principle of effective stress. *Teknisk Ukeblad*, 39:859–863, 1959.

M. Blunt and P. King. Macroscopic parameters from simulations of pore scale flow. *Phys. Rev. A*, 42(8):4780–4787, 1990.

R. Boswell. Is gas hydrate energy within reach? *Science*, 325(5943):957–958, 2009.

B. P. Boudreau, C. Algar, B. D. Johnson, I. Croudace, A. Reed, Y. Furukawa, K. M. Dorgan, P. A. Jumars, and A. S. Grader. Bubble growth and rise in soft sediments. *Geology*, 33(6):517–520, doi:10.1130/G21259.1, 2005.

M. S. Bruno. Micromechanics of stress-induced permeability anisotropy and damage in sedimentary rocks. *Mech. Mater.*, 18:31–48, 1994.

M. S. Bruno and R. B. Nelson. Microstructural analysis of the inelastic behavior of sedimentary rock. *Mech. Mater.*, 12(2):95–118, 1991.

B. Buffett and D. Archer. Global inventory of methane clathrate: sensitivity to changes in the deep ocean. *Earth Planet. Sci. Lett.*, 227:185–199, 2004.

J.-D. Chen and D. Wilkinson. Pore-scale viscous fingering in porous media. *Phys. Rev. Lett.*, 55 (18):1892–1895, 1985.

X. Cheng, L. Xu, A. Patterson, H. M. Jaeger, and S. R. Nagel. Towards the zero-surface-tension limit in granular fingering instability. *Nature Phys.*, 4(3):234–237, 2008.

C. Chevalier, A. Lindner, M. Leroux, and E. Clement. The instability of slow, immiscible, viscous liquid-liquid displacements in permeable media. *J. Non-Newton. Fluid.*, 158:63–72, 2009.

G. C. Cho and J. C. Santamarina. Unsaturated particulate materials—Particle-level studies. *J. Geotech. Geoenviron. Eng.*, 127(1):84–96, 2001.

J.-H. Choi, Y. Seol, R. Boswell, and R. Juanes. X-ray computed-tomography imaging of gas migration in water-saturated sediments: from capillary invasion to conduit opening. *Geophys. Res. Lett.*, 38:L17310, doi:10.1029/2011GL048513, 2011.

M. Clark and P. R. Bishnoi. Determination of activation energy and intrinsic rate constant of methane gas hydrate decomposition. *Can. J. Chem. Eng.*, 79(1):143–147, doi=10.1002/cjce.5450790122, 2001.

T. Collett, M. Riedel, J. Cochran, R. Boswell, J. Presley, P. Kumar, A. Sathe, A. Sethi, M. Lall, V. Sibal, and the NGHP Expedition 01 Scientists, editors. *Indian National Gas Hydrate Program Expedition 01 Initial Reports*, New Delhi, India, 2008. Indian Directorate General of Hydrocarbons.

B. K. Cook, D. R. Noble, and J. R. Williams. A direct simulation method for particle-fluid systems. *Eng. Comput.*, 21(2–4):151–168, 2004.

O. Coussy. *Mechanics of Porous Media*. John Wiley & Sons, Chichester, England, 1995. Originally published in French as *Mécanique des Milieux Poreux*, Editions Technip, 1991.

J. Crank. *Mathematics of Diffusion*. Oxford University Press, second edition, 1975. (First edition, 1956).

P. M. Crill, K. B. Bartlett, J. O. Wilson, D. I. Sebacher, R. C. Harriss, J. M. Melack, S. Macintyre, L. Lesack, and L. Smithmorrill. Tropospheric methane from an Amazonian floodplane lake. *J. Geophys. Res.*, 93(D2):1564–1570, 1988.

P. A. Cundall and O. D. L. Strack. Discrete numerical model for granular assemblies. *Geotechnique*, 29:47–65, 1979.

H. Daigle and B. Dugan. Origin and evolution of fracture-hosted methane hydrate deposits. *J. Geophys. Res.*, 115:B11103, doi:10.1029/2010JB007492, 2010.

P. G. de Gennes. Wetting: statics and dynamics. *Rev. Mod. Phys.*, 57:827–863, 1985.

T. Delsontro, D. F. McGinnis, S. Sobek, I. Ostrovsky, and B. Wehrli. Extreme methane emissions from a Swiss hydropower reservoir: Contribution from bubbling sediments. *Environ. Sci. Technol.*, 44(7):2419–2425, 2010.

G. R. Dickens. Rethinking the global carbon cycle with a large, dynamic and microbially mediated gas hydrate capacitor. *Earth Planet. Sci. Lett.*, 213:169–183, 2003.

G. R. Dickens, J. R. O'Neil, D. K. Rea, and R. M. Owen. Dissociation of oceanic methane hydrate as a cause of the carbon isotope excursion at the end of the Paleocene. *Paleoceanography*, 10 (6):965–971, 1995.

G. R. Dickens, C. K. Paull, and P. Wallace. Direct measurement of in situ methane quantities in a large gas-hydrate reservoir. *Nature*, 385:426–428, 1997.

Z. H. Duan, N. Møller, and J. H. Weare. An equation of state for the CH_4-CO_2-H_2O system: I. Pure systems from 0 to 1000°C and 0 to 8000 bar. *Geochim. Cosmochim. Acta*, 56(7):2605–2617, 1992.

E. J. Fechner-Levy and H. F. Hemond. Trapped methane volume and potential effects on methane ebullition in a northern peatland. *Limnol. Oceanogr.*, 41(7):1375–1383, 1996.

M. Ferer, C. Ji, G. S. Bromhal, J. Cook, G. Ahmadi, and D. H. Smith. Crossover from capillary fingering to viscous fingering for immiscible unstable flow: Experiment and modeling. *Phys. Rev. E*, 70:016303, 2004.

P. B. Flemings, X. Liu, and W. J. Winters. Critical pressure and multiphase flow in Blake Ridge gas hydrates. *Geology*, 31(12):1057–1060, 2003.

L. Furuberg, K. J. Måløy, and J. Feder. Intermittent behavior in slow drainage. *Phys. Rev. E*, 53 (1):966–977, 1996.

S. K. Garg, J. W. Pritchett, A. Katoh, K. Baba, and T. Fujii. A mathematical model for the formation and dissociation of methane hydrates in the marine environment. *J. Geophys. Res.*, 113 (B1):10.1029/2006JB004768, 2008.

G. D. Ginsburg and V. A. Soloviev. Methane migration within the submarine gas-hydrate stability zone under deep-water conditions. *Mar. Geol.*, 137:49–57, 1997.

D. Goldberg, T. Takahashi, and A. L. Slagle. Carbon dioxide sequestration in deep-sea basalt. *Proc. Natl. Acad. Sci. U.S.A.*, 105:9920–9925, 2008.

J. P. Gollub and J. S. Langer. Pattern formation in nonequilibrium physics. *Rev. Mod. Phys.*, 71: S396–S403, 1999.

X. Gong, S. Takagi, and Y. Matsumoto. The effect of bubble-induced liquid flow on mass transfer in bubble plumes. *Int. J. Multiphase Flow*, 35:155–162, 2009.

A. R. Gorman, W. S. Holbrook, M. J. Hornbach, K. L. Hackwith, D. Lizarralde, and I. Pecher. Migration of methane gas through the hydrate stability zone in a low-flux hydrate province. *Geology*, 30(4):327–330, 2002.

J. Greinert, D. F. McGinnis, L. Naudts, P. Linke, and M. De Batist. Atmospheric methane flux from bubbling seeps: Spatially extrapolated quantification from a Black Sea shelf area. *J. Geophys. Res.*, 115:C01002, 2010.

J. Greinert and B. Nutzel. Hydroacoustic experiments to establish a method for the determination of methane bubble fluxes at cold seeps. *Geo-Mar. Lett.*, 24(2):75–85, 2004.

W. B. Haines. Studies in the physical properties of soils. V. The hysteresis effect in capillary properties, and the modes of moisture redistribution associated therewith. *J. Agr. Sci.*, 20:97–116, 1930.

K. U. Heeschen, R. W. Collier, M. A. de Angelis, E. Suess, G. Rehder, P. Linke, and G. P. Klinkhammer. Methane sources, distributions, and fluxes from cold vent sites at Hydrate Ridge, Cascadia Margin. *Glob. Biogeochem. Cycle*, 19(2):GB2016, 2005.

K. U. Heeschen, H. J. Hohnberg, M. Haeckel, F. Abegg, M. Drews, and G. Bohrmann. In situ hydrocarbon concentrations from pressurized cores in surface sediments, Northern Gulf of Mexico. *Mar. Chem.*, 107:498–515, 2007.

K. U. Heeschen, A. M. Trehu, R. W. Collier, E. Suess, and G. Rehder. Distribution and height of methane bubble plumes on the Cascadia Margin characterized by acoustic imaging. *Geophys. Res. Lett.*, 30(12):1643, doi:10.1029/2003GL016974, 2003.

K. C. Hester and P. G. Brewer. Clathrate hydrates in nature. *Annu. Rev. Mar. Sci.*, 1(1):303–327, 2009.

W. S. Holbrook, H. Hoskins, W. T. Wood, R. A. Stephen, and D. Lizarralde. Methane hydrate and free gas on the Blake Ridge from vertical seismic profiling. *Science*, 273:1840–1842, September 27, 1996.

R. Holtzman and R. Juanes. Crossover from fingering to fracturing in deformable disordered media. *Phys. Rev. E*, 82:046305, doi:10.1103/PhysRevE.82.046305, 2010.

R. Holtzman, M. L. Szulczewski, and R. Juanes. Capillary fracturing in granular media. *Phys. Rev. Lett.*, page in press, 2012.

M. J. Hornbach, C. Ruppel, and C. L. Van Dover. Three-dimensional structure of fluid conduits sustaining an active deep marine cold seep. *Geophys. Res. Lett.*, 34:L05601, doi:10.1029/2006GL028859, 2007.

M. J. Hornbach, D. M. Saffer, and W. S. Holbrook. Critically pressured free-gas reservoirs below gas-hydrate provinces. *Nature*, 427(6970):142–144, 2004.

K. Z. House, D. P. Schrag, C. F. Harvey, and K. S. Lackner. Permanent carbon dioxide storage in deep-sea sediments. *Proc. Natl. Acad. Sci. U.S.A.*, 103:12291–12295, 2006.

M. Hovland, J. V. Gardner, and A. G. Judd. The significance of pockmarks to understanding fluid flow processes and geohazards. *Geofluids*, 2:127–136, 2002.

J. R. Hunt, N. Sitar, and K. S. Udell. Nonaqueous phase liquid transport and cleanup, 1. Analysis of mechanisms. *Water Resour. Res.*, 24(8):1247–1258, 1988.

IPCC. *Climate Change 2007: The Physical Science Basis*. Cambridge University Press, Cambridge, UK, 2007.

ITASCA. *PFC2D, v3.1 – Theory and Background*. Itasca Consulting Group, Inc., Minneapolis, MN, 2004.

A. K. Jain and R. Juanes. Pore-scale mechanistic study of the preferential mode of hydrate formation in sediments: Coupling of multiphase fluid flow and sediment mechanics. In *Proc. 6th Intl. Conf. Gas Hydrates (ICGH 2008)*, Vancouver, Canada, July 6–10, 2008.

A. K. Jain and R. Juanes. Preferential mode of gas invasion in sediments: grain-scale mechanistic model of coupled multiphase fluid flow and sediment mechanics. *J. Geophys. Res.*, 114:B08101, doi:10.1029/2008JB006002, 2009.

K. L. Johnson. *Contact Mechanics*. Cambridge University Press, 1987.

A. G. Judd, M. Hovland, L. I. Dimitrov, S. Garcia Gil, and V. Jukes. The geological methane budget at Continental Margins and its influence on climate change. *Geofluids*, 2:109–126, 2002.

S. Kato, T. Sakakibara, and H. Yoshimori. Effects of intergranular adhesive force on behavior of granular material. In Y. Shimizu, R. D. Hart, and P. Cundall, editors, *Numerical Modeling in Micromechanics Via Particle Methods. Proc. of the 2nd International PFC Symposium, Kyoto, Japan*, pages 347–354, Balkema, Leiden, October 2004.

M. Keller and R. F. Stallard. Methane emission by bubbling from Gatun Lake, Panama. *J. Geophys. Res.*, 99(D4):8307–8319, 1994.

J. P. Kennett and B. N. Fackler-Adams. Relationship of clathrate instability to sediment deformation in the upper Neogene of California. *Geology*, 28(3):215–218, 2000.

H. C. Kim, P. R. Bishnoi, R. A. Heideman, and S. S. H. Rizvi. Kinetics of methane hydrate decomposition. *Chem. Eng. Sci.*, 42(7):1645–1653, doi=10.1016/0009–2509(87)80169–0, 1987.

A. Klar, K. Soga, and M. Y. A. Ng. Coupled deformation-flow analysis for methane hydrate extraction. *Geotechnique*, 60(10):765–776, 2010.

H. Koide, Y. Shindo, Y. Tazaki, M. Iijima, K. Ito, N. Kimura, and K. Omata. Deep sub-seabed disposal of CO_2 – The most protective storage. *Energy Conv. Manag.*, 38:S253–S258, 1997a.

H. Koide, M. Takahashi, Y. Shindo, Y. Tazaki, M. Iijima, K. Ito, N. Kimura, and K. Omata. Hydrate formation in sediments in the sub-seabed disposal of CO_2. *Energy*, 22:279–283, 1997b.

H. Koide, M. Takahashi, and H. Tsukamoto. Self-trapping mechanisms of carbon dioxide in the aquifer disposal. *Energy Conv. Manag.*, 36:505–508, 1995.

X.-Z. Kong, W. Kinzelbach, and F. Stauffer. Morphodynamics during air injection into water-saturated movable spherical granulates. *Chem. Eng. Sci.*, 65:4652–4660, 2010.

M. B. Kowalsky and G. J. Moridis. Comparison of kinetic and equilibrium reaction models in simulating gas hydrate behavior in porous media. *Energy Conv. Manag.*, 48(6):1850–1863, 10.1016/j.enconman.2007.01.017, 2007.

K. A. Kvenvolden. Methane hydrate – a major reservoir of carbon in the shallow geosphere? *Chem. Geol.*, 71:41–51, 1988.

T. H. Kwon, G.-C. Cho, and J. C. Santamarina. Gas hydrate dissociation in sediments: Pressure-temperature evolution. *Geochem. Geophys. Geosyst.*, 9(3):Q03019, doi=10.1029/2007GC001920, 2006.

T. H. Kwon, K.-I. Song, and G.-C. Cho. Destabilization of marine gas hydrate-bearing sediments induced by a hot wellbore: A numerical approach. *Energ. Fuel.*, 24(10):5493–5507, 2010.

C.-H. Lam. Fluid invasion in porous media: viscous gradient percolation. *Phys. Rev. Lett.*, 92(25): 254503, 2004.

I. Leifer and J. Boles. Turbine tent measurements of marine hydrocarbon seeps on subhourly timescales. *J. Geophys. Res.*, 110(C1):C01006, 2005.

I. Leifer, B. P. Luyendyk, J. Boles, and J. F. Clark. Natural marine seepage blowout: Contribution to atmospheric methane. *Glob. Biogeochem. Cycle*, 20(3):GB3008, 2006.

A. M. Leitch and W. D. Baines. Liquid volume flux in a weak bubble plume. *J. Fluid Mech.*, 205: 77–98, 1989.

E. Lemaire, P. Levitz, G. Daccord, and H. Van Damme. From viscous fingering to viscoelastic fracturing in colloidal fluids. *Phys. Rev. Lett.*, 67(15):2009–2012, 1991.

R. Lenormand. Flow through porous media: limits of fractal patterns. *Proc. R. Soc. Lond. A*, 423: 159–168, 1989.

R. Lenormand, E. Touboul, and C. Zarcone. Numerical models and experiments on immiscible displacements in porous media. *J. Fluid Mech.*, 189:165–187, 1988.

R. Lenormand, C. Zarcone, and A. Sarr. Mechanisms of the displacement of one fluid by another in a network of capillary ducts. *J. Fluid Mech.*, 135:123–132, 1983.

M. C. Leverett. Capillary behavior of porous solids. *Petrol. Trans.* AIME, 142:152–169, 1941.

A. Levermann and I. Procaccia. Bi-Laplacian growth patterns in disordered media. *Phys. Rev. Lett.*, 89(23):234501, 2002.

J. S. Levine, J. M. Matter, D. Goldberg, A. Cook, and K. S. Lackner. Gravitational trapping of carbon dioxide in deep sea sediments: Permeability, buoyancy, and geomechanical analysis. *Geophys. Res. Lett.*, 34:L24703, doi:10.1029/2007GL031560, 2007.

L. Li and R. M. Holt. Simulation of flow in sandstone with fluid coupled particle model. In *Rock Mechanics in the National Interest. Proceedings of the 38th U.S. Rock Mechanics Symposium, Washington, D.C.*, volume 1, pages 165–172, Balkema, Rotterdam, July 2001.

L. Li and R. M. Holt. A study on the calculation of particle volumetric deformation in a fluid coupled PFC model. In Y. Shimizu, R. D. Hart, and P. Cundall, editors, *Numerical Modeling in Micromechanics Via Particle Methods. Proc. of the 2nd International PFC Symposium, Kyoto, Japan*, pages 273–279, Balkema, Leiden, October 2004.

Y. Li, Y. Xu, and C. Thornton. A comparison of discrete element simulations and experiments for "sandpiles" composed of spherical particles. *Powder Technol.*, 160(3):219–228, 2005.

G. Lian, C. Thornton, and M. J. Adams. A theoretical study of the liquid bridge forces between two rigid spherical bodies. *J. Colloid Interface Sci.*, 161:138–147, 1993.

A. Lindner, P. Coussot, and D. Bonn. Viscous fingering in a yield stress fluid. *Phys. Rev. Lett.*, 85: 314–317, 2000.

X. Liu and P. B. Flemings. Passing gas through the hydrate stability zone at southern Hydrate Ridge, offshore Oregon. *Earth Planet. Sci. Lett.*, 241:211–216, 2006.

X. Liu and P. B. Flemings. Dynamic multiphase flow model of hydrate formation in marine sediments. *J. Geophys. Res.*, 112:B03101, doi:10.1029/2005JB004227, 2007.

X. Liu and P. B. Flemings. Dynamic response of oceanic hydrates to sea level drop. *Geophys. Res. Lett.*, 36:L17308, doi:10.1029/2009GL039821, 2009.

G. Løvoll, Y. Méheust, R. Toussaint, J. Schmittbuhl, and K. J. Måløy. Growth activity during fingering in a porous Hele-Shaw cell. *Phys. Rev. E*, 70:026301, 2004.

K. J. Måløy, J. Feder, and T. Jøssang. Viscous fingering fractals in porous media. *Phys. Rev. Lett.*, 55(24):2688–2691, 1985.

K. J. Måløy, L. Furuberg, J. Feder, and T. Jøssang. Dynamics of slow drainage in porous media. *Phys. Rev. Lett.*, 68(14):2161–2164, 1992.

C. S. Martens and J. Val Klump. Biogeochemical cycling in an organic-rich coastal marine basin. 1. Methane sediment-water exchange processes. *Geochim. Cosmochim. Acta*, 44(3):471–490, 1980.

G. Mason and N. R. Morrow. Capillary behavior of a perfectly wetting liquid in irregular triangular tubes. *J. Colloid Interface Sci.*, 141:262, 1991.

M. D. Mattson and G. E. Likens. Air pressure and methane fluxes. *Nature*, 347:718–719, 1990.

R. P. Mayer and R. A. Stowe. Mercury-porosimetry breakthrough pressure for penetration between packed spheres. *J. Colloid Interface Sci.*, 20:893, 1965.

D. F. McGinnis, J. Greinert, Y. Artemov, S. E. Beaubien, and A. Wuest. Fate of rising methane bubbles in stratified waters: How much methane reaches the atmosphere? *J. Geophys. Res.*, 111 (C9):C09007, 2006.

P. Meakin. Models for material failure and deformation. *Science*, 252:226–234, 1991.

P. Meakin, G. Li, L. M. Sander, E. Louis, and F. Guinea. A simple two-dimensional model for crack propagation. *J. Phys. A: Math. Gen.*, 22:1393–1403, 1989.

J. Mienert, M. Vanneste, S. Bünz, K. Andreassen, H. Haflidason, and H. P. Sejrup. Ocean warming and gas hydrate stability on the mid-Norwegian margin at the Storegga slide. *Mar. Pet. Geol.*, 22:233–244, 2005.

A. V. Milkov, G. R. Dickens, G. E. Claypool, Y.-J. Lee, W. S. Borowski, M. E. Torres, W. Xu, H. Tomaru, A. M. Trehu, and P. Schultheiss. Co-existence of gas hydrate, free gas, and brine within the regional gas hydrate stability zone at Hydrate Ridge (Oregon margin): evidence from prolongued degassing of a pressurized core. *Earth Planet. Sci. Lett.*, 222:829–843, 2004.

A. V. Milkov and W. Xu. Comment on "Gas hydrate growth, methane transport, and chloride enrichment at the southern summit of Hydrate Ridge, Cascadia margin off Oregon" by Torres et al. [Earth Planet. Sci. Lett. 226:225–241 (2004)]. *Earth Planet. Sci. Lett.*, 239:162–167, 2005.

M. Muskat. *Physical Principles of Oil Production*. McGraw-Hill, New York, 1949.

G. L. Netzeband, C. P. Hübscher, D. Gajewski, J. W. G. Grobys, and J. Bialas. Seismic velocities from the Yaquina forearc basin off Peru: evidence for free gas within the gas hydrate stability zone. *Int. J. Earth Sci.*, 94:420–432, 2005.

L. Niemeyer, L. Pietronero, and H. J. Wiesmann. Fractal dimension of dielectric breakdown. *Phys. Rev. Lett.*, 52(12):1033–1036, 1984.

J. Nimblett and C. Ruppel. Permeability evolution during the formation of gas hydrates in marine sediments. *J. Geophys. Res.*, 108(B9):2420, doi:10.1029/2001JB001650, 2003.

J. A. Nunn and P. Meulbroek. Kilometer-scale upward migration of hydrocarbons in geopressured sediments by buoyancy-driven propagation of methane-filled fractures. *AAPG Bull.*, 86(5):907–918, 2002.

A. Obzhirov, R. Shakirov, A. Salyuk, E. Suess, N. Biebow, and A. Salomatin. Relations between methane venting, geological structure and seismo-tectonics in the Okhotsk Sea. *Geo-Mar. Lett.*, 24:135–139, 2004.

P. E. Øren, S. Bakke, and O. J. Arntzen. Extending predictive capabilities to network models. *Soc. Pet. Eng. J.*, 3(4):324–336, December 1998.

F. M. Orr, L. E. Scriven, and A. P. Rivas. Pendular rings between solids: meniscus properties and capillary force. *J. Fluid Mech.*, 67:723–742, 1975.

L. Paterson. Diffusion-limited aggregation and two-fluid displacements in porous media. *Phys. Rev. Lett.*, 52(18):1621–1624, 1984.

T. W. Patzek. Verification of a complete pore network simulator of drainage and imbibition. *Soc. Pet. Eng. J.*, 6(2):144–156, June 2001.

T. W. Patzek and D. B. Silin. Shape factor and hydraulic conductance in noncircular capillaries: I. One-phase creeping flow. *J. Colloid Interface Sci.*, 296:295–304, 2001.

C. K. Paull, P. G. Brewer, W. Ussler, E. T. Peltzer, G. Rehder, and D. Clague. An experiment demonstrating that marine slumping is a mechanism to transfer methane from seafloor gas-hydrate deposits into the upper ocean and atmosphere. *Geo-Mar. Lett.*, 22:198–203, 2003.

C. K. Paull, W. Ussler, S. R. Dallimore, S. M. Blasco, T. D. Lorenson, H. Mellling, B. E. Medioli, F. M. Nixon, and F. A. McLaughlin. Origin of pingo-like features on the Beaufort Sea shelf and their possible relationship to decomposing methane gas hydrates. *Geophys. Res. Lett.*, 34: L01603, 2007.

D. O. Potyondy and P. A. Cundall. A bonded-particle model for rock. *Int. J. Rock Mech. Min. Sci.*, 41:1329–1364, 2004.

O. Praud and H. L. Swinney. Fractal dimension and unscreened angles measured for radial viscous fingering. *Phys. Rev. E*, 72:011406, 2005.

P. B. Price and T. Sowers. Temperature dependence of metabolic rates for microbial growth, maintenance, and survival. *Proc. Natl. Acad. Sci. U.S.A.*, 101(13):4631–4636, 2004.

H. M. Princen. Capillary phenomena in assemblies of parallel cylinders. I. Capillary rise between two cylinders. *J. Colloid Interface Sci.*, 30:60, 1969a.

H. M. Princen. Capillary phenomena in assemblies of parallel cylinders. II. Capillary rise in systems with more than two cylinders. *J. Colloid Interface Sci.*, 30:359, 1969b.

H. M. Princen. Capillary phenomena in assemblies of parallel cylinders. III. Liquid columns between horizontal parallel cylinders. *J. Colloid Interface Sci.*, 34:171, 1970.

M. Prodanovic and S. Bryant. A level set method for determining critical curvatures for drainage and imbibition. *J. Colloid Interface Sci.*, 304:442–458, 2006.

M. T. Reagan and G. J. Moridis. Large-scale simulation of methane hydrate dissociation along the West Spitsbergen Margin. *Geophys. Res. Lett.*, 36:L23612, 2009.

G. Rehder, P. W. Brewer, E. T. Peltzer, and G. Friederich. Enhanced lifetime of methane bubble streams within the deep ocean. *Geophys. Res. Lett.*, 29(15):1731, 2002.

L. A. Richards. Capillary conduction of liquids through porous mediums. *Physics*, 1:318–333, 1931.

M. Riedel, T. S. Collett, M. J. Malone, and the Expedition 311 Scientists, editors. *Cascadia Margin Gas Hydrates*, volume 311 of *Proc. IODP, Expedition Reports*, College Station, TX, 2006. Integrated Ocean Drilling Program.

J. W. M. Rudd, R. D. Hamilton, and N. E. Campbell. Measurement of microbial oxidation of methane in lake water. *Limnol. Oceanogr.*, 19(3):519–524, 1974.

C. Ruppel, G. R. Dickens, D. G. Castellini, W. Gilhooly, and D. Lizarralde. Heat and salt inhibition of gas hydrate formation in the northern Gulf of Mexico. *Geophys. Res. Lett.*, 32:L04605, doi:10.1029/2004GL021909, 2005.

J. Rutqvist and G. J. Moridis. Numerical studies on the geomechanical stability of hydrate-bearing sediments. *Soc. Pet. Eng. J.*, 14(2):267–282, 2009.

H. Sahling, G. Bohrmann, V. Spiess, J. Bialas, M. Breitzke, M. Ivanov, S. Kasten, S. Krastel, and R. Schneider. Pockmarks in the Northern Congo Fan area, SW Africa: Complex seafloor features shaped by fluid flow. *Mar. Geol.*, 249:206–225, 2008.

B. Sandnes, E.G. Flekkøy, H.A. Knudsen, K. J. Måløy, and H. See. Patterns and flow in frictional fluid dynamics. *Nat. Commun.*, 2:288, 2011.

B. Sandnes, H. A. Knudsen, K. J. Måløy, and E. G. Flekkøy. Labyrinth patterns in confined granular-fluid systems. *Phys. Rev. Lett.*, 99(3):038001, 2007.

R. Sassen, S. L. Losh, L. Cathles III, H. H. Roberts, J. K. Whelan, A. V. Milkov, S. T. Sweet, and D. A. DeFreitas. Massive vein-filling gas hydrate: relation to ongoing gas migration from the deep subsurface in the Gulf of Mexico. *Mar. Pet. Geol.*, 18:551–560, 2001.

B. P. Scandella. Numerical modeling of methane venting from lake sediments. Master's thesis, Massachusetts Institute of Technology, Cambridge, Massachusetts, 2010.

B. P. Scandella, C. Varadharajan, H. Hemond, C. Ruppel, and R. Juanes. A conduit dilation model of methane venting from lake sediments. *Geophys. Res. Lett.*, 38:L06408, doi:10.1029/2011GL046768, 2011.

N. Shakhova, I. Semiletov, A. Salyuk, V. Yusupov, D. Kosmach, and Ö. Gustafsson. Extensive methane venting to the atmosphere from sediments of the East Siberian Arctic shelf. *Science*, 327:1246–1250, 2010.

Y. Shimizu. Fluid coupling in PFC2D and PFC3D. In Y. Shimizu, R. D. Hart, and P. Cundall, editors, *Numerical Modeling in Micromechanics Via Particle Methods. Proc. of the 2nd International PFC Symposium, Kyoto, Japan*, pages 281–287, Balkema, Leiden, October 2004.

Hosung Shin and J. Carlos Santamarina. Fluid-driven fractures in uncemented sediments: Underlying particle-level processes. *Earth Planet. Sci. Lett.*, 299(1–2):180–189, 2010.

G. C. Sills, S. J. Wheeler, S. D. Thomas, and T. N. Gardner. Behavior of offshore soils containing gas bubbles. *Geotechnique*, 41(2):227–241, 1991.

E. D. Sloan. *Clathrate Hydrates of Natural Gases*. Marcel Deker, New York, second edition, 1998.

E. D. Sloan. Fundamental principles and applications of natural gas hydrates. *Nature*, 426:353–359, November 23, 2003.

E. D. Sloan and C. A. Koh. *Clathrate Hydrates of Natural Gases*. CRC Press, New York, third edition, 2008.

E. A. Solomon, M. Kastner, I. R. MacDonald, and I. Leifer. Considerable methane fluxes to the atmosphere from hydrocarbon seeps in the Gulf of Mexico. *Nat. Geosci.*, 2(8):561–565, 2009.

V. A. Soloviev and G. D. Ginsburg. Water segregation in the course of gas hydrate formation and accumulation in submarine gas-seepage fields. *Mar. Geol.*, 137:59–68, 1997.

J. P. Stokes, D. A. Weitz, J. P. Gollub, A. Dougherty, M. O. Robbins, P. M. Chaikin, and H. M. Lindsay. Interfacial stability of immiscible displacement in a porous medium. *Phys. Rev. Lett.*, 57:1718–1721, 1986.

E. Suess, M. E. Torres, G. Bohrmann, R. W. Collier, J. Greinert, P. Linke, G. Rehder, A. Trehu, K. Wallmann, G. Winckler, and E. Zuleger. Gas hydrate destabilization: enhanced dewatering, benthic material turnover and large methane plumes at the Cascadia convergent margin. *Earth Planet. Sci. Lett.*, 170:1–15, 1999.

N. Sultan, P. Cochonat, J.-P. Foucher, and J. Mienert. Effect of gas hydrates melting on seafloor slope instability. *Mar. Geol.*, 213:379–401, 2004.

K. t. Leung and Z. Néda. Pattern formation and selection in quasistatic fracture. *Phys. Rev. Lett.*, 85(3):662–665, 2000.

B. B. Tan. Geotechnical characterization of sediments from Hydrate Ridge, Cascadia continental margin. M.Sc. Thesis, MIT, Cambridge, MA, 2004.

B. B. Tan, J. T. Germaine, and P. B. Flemings. Data report: Consolidation and strength characteristics of sediments from ODP Site 1244, Hydrate Ridge, Cascadia continental margin. In *Proc. Ocean Drilling Program, Sci. Results*, volume 204, 2006.

K. Terzaghi. *Theoretical Soil Mechanics*. John Wiley, New York, 1943.

S. D. Thomas. *The consolidation behaviour of gassy soil*. PhD thesis, University of Oxford, 1987.

M. E. Torres, J. McManus, D. E. Hammond, M. A. de Angelis, K. U. Heeschen, S. L. Colbert, M. D. Tryon, K. M. Brown, and E. Suess. Fluid and chemical fluxes in and out of sediments hosting methane hydrate deposits on Hydrate Ridge, OR, I: Hydrological provinces. *Earth Planet. Sci. Lett.*, 201:525–540, 2002.

M. E. Torres, K. Wallmann, A. M. Trehu, G. Bohrmann, W. S. Borowski, and H. Tomaru. Gas hydrate growth, methane transport, and chloride enrichment at the southern summit of Hydrate Ridge, Cascadia margin off Oregon. *Earth Planet. Sci. Lett.*, 226:225–241, 2004.

M. E. Torres, K. Wallmann, A. M. Trehu, G. Bohrmann, W. S. Borowski, and H. Tomaru. Reply to comment on: "Gas hydrate growth, methane transport, and chloride enrichment at the southern summit of Hydrate Ridge, Cascadia margin off Oregon". *Earth Planet. Sci. Lett.*, 239:168–175, 2005.

R. Toussaint, G. Løvoll, Y. Méheust, K. J. Måløy, and J. Schmittbuhl. Influence of pore-scale disorder on viscous fingering during drainage. *Europhys. Lett.*, 71(4):583–589, 2005.

A. M. Trehu, G. Bohrmann, M. E. Torres, and F. S. Colwell, editors. *Drilling Gas Hydrates on Hydrate Ridge, Cascadia Continental Margin*, volume 204 of *Proc. ODP, Sci. Results*, College Station, TX, 2006a. Ocean Drilling Program. doi:10.2973/odp.proc.sr.204.2006.

A. M. Trehu, P. B. Flemings, N. L. Bangs, J. Chevalier, E. Gracia, J. E. Johnson, C.-S. Liu, X. Liu, M. Riedel, and M. E. Torres. Feeding methane vents and gas hydrate deposits at south Hydrate Ridge. *Geophys. Res. Lett.*, 31:L23310, doi:10.1029/2004GL021286, 2004a.

A. M. Trehu, P. E. Long, M. E. Torres, G. Bohrmann, F. R. Rack, T. S. Collett, D. S. Goldberg, A. V. Milkov, M. Riedel, P. Schultheiss, N. L. Bangs, S. R. Barr, W. S. Borowski, G. E. Claypool, M. E. Delwiche, G. R. Dickens, E. Gracia, G. Guerin, M. Holland, J. E. Johnson, Y. J. Lee, C. S. Liu, X. Su, B. Teichert, H. Tomaru, M. Vanneste, M. Watanabe, and J. L. Weinberger. Three-dimensional distribution of gas hydrate beneath southern Hydrate Ridge: constraints from ODP Leg 204. *Earth Planet. Sci. Lett.*, 222:845–862, 2004b.

A. M. Trehu, C. Ruppel, M. Holland, G. R. Dickens, M. E. Torres, T. S. Collett, D. Goldberg, R. Riedel, and P. Schultheiss. Gas hydrates in marine sediments: lessons from scientific drilling. *Oceanography*, 19(4):124–143, 2006b.

M. D. Tryon, K. M. Brown, and M. E. Torres. Fluid and chemical flux in and out of sediments hosting methane hydrate deposits on Hydrate Ridge, OR, II: Hydrological processes. *Earth Planet. Sci. Lett.*, 201:541–557, 2002.

M. D. Tryon, K. M. Brown, M. E. Torres, A. M. Trehu, J. McManus, and R. W. Collier. Measurements of transience and downward fluid flow near episodic methane gas vents, Hydrate Ridge, Cascadia. *Geology*, 27(12):1075–1078, 1999.

I. N. Tsimpanogiannis and P. C. Lichtner. Pore-network study of methane hydrate dissociation. *Phys. Rev. E*, 74(5):056303, 2006.

F. Tzschichholz and H. J. Herrmann. Simulations of pressure fluctuations and acoustic emission in hydraulic fracturing. *Phys. Rev. E*, 51(3):1961–1970, 1995.

D. L. Valentine, D. C. Blanton, W. S. Reeburgh, and M. Kastner. Water column methane oxidation adjacent to an area of active hydrate dissociation, Eel River Basin. *Geochim. Cosmochim. Acta*, 65(16):2633–2640, 2001.

P. Van Rensbergen, M. De Batist, J. Klerkx, R. Hus, J. Poort, M. Vanneste, N. Granin, O. Khlystov, and P. Krinitsky. Sublacustrine mud volcanoes and methane seeps caused by dissociation of gas hydrates in Lake Baikal. *Geology*, 30(7):631–634, 2002.

C. Varadharajan. *Magnitude and Spatio-Temporal Variability of Methane Emissions from a Eutrophic Freshwater Lake*. PhD Dissertation, November 2009.

C. Varadharajan, R. Hermosillo, and H. F. Hemond. A low-cost automated trap to measure bubbling gas fluxes. *Limnol. Oceanogr. Methods*, 8:363–375, 2010.

G. Varas, V. Vidal, and J.-C. Géminard. Morphology of air invasion in an immersed granular layer. *Phys. Rev. E*, 83:061302, 2011.

W. F. Waite, T. J. Kneafsey, W. J. Winters, and D. H. Mason. Physical property changes in hydrate-bearing sediment due to depressurization and subsequent repressurization. *J. Geophys. Res.*, 113:B07102, 2008.

W. F. Waite, J. C. Santamarina, D. D. Cortes, B. Dugan, D. N. Espinoza, J. Germaine, J. Jang, J. W. Jung, T. J. Kneafsey, H. Shin, K. Soga, W. J. Winters, and T-S. Yun. Physical properties of hydrate-bearing sediments. *Rev. Geophys.*, 47:10.1029/2008RG000279, 2009.

K. M. Walter, S. A. Zimov, J. P. Chanton, D. Verbyla, and F. S. Chapin III. Methane bubbling from Siberian thaw lakes as a positive feedback to climate warming. *Nature*, 443:71–75, 2006.

H. F. Wang. *Theory of Linear Poroelasticity*. Princeton University Press, 2000.

J. L. Weinberger and K. M. Brown. Fracture networks and hydrate distribution at Hydrate Ridge, Oregon. *Earth Planet. Sci. Lett.*, 245:123–136, 2006.

J. L. Weinberger, K. M. Brown, and P. E. Long. Painting a picture of gas hydrate distribution with thermal images. *Geophys. Res. Lett.*, 32:L04609, doi:10.1029/2004GL021437, 2005.

G. K. Westbrook, K. E. Thatcher, et al. Escape of methane gas from the seabed along the West Spitsbergen continental margin. *Geophys. Res. Lett.*, 36:L15608, doi:10.1029/2009GL039191, 2009.

S. J. Wheeler. Movement of large gas bubbles in unsaturated fine-grained sediments. *Mar. Geotechnol.*, 9(2):113–129, 1990.

D. Wilkinson and J. Willemsen. Invasion percolation: a new form of percolation theory. *J. Phys. A*, 16:3365–3376, 1983.

W. T. Wood, J. F. Gettrust, N. R. Chapman, G. D. Spence, and R. D. Hyndman. Decreased stability of methane hydrates in marine sediments owing to phase-boundary roughness. *Nature*, 420: 656–660, 2002.

L. Xu, S. Davies, A. B. Schofield, and D. A. Weitz. Dynamics of drying in 3D porous media. *Phys. Rev. Lett.*, 101:094502, 2008.

W. Xu and L. N. Germanovich. Excess pore pressure resulting from methane hydrate dissociation in marine sediments: A theoretical approach. *J. Geophys. Res.*, 111:B01104, doi:10.1029/2004JB003600, 2006.

W. Xu and C. Ruppel. Predicting the occurrence, distribution, and evolution of methane gas hydrate in porous marine sediments. *J. Geophys. Res.*, 104(B3):5081–5095, 1999.

Y. C. Yortsos, B. Xu, and D. Salin. Phase diagram of fully-developed drainage in porous media. *Phys. Rev. Lett.*, 79(23):4581–4584, 1997.

L. Zühlsdorff and V. Spiess. Three-dimensional seismic characterization of a venting site reveals compelling indications of natural hydraulic fracturing. *Geology*, 32(2):101–104, 2004.

Appendix – Description of Underlying Models

A significant portion of this research involved the development of new models of grain-scale phenomena, especially the motion of gas/water interfaces in granular materials. Novel aspects included the development of physically representative network models that eliminate the artificial boundary conditions that have been applied to all network models in the past; models and methods that simultaneously account for capillarity-driven gas invasion and grain displacement by gas pressure forces; a method to approximate the fundamental physics of imbibition (which requires explicit representation of the geometry of grains in the porous medium) in a network model which has no representation of the grain geometry; a method to validate the basic premise of network modeling (viz. that individual pore-filling events can be correctly captured by a set of rules).

These models underlie much of the analysis described in the body of this report. However many of them do not have immediate application to the behavior of hydrate-bearing sediments, which is the main focus of this report. We therefore describe these models by reference, that is, we cite the series of quarterly progress reports prepared over the course of this project for DOE NETL, and we refer to publications that have appeared on the same topics. All reports and publications are publicly available. We group these citations under three broad categories: model sediments, drainage/imbibition simulations, and capillarity/mechanics coupling.

Model Sediments

We developed algorithms to produce model sediments (dense, disordered packings of spheres) with a range of grain size distributions. The set of model sediments provided a test bed for drainage and imbibition simulations. The models are described in

Juanes R., and Bryant, S. L., 2007. "Mechanisms Leading to Co-Existence of Gas and Hydrate in Ocean Sediments," *Creation of Sediment Models – Task 3 Technical Report*, University of Texas, DOE Award No.: DE-FC26-06NT43067. April 2007. (http://1.usa.gov/HvIJHF)

Advanced Methods for Simulating Drainage and Imbibition

We extended the Level Set Method for capillarity-controlled displacements (Prodanović and Bryant, *J. Colloid. Interfac. Sci,* 2006) to account for the geometry in rough-walled fractures (relevant to the problem of when and where hydrates could grow following gas invasion by fracturing a sediment). We also developed the concept of infinite-acting network models. These enabled the first fundamentally correct prediction of residual saturations resulting from drainage/imbibition displacements in nature, where no explicit boundaries for the sediment/rock exist.

Prodanović, M., Bryant, S.L., and Karpyn, Z.T., "Investigating Matrix/Fracture Transfer via a Level Set Method for Drainage and Imbibition," *Society of Petroleum Engineers Journal*, Volume 15, Number 1, pp. 125-136, March 2010. DOI: 10.2118/116110-PA, published online 12 November 2009.

Prodanović, M. and Bryant, S., "Physics-Driven Interface Modeling for Drainage and Imbibition in Fractures," *Society of Petroleum Engineers Journal,* Volume 14, Number 3, pp. 532-542, September 2009. DOI: 10.2118/110448-PA, published online 27 July 2009.

Behseresht, J., Bryant, S. and Seperhnoori, K., "Infinite-Acting Physically Representative Networks for Capillarity-Controlled Displacements," *Society of Petroleum Engineers Journal,* Volume 14, Number 4, pp. 568-578, December 2009. DOI: 10.2118/110581-PA, published online 16 July 2009.

Peng, Y., Prodanović, M., and Bryant, S., "Improving Fidelity of Network Models for Drainage and Imbibition," SPE 124440 prepared for presentation at the 2009 SPE Annual Technical Conference and Exhibition held in New Orleans, Louisiana, USA, 4–7 October 2009.

Behseresht, J., Peng, Y., Prodanovic, M., and Bryant, S. L., 2008. "Grain Scale Study of Hydrate Formation in Sediments from Methane Gas: Role of Capillarity," *Proceedings of the 6th International Conference on Gas Hydrates (ICGH 2008),* Vancouver, British Columbia, CANADA, July 6-10, 2008. (http://1.usa.gov/H85rUn)

Prodanović, M. and Bryant, S., "Physics-Driven Interface Modeling for Drainage and Imbibition in Fractures," SPE110448, *Proceedings of the 2007 SPE Annual Technical Conference and Exhibition,* Anaheim, California, USA, 11–14 November 2007.

Coupled Capillarity-Controlled Fluid Displacement with Mechanics

The competition between fracturing and drainage as modes of gas invasion is fundamental to oceanic hydrate-bearing sediments. Thus we carried out extensive development of methods that account for both processes simultaneously.

Prodanović, M., Holder, J. and Bryant, S. "Pore Scale Coupling of Fluid Displacement and Unconsolidated Sediment Mechanics," accepted for publication in the *International Journal of Oil, Gas and Coal Technology*, 21 Oct 2011.

Holtzman, R. and R. Juanes. Mechanisms of gas transport in sediments: crossover from fingering to fracturing. In CD Proc., 7th International Conference on Gas Hydrates (ICGH 2011), Edinburgh, Scotland, UK, July 17-21, 2011.

Holtzman, R. and R. Juanes. Crossover from fingering to fracturing in deformable disordered media. *Physical Review E*, 82(4):046305 (2010), doi:10.1103/PhysRevE.82.046305.

Prodanović, M., Holder, J. and Bryant, S., "Coupling Capillarity-Controlled Fluid Displacement With Unconsolidated Sediment Mechanics: Grain Scale Fracture Opening," SPE 124717 prepared for presentation at the 2009 SPE Annual Technical Conference and Exhibition held in New Orleans, Louisiana, USA, 4–7 October 2009.

Jain, A. K. and R. Juanes. Preferential mode of gas invasion in sediments: grain-scale mechanistic model of coupled multiphase fluid flow and sediment mechanics. *Journal of Geophysical Research*, 114, B08101 (2009), doi:10.1029/2008JB006002.

Jain, A. K., and Juanes, R., 2008. "Pore-scale Mechanistic Study of the Preferential Mode of Hydrate Formation in Sediments: Coupling of Multiphase Fluid Flow and Sediment Mechanics," *Proceedings of the 6th International Conference on Gas Hydrates (ICGH 2008),* Vancouver, British Columbia, CANADA, July 6-10, 2008.

Prodanović, M. and Bryant, S., "Capillarity Controlled Displacements in Sediments With Movable Grains: Implications for Growth of Methane Hydrates," SPE 116663, *Proceedings of the 2008 SPE Annual Technical Conference and Exhibition,* Denver, Colorado, USA, 21–24 September 2008.

Experiments of Multiphase Fluid Displacement with Mechanics

R. Holtzman, M. L. Szulczewski, and R. Juanes. Capillary fracturing in granular media. *Physical Review Letters*, in press (2012).

Choi, J.-H., Y. Seol, R. Boswell and R. Juanes. X-ray computed-tomography imaging of gas migration in water-saturated sediments: from capillary invasion to conduit opening. *Geophysical Research Letters*, 38, L17310 (2011), doi:10.1029/2011GL048513.

Publications on Field-scale Modeling and Hydrate-Bearing Sediments

For completeness we list other publications based on the research described in this report that deal with hydrate-bearing sediments; these topics are covered in the main body of the report.

Scandella, B. P. and R. Juanes. Numerical modeling of hydrate formation from methane gas transport through dynamic conduits. In CD Proc., 7th International Conference on Gas Hydrates (ICGH 2011), Edinburgh, Scotland, UK, July 17-21, 2011.

Scandella, B. P., C. Varadharajan, H. F. Hemond, C. Ruppel and R. Juanes. A conduit dilation model of methane venting from lake sediments. *Geophysical Research Letters*, 38, L06408 (2011), doi:10.1029/2011GL046768.

Holtzman, R. and R. Juanes. Pore-scale modeling of overpressure caused by hydrate dissociation. In CD Proc., 7th International Conference on Gas Hydrates (ICGH 2011), Edinburgh, Scotland, UK, July 17-21, 2011.

Holtzman, R. and R. Juanes. Thermodynamic and hydrodynamic constraints on overpressure caused by hydrate dissociation: a pore-scale model. *Geophysical Research Letters*, 38, L14308 (2011), doi:10.1029/2011GL047937.

Behseresht, J. and Bryant, S., 2011. "Sedimentological Control on Saturation Distribution in Arctic Gas-Hydrate-Bearing Sands," *U.S. DOE-NETL Fire in the Ice Newsletter*, Vol. 11, Issue 1.

Behseresht, J. and Bryant, S., "Effect of Relative Permeability Characteristics and Gas/Water Flow on Gas-Hydrate Saturation Distribution," SPE 147221 prepared for presentation at the SPE Annual Technical Conference and Exhibition to be held in Denver, Colorado, USA, 30 October–2 November 2011.

Behseresht, J. and Bryant, S., "Sedimentological Control On Hydrate Saturation Distribution In Arctic Gas-Hydrate-Bearing Deposits," Proceedings of the 7th International Conference on Gas Hydrates (ICGH 2011), Edinburgh, Scotland, United Kingdom, July 17-21, 2011.

Behseresht, J., Peng, Y., Bryant, S. and Winters, W. "Sedimentological Control on Arctic Gas-Hydrate-Bearing Deposits," poster GC51A-0707, American Geophysical Union Fall Meeting, San Francisco, 14-18 Dec. 2009.

Juanes, R., and Bryant, S. L., 2009. "Models provide clues to how methane gas and hydrate coexist in nature," *U.S. DOE-NETL Fire in the Ice Newsletter*, Vol. 9, Issue 4, pgs. 7-11. (http://1.usa.gov/HBY7gM)

Behseresht, J., Peng, Y., Prodanovic, M., and Bryant, S. L., 2008. "Mechanisms by Which Methane Gas and Methane Hydrate Coexist in Ocean Sediments," *Offshore Technology Conference*, Houston, Texas, May 5-8, 2008. (http://1.usa.gov/H46RP8)

Holtzman, R., and Juanes, R., 2009. "Hydrate Formation in Gas-Rich Marine Sediments: A Grain-Scale Model," *Eos Trans*. AGU 90(52), Fall Meet. Suppl. OS41A-08.

Material in Preparation or in Review

At the time of submission of this report, several scholarly works are in progress. We include them here for reference.

Behseresht, J. Dec 2012. "Sedimentological and Transport Control of Conversion of Gas Reservoirs to Hydrate during Global Cooling". Ph.D. Dissertation – The University of Texas at Austin.

Behseresht, J. and Bryant, S. Sedimentological Control on Saturation Distribution in Arctic Gas-Hydrate-Bearing Sands, in review, *Earth Plan. Sci. Lett*.

Theses and Dissertations

Behseresht, J. 2008. "Infinite-Acting Physically Representative Networks for Capillarity-Controlled Displacements". M.S. Thesis – The University of Texas at Austin.

Jain, A. K., 2009. "Preferential Mode of Gas Invasion in Sediments: Grain-Scale Model of Coupled Multiphase Fluid Flow and Sediment Mechanics," M. S. Thesis - Massachusetts Institute of Technology.

Peng, Y. 2011. "Study of Methane Hydrate Formation and Distribution in Arctic Regions: From Pore Scale to Field Scale" Ph.D. Dissertation – The University of Texas at Austin.

Scandella, B. P. 2010. "Numerical modeling of methane venting from lake sediments." M.S. Thesis, Massachusetts Institute of Technology.

Progress Reports

Quarterly progress reports in chronological order include

- 2006 Q4
- 2007 Q1
- 2007 Q2
- 2007 Q3
- 2007 Q4
- 2008 Q1
- 2008 Q2
- 2008 Q4
- 2009 Q1
- 2009 Q2
- 2009 Q3
- 2009 Q4
- 2010 Q1
- 2010 Q2
- 2010 Q3
- 2010 Q4
- 2011 Q1
- 2011 Q2
- 2011 Q3

In addition to the quarterly reports, the deliverables on several specific tasks or subtasks included a technical report. The quarterly report for 2008 Q3 was subsumed by the report

deliverable for Task 5.3. A full listing of these reports follows. Reports prepared as deliverables are denoted by '*'.

Juanes R., and Bryant, S. L., 2007. "Mechanisms Leading to Co-Existence of Gas and Hydrate in Ocean Sediments," *Quarterly Progress Report, October - December 2006*, University of Texas, DOE Award No.: DE-FC26-06NT43067. March 2007. (http://1.usa.gov/Hpzqtx)

Juanes R., and Bryant, S. L., 2007. "Mechanisms Leading to Co-Existence of Gas and Hydrate in Ocean Sediments," *Quarterly Progress Report, January – March 2007*, University of Texas, DOE Award No.: DE-FC26-06NT43067. April 2007. (http://1.usa.gov/HvPfxY)

* Juanes R., and Bryant, S. L., 2007. "Mechanisms Leading to Co-Existence of Gas and Hydrate in Ocean Sediments," *Creation of Sediment Models – Task 3 Technical Report*, University of Texas, DOE Award No.: DE-FC26-06NT43067. April 2007. (http://1.usa.gov/HvIJHF)

Juanes R., and Bryant, S. L., 2007. "Mechanisms Leading to Co-Existence of Gas and Hydrate in Ocean Sediments," *Quarterly Progress Report, April – June 2007*, University of Texas, DOE Award No.: DE-FC26-06NT43067. July 2007. (http://1.usa.gov/Hv4QeR)

Juanes R., and Bryant, S. L., 2007. "Mechanisms Leading to Co-Existence of Gas and Hydrate in Ocean Sediments," *Quarterly Progress Report, July –September 2007*, University of Texas, DOE Award No.: DE-FC26-06NT43067. October 2007. (http://1.usa.gov/HA4Hr4)

Juanes R., and Bryant, S. L., 2008. "Mechanisms Leading to Co-Existence of Gas and Hydrate in Ocean Sediments," *Quarterly Progress Report, October – December 2007*, University of Texas, DOE Award No.: DE-FC26-06NT43067. January 2008. (http://1.usa.gov/H42Qgu)

Juanes R., and Bryant, S. L., 2007. "Mechanisms Leading to Co-Existence of Gas and Hydrate in Ocean Sediments," *Quarterly Progress Report, January – March 2008*, University of Texas, DOE Award No.: DE-FC26-06NT43067. May 2008. (http://1.usa.gov/HA4OTu)

* Juanes R., and Bryant, S. L., 2008. "Mechanisms Leading to Co-Existence of Gas and Hydrate in Ocean Sediments," *Fracture Initiation and Propagation – Task 4 Technical Report*, University of Texas, DOE Award No.: DE-FC26-06NT43067. May 2008. (http://1.usa.gov/HvPFVe)

* Juanes R., and Bryant, S. L., 2008. "Mechanisms Leading to Co-Existence of Gas and Hydrate in Ocean Sediments," *Compute Critical Curvatures for Pore-level Events – Task 5.1 Technical Report*, University of Texas, DOE Award No.: DE-FC26-06NT43067. June 2008. (http://1.usa.gov/HvPKbx)

Juanes R., and Bryant, S. L., 2008. "Mechanisms Leading to Co-Existence of Gas and Hydrate in Ocean Sediments," *Quarterly Progress Report, April – June 2008*, University of Texas, DOE Award No.: DE-FC26-06NT43067. August 2008. (http://1.usa.gov/HBfvnj)

Juanes R., and Bryant, S. L., 2008. "Mechanisms Leading to Co-Existence of Gas and Hydrate in Ocean Sediments," *Quarterly Progress Report, July – September 2008*, University of Texas, DOE Award No.: DE-FC26-06NT43067. October 2008. (http://1.usa.gov/H2IoLy)

* Juanes R., and Bryant, S. L., 2008. "Mechanisms Leading to Co-Existence of Gas and Hydrate in Ocean Sediments," *Compute gas/water interface geometry during drainage and imbibtion in model sediments – Task 5.2 Technical Report*, University of Texas, DOE Award No.: DE-FC26-06NT43067. October 2008. (http://1.usa.gov/HpAyxn)
* Juanes R., and Bryant, S. L., 2008. "Mechanisms Leading to Co-Existence of Gas and Hydrate in Ocean Sediments," *Compute gas/water interface geometry within fracture – Task 5.3 Technical Report*, University of Texas, DOE Award No.: DE-FC26-06NT43067. October 2008. (http://1.usa.gov/H8jIMU)
Juanes R., and Bryant, S. L., 2009. "Mechanisms Leading to Co-Existence of Gas and Hydrate in Ocean Sediments," *Quarterly Progress Report, October – December 2008*, University of Texas, DOE Award No.: DE-FC26-06NT43067. February 2009. (http://1.usa.gov/H226rM)
* Juanes R., and Bryant, S. L., 2009. "Mechanisms Leading to Co-Existence of Gas and Hydrate in Ocean Sediments," *Couple gas/water interface dynamics with fracture propagation – Task 6 Technical Report*, University of Texas, DOE Award No.: DE-FC26-06NT43067. February 2009. (http://1.usa.gov/H225nM)
Juanes R., and Bryant, S. L., 2009. "Mechanisms Leading to Co-Existence of Gas and Hydrate in Ocean Sediments," *Quarterly Progress Report, January – March 2009*, University of Texas, DOE Award No.: DE-FC26-06NT43067. May 2009. (http://1.usa.gov/H2Ixyz)
Juanes R., and Bryant, S. L., 2009. "Mechanisms Leading to Co-Existence of Gas and Hydrate in Ocean Sediments," *Quarterly Progress Report, April – June 2009*, University of Texas, DOE Award No.: DE-FC26-06NT43067. July 2009. (http://1.usa.gov/H8jRjf)
* Juanes R., and Bryant, S. L., 2009. "Mechanisms Leading to Co-Existence of Gas and Hydrate in Ocean Sediments," *Coupled gas/water/sediment dynamics with rigid hydrate films – Task 7.1 Technical Report*, University of Texas, DOE Award No.: DE-FC26-06NT43067. October 2009. (http://1.usa.gov/HC4EIB)
Juanes R., and Bryant, S. L., 2010. "Mechanisms Leading to Co-Existence of Gas and Hydrate in Ocean Sediments," *Quarterly Progress Report, October - December 2009*, University of Texas, DOE Award No.: DE-FC26-06NT43067. January 2010. (http://1.usa.gov/H2IAdV)
Juanes R., and Bryant, S. L., 2010. "Mechanisms Leading to Co-Existence of Gas and Hydrate in Ocean Sediments," *Quarterly Progress Report, January - March 2010*, Massachusetts Institute of Technology, DOE Award No.: DE-FC26-06NT43067. March 2010. (http://1.usa.gov/H51Fyn)
Juanes R., and Bryant, S. L., 2010. "Mechanisms Leading to Co-Existence of Gas and Hydrate in Ocean Sediments," *Quarterly Progress Report, April - June 2010*, University of Texas, DOE Award No.: DE-FC26-06NT43067. August 2010. (http://1.usa.gov/H8k71M)
Juanes R., and Bryant, S. L., 2010. "Mechanisms Leading to Co-Existence of Gas and Hydrate in Ocean Sediments," *Quarterly Progress Report, July - September 2010*, University of Texas, DOE Award No.: DE-FC26-06NT43067. November 2010. (http://1.usa.gov/HrJSQd)
Juanes R., and Bryant, S. L., 2011. "Mechanisms Leading to Co-Existence of Gas and Hydrate in Ocean Sediments," *Quarterly Progress Report, October - December 2010*,

University of Texas, DOE Award No.: DE-FC26-06NT43067. February 2011. (http://1.usa.gov/HpBmlZ)

Juanes R., and Bryant, S. L., 2011. "Mechanisms Leading to Co-Existence of Gas and Hydrate in Ocean Sediments," *Quarterly Progress Report, January – March 2011*, University of Texas, DOE Award No.: DE-FC26-06NT43067. April 2011. (http://1.usa.gov/H5kYmM)

Juanes R., and Bryant, S. L., 2011. "Mechanisms Leading to Co-Existence of Gas and Hydrate in Ocean Sediments," *Quarterly Progress Report, April –June 2011*, University of Texas, DOE Award No.: DE-FC26-06NT43067. July 2011. (http://1.usa.gov/H38NoV)

Juanes R., and Bryant, S. L., 2011. "Mechanisms Leading to Co-Existence of Gas and Hydrate in Ocean Sediments," *Quarterly Progress Report, July –September 2011*, University of Texas, DOE Award No.: DE-FC26-06NT43067. October 2011. (http://1.usa.gov/H5l39S)